Graz University of Technology

Master Thesis

The Impact of Clock Offset on Multipath-assisted Indoor Localization

conducted at the
Signal Processing and Speech Communications Laboratory
Graz University of Technology, Austria

by
Rüdisser Christoph, 0830230

Supervisors:
Assoc.Prof. Dipl.-Ing. Dr. Klaus Witrisal
Dipl.-Ing. Paul Meissner
Dipl.-Ing. Erik Leitinger

Graz, September 15, 2014

Statutory Declaration

I declare that I have authored this thesis independently, that I have not used other than the declared sources/resources, and that I have explicitly marked all material which has been quoted either literally or by content from the used sources.

date	(signature)

Abstract

Multipath-assisted indoor localization is a promising technology for realizing highly accurate indoor localization systems based on ultra-wideband (UWB) radio signals. It exploits position-related information contained in deterministic signal reflections, which makes it inherently robust against malfunction in non-line-of-sight (NLOS) situations. Recent research results highlight the potential of this approach. However, perfect clock synchronization between transmitters and receivers was assumed up to now. This is not feasible in reality.

This thesis provides an in-depth analysis of multipath-assisted indoor localization in presence of clock asynchronism for different scenarios with either a single or multiple anchors. The fundamental limits of position estimation are studied by examining the Cramér-Rao lower bound (CRLB), and a quantitative assessment of the achievable performance is presented by evaluating the CRLB in an example scenario. The theoretical results are complemented by the examination of a maximum likelihood estimator (MLE), introducing several issues of practical relevance. The principal feasibility is successfully demonstrated using measurement data.

The theoretical results give evidence about the high achievable performance, which mainly depends on the signal bandwidth and the signal-to-interference-plus-noise ratios (SINRs) of signal reflections. Increasing the bandwidth is also an effective measure to remedy the performance degradation caused by the clock asynchronism as well as the influence of path overlap. Alternatively, the use of additional anchors also leads to a better room coverage. Multimodality of the likelihood function (LHF) reveals to be a major issue of the MLE. This can lead to an unacceptable number of outliers and therefore poor localization performance. An increase of the robustness can be achieved with the use of additional measures such as coarse clock synchronization, prior knowledge on the agent position, the use of multiple anchors or large signal bandwidth.

Kurzfassung

„Multipath-assisted indoor localization“ ist ein vielversprechender Lösungsansatz zur Realisierung von hochauflösender Innenraumlokalisierung basierend auf Ultra-Breitband-Funktechnologie. Dieser Ansatz verwendet Positionsinformation, welche in deterministischen Signalreflexionen enthalten ist. Aktuelle Forschungsergebnisse belegen das große Potential dieses Konzepts. Allerdings wurde bis jetzt immer perfekte Synchronisation zwischen der Basisstation und den Teilnehmern vorausgesetzt, was jedoch in der Praxis nicht realistisch ist.

Diese Masterarbeit untersucht den Einfluss der fehlenden Synchronisation auf Szenarien mit einer oder mehreren Basisstationen. Die theoretischen Grenzen des Lokalisierungsfehlers werden mit Hilfe der Cramér-Rao lower bound (CRLB) untersucht. Eine quantitative Beurteilung der Ergebnisse erfolgt durch die numerische Auswertung der CRLB für einen einfachen Innenraum. Die anschließende Analyse eines „Maximum-Likelihood“ (ML) Positionsschätzers liefert wichtige praxisrelevante Erkenntnisse, welche den theoretischen Teil der Arbeit vervollständigen. Abschließend wird die prinzipielle Funktionalität von multipath-assisted indoor localization bei fehlender Synchronisation mit realen Messdaten erfolgreich demonstriert.

Die theoretischen Ergebnisse heben die hohe Leistungsfähigkeit hervor, welche hauptsächlich von der verwendeten Signalbandbreite sowie vom Signal-zu-Interferenz-und-Rausch-Abstand der deterministischen Signalkomponenten abhängt. Eine Erhöhung der Bandbreite reduziert zudem den Einfluss der fehlenden Synchronisation und von zeitlicher Überlappung der Mehrwegekomponenten. Alternativ können auch mehrere Basisstationen verwendet werden, wodurch zusätzlich noch die Raumabdeckung erhöht wird. Die Multimodalität der Likelihood-Funktion stellt sich als das Hauptproblem des ML Schätzers heraus. Durch diese kann es zu Ausreißern kommen, wodurch die Leistungsfähigkeit stark beeinträchtigt wird. Die Robustheit kann jedoch mit geeigneten Mitteln erhöht werden, z.B. mit Hilfe von teilweiser Synchronisation, a-priori Wissen über die Position, Verwendung mehrerer Basisstationen oder hoher Signalbandbreite.

Acknowledgement

I want to express my gratitude to everyone who supported me throughout the course of this thesis. In particular I want to thank Assoc. Prof. Dipl.-Ing. Dr. Klaus Witrisal for giving me the opportunity to contribute to such an interesting project, and for the great supervision together with Dipl.-Ing. Paul Meissner and Dipl.-Ing. Erik Leitinger. They deserve special thanks for the helpful advices, motivation, patience, encouragement and support. Thanks to my parents, who helped me to enjoy the years of study in a carefree manner. And finally I would like to thank my girlfriend Alexandra for always supporting me.

Christoph Rüdisser

Contents

Tables and Figures

List of Tables

List of Figures

Notation and Symbols

Used Notation

a	a scalar number
a^*	conjugate complex of a
$\mathbf{a}$	a column vector, lowercase and boldface
$\|\|\mathbf{a}\|\|$	euclidean norm
$\mathbf{A},\ \mathbf{A}_{(i\times j)}$	a matrix (uppercase and boldface), a $(i \times j)$ matrix
$[\mathbf{A}]_{i,j}$	matrix element in row i and column j
$[\mathbf{A}]_{i\times j}$	$(i \times j)$ principal submatrix of $\mathbf{A}$
$\mathbf{a}^T,\ \mathbf{A}^T$	transposed vector / matrix
$\mathbf{a}^H,\ \mathbf{A}^H$	hermitian transposed vector / matrix
$\mathbf{I}$	identity matrix
$\mathrm{Tr}\{\}$	trace of a matrix
$\mathrm{E}\{\}$	expectation operator
$\mathcal{F}\{\}$	fourier transformation
$\mathrm{Re}\{\}, \mathrm{Im}\{\}$	real and imaginary parts of a complex number

List of frequently used Symbols

$\mathbf{p},\ \hat{\mathbf{p}}$	position of the mobile agent and its estimate
$s(t)$	transmit pulse
β	RMS bandwidth of the transmit pulse
$r(t),\ \mathbf{r}$	received signal
J	number of anchors
$K^{(j)}$	number of MPCs from anchor j
$\mathbf{p}_k^{(j)}$	position of the k-th VA of anchor j
$\alpha_k^{(j)}$	complex amplitude of the k-th MPC of anchor j
$\tau_k^{(j)}$	arrival time of the k-th MPC of anchor j
$\xi^{(j)}$	clock offset between the j-th transmitter and the receiver
$\boldsymbol{\theta},\ \hat{\boldsymbol{\theta}}$	channel parameter vector and its estimate
$\ln\ f(\mathbf{r};\boldsymbol{\theta})$	log-LHF of $\boldsymbol{\theta}$ given observation $\mathbf{r}$
$\mathbf{C}_{\hat{\boldsymbol{\theta}}},\ \mathbf{C}_{\hat{\mathbf{p}}}$	covariance matrix for $\hat{\boldsymbol{\theta}}$ and $\hat{\mathbf{p}}$
$\mathbf{J}_{\boldsymbol{\theta}},\ \mathbf{J}_{\mathbf{p}}$	FIM for $\boldsymbol{\theta}$ and EFIM for $\mathbf{p}$, respectively

Abbreviations

List of Abbreviations

2D	two-dimensional
ACF	autocorrelation function
AWGN	additive white gaussian noise
CDF	cummulative distribution function
CEB	clock error bound
CIR	channel impulse response
CRLB	Cramér-Rao lower bound
EFIM	equivalent Fisher information matrix
FIM	Fisher information matrix
GPS	Global Positioning System
IR-UWB	impulse-radio-based ultra-wideband technology
LHF	likelihood function
LOS	line-of-sight
LTI	linear time-invariant
MAP	maximum a posteriori
MINT	multipath-assisted indoor navigation and tracking
ML	maximum likelihood
MLE	maximum likelihood estimator
MPC	multipath component
MVUE	minimum variance unbiased estimator
NLOS	non-line-of-sight
NTP	network time protocol

PDF	probability density function
PDP	power delay profile
PEB	position error bound
PO	path overlap
ppm	parts per million
PSD	power spectral density
RBS	reference broadcast synchronization
RC	raised-cosine
RF	radio frequency
RMS	root mean square
RP	random process
RRC	root-raised-cosine
RTXO	room temperature crystal oscillators
RV	random vector
SINR	signal-to-interference-plus-noise ratio
SNR	signal-to-noise ratio
TDOA	time-difference-of-arrival
TOA	time-of-arrival
TOF	time-of-flight
TPSN	timing-sync protocol for sensor networks
UWB	ultra-wideband
VA	virtual anchor
WSN	wireless sensor network

1 Introduction

During recent years, a rising demand for highly accurate indoor localization systems has been observed. Terms like ubiquitous computing or context- and location-awareness shape a new generation of devices, enabling numerous new applications. Potential applications cover the commercial sector, public safety, and the military sector and could provide assistance in logistics, security, rescue operations etc. [1, 2].

While location awareness is already enabled in outdoor environments e.g. by the use of the Global Positioning System (GPS), highly accurate and especially robust indoor localization is still a major research topic. Different approaches for indoor localization exist, including e.g. optical systems and signal strength based systems [3, 4]. Localization systems based on range measurements [1] using radio signals are especially attractive, as they could be implemented in already existing communication devices. However, existing localization techniques cannot directly be applied to indoor environments, due to the harsh propagation environment. Multipath propagation, caused by specular reflections and scattering on walls and objects, as well as frequent NLOS situations represent the main difficulties for indoor localization [1]. Different approaches were proposed to deal with these issues, including e.g. the detection of NLOS situations [5].

While multipath propagation represents a major issue for most localization systems, it enables at the same time a completely different approach to the localization problem, which was named multipath-assisted indoor navigation and tracking (MINT) in [6]. This concept explicitly uses deterministic multipath components (MPCs), resulting from signal reflections on walls and other surfaces. Together with floor plan information of the indoor environment, these deterministic MPCs contain valuable position information, which can be used for localization. The resulting advantages are its inherent robustness to multipath propagation and a reduced cost for infrastructure, by theoretically allowing localization with only one fixed anchor. Performing multipath-assisted localization requires to extract individual MPCs from the received signal, which makes the use of UWB signals obligatory [7]. Current research results [8, 9] highlight the feasibility of this approach also in real-time implementations as well as the impressive performance.

An open issue of the current MINT analyses and implementations is that they rely on per-

fect clock synchronization between transmitter and receiver, thus enabling localization directly based on the arrival times of MPCs. In a realistic implementation, the desired sub-nanosecond clock accuracy is most likely not feasible. In [10] it is shown that perfect pairwise clock synchronization is not possible when having asymmetric path-delays. The performance of clock synchronization using protocols commonly used in wireless sensor network (WSN) are insufficient. E.g. the network time protocol (NTP), reference broadcast synchronization (RBS) or timing-sync protocol for sensor networks (TPSN) achieve clock synchronization in the range of milliseconds to microseconds [11]. Synchronization using an impulse-radio-based ultra-wideband technology (IR-UWB) was shown to achieve a performance in the order of 1 ns [12]. Still, when performing localization, such a synchronization error results in a rather large error.

As a consequence, we explicitly need to take the clock asynchronism into account, and focus on feasibility of multipath-assisted indoor localization in presence of clock asynchronism. Without having prior knowledge on the clock error, only the differences of the arrival times of the MPCs carry information which can be used for localization, therefore we refer to multipath-assisted localization in presence of a clock offset as multipath-assisted time-difference-of-arrival (TDOA) (In contrast, if perfect synchronization is assumed, we call it the time-of-arrival (TOA) setup). The receiver needs to perform the position and clock estimation jointly, solely based on the received signal and the knowledge of the floor plan.

The methodology for the present analysis is as follows: We will first examine the CRLB for the position estimation error, which yields the fundamental limit of position estimation. The CRLB for TDOA systems has already been the focus of several publications like [13–17] and similar. But these derivations are based directly on the TDOA metric, i.e. the differences of the arrival times. Therefore, the difficulty of extracting the TDOA metric from the received signal is ignored. We on the other hand formulate the CRLB of the position error solely based on one observation of the received signal. This approach is an extension of the work in [6], so that it considers the unknown clock offset. It is also similar to the TDOA analysis in [2], but with focus on multipath-assisted localization.

Since the analysis using the CRLB does not cover all issues which arise when implementing a multipath-assisted TDOA system, we also analyze how the clock offset affects a real estimator, by examining its impact on an MLE. Efficient methods for maximum likelihood (ML) position estimation based on the TDOA metric exist (e.g. [18] etc.), but are not directly applicable to the given problem, since the extraction of the metric as well as data association are not possible in a simple and reliable way. We therefore implement the MLE directly based on a sampled version of the received signal. This approach also has the advantage that the performance results of the MLE can be compared with the theoretical results of the CRLB.

1.1 Contribution of this Thesis

- Extension of the system model in [6] to consider the clock asynchronism between transmitter and receiver.

- The derivation and analysis of the CRLB for the position estimates and clock offset, based on the received signal waveform. Thereby scenarios with either a single or multiple synchronous / asynchronous anchors are considered. The results have also been published in [19].

- Numerical evaluation and analysis of the CRLB across a floor plan of an example scenario. Qualitative and quantitative comparison of the differences between TDOA and TOA; assessment of measures to circumvent the performance loss.
- Formulation of the MLE for the agent position, considering a setup with either a single or multiple synchronous / asynchronous anchors.
- Numerical evaluation of the MLE, investigation of potential problems, presentation of remedial measures.
- Verification of the CRLB by comparison with the MLE performance.
- Case study: Performing localization using the MLE with measurement data.

1.2 Outline

The remaining work is structured as follows:

Chapter 2 gives an overview about the system model. It introduces the concept of virtual anchors (VAs), which is used to model deterministic signal reflections. Extending this model by probabilistic assumptions about diffuse multipath leads then to a model for the received signal. This forms the basis for analyzing the impact of the unknown clock offset. We then define the position estimator and discuss some basic issues and challenges of the estimation problem. The model is extended for the use of multiple anchors. The chapter finishes with the definition of an example scenario, which is used in Chapter 3 and 4 to perform the numerical evaluation of the CRLB and the MLE.

Chapter 3 presents a detailed analysis of the impact of the unknown clock offset on the theoretical limits of position estimation. We start the analysis by discussing performance measures for estimators such as the covariance matrix of the position estimates, and then introduce the CRLB as a lower bound for it. After deriving the CRLB for different scenarios with single or multiple anchors, we simplify the result using the concepts of the equivalent Fisher information matrix (EFIM) and position error bound (PEB). The influence of design parameters is analyzed and the influence of the clock asynchronism is quantified by numerical evaluation for the example scenario. The results highlight the importance of design parameters such as the signal bandwidth, and the problem of path overlap (PO). They also allow to find appropriate countermeasures to reduce the impact of the clock offset.

Chapter 4 examines the impact of the unknown clock offset on an actual estimator implementation, namely an MLE. Therefore statistical properties of the sampled received waveform are derived, and the MLE is defined. Because of the high computational cost some simplifications of the LHF are discussed. Issues of practical relevance are examined by visual inspection of the LHF, and remedial measures are presented. The performance of the MLE is compared with the CRLB. The principal feasibility of multipath-assisted localization in presence of a clock offset is then demonstrated by evaluating the MLE based on measurement data.

Chapter 5 finally draws a conclusion and discusses further work.

2 System Model

2.1 Introduction

In this chapter we will introduce the system model, which provides the basis for analyzing the impact of the unknown clock offset in the following chapters. More precisely, we will focus on how to model the received signal, as this is essential for assessing estimator performance as well as for deriving an optimal estimator. In order to develop an accurate model, it is necessary to first understand multipath-assisted indoor localization. We will discuss the concept of VAs and how they help to model deterministic signal reflections. With the introduction of the clock offset and probabilistic assumptions about diffuse multipath we are finally able to give a model for the received signal.

What follows are some first considerations about similarities to other localization systems, possible challenges and limitations. Furthermore, we will extend the model for the use of multiple transmitting anchors, which can be beneficial to overcome some of the arising problems. We also define an example room scenario at the end of the chapter, which will later be used to perform numerical evaluation of the results of the following chapters.

It must be noted that the model described in this chapter does not differ very much from the model introduced in [6]. Actually the main difference is the introduction of the clock offset. However, here the whole model is treated more detailed and with additional interpretations for the sake of a better understanding and completeness.

2.2 Multipath-assisted Indoor Localization

Mutlipath-assisted indoor localization was first introduced in [20] under the title MINT. In contrast to conventional localization systems which make use of muliple transmitting anchors, the idea is to use only one transmitter, and extract geometric information from deterministic signal reflections. This requires some a priori information about the scenario, like e.g. the floor plan.

A scenario with minimal assumptions consists of only one anchor with a known position in an indoor environment, and a mobile agent with unknown position. The fixed anchor transmits a UWB signal which propagates on different paths to the receiver antenna. The mobile agent then examines the received signal, which contains valuable position information in the form of deterministic MPCs. These correspond to the line-of-sight (LOS) signal and signal reflections on walls and other surfaces. Together with the floor plan information, the receiver can then estimate its position using these deterministic MPCs[1].

The use of information contained in deterministic MPCs is an important advantage of this approach in contrast to conventional localization systems: For the latter, MPCs are often a source of error, and especially NLOS situations are difficult to handle. The explicit use of these MPCs makes the MINT approach robust against malfunction under these conditions.

Being able to extract the information contained in deterministic MPCs requires that we can resolve individual MPCs. The enabling technology is the use of UWB signals. These are defined as signals with an absolute bandwidth larger or equal than 500 MHz, or relative bandwidth greater than 20%. With the time-bandwidth product being constant, these signals have such low pulse durations, that it is possible to resolve individual MPCs, even if the are very close together. This is mandatory to achieve a high spatial resolution of the localization system.

The localization system can be extended by an arbitrary number of mobile agents at no additional cost for localization infrastructure – all these agents process the received signal from the same anchor. On the other hand this system can also be enhanced by using multiple transmitting anchors. Then every agent is able to estimate its position based on multiple observations, which leads to a better localization performance and enhanced room coverage.

2.3 The concept of Virtual Anchors

From the previous section it is clear, that deterministic signal reflections are essential for the presented approach. We now introduce VAs, which provide a simple yet elegant way to describe deterministic signal reflections. In addition they allow us to gain some more insight in the localization problem, as we will see in Section 2.6. In the following we will cover everything that is needed to understand the modelling of deterministic MPCs using VAs. For further reading see e.g. [21].

When considering an arbitrary scenario with a fixed anchor transmitting a waveform, the reflected signal components can be seen as signals transmitted by VAs. Therefore a VA, as indicated by its name, acts similar as an anchor. Each VA belongs to one specific physical anchor, and has a fixed position. It can be classified such as first-order VA, second-order and so forth, where the order corresponds to the number of signal reflections.

In order to understand the concept, we start by looking at how a set of VAs is constructed. For simplicity we restrict to the simple two-dimensional (2D) floor plan illustrated in Fig. 2.1(a), although this concept is easily extensible for complex 3D scenarios. The scenario consists of two wall segments in the 2D plane, with one fixed anchor used as transmitter. We obtain the first-order VAs by mirroring the anchor with respect to the wall segments, which results in two first-order VAs – one for each wall. This step is illustrated in Fig. 2.1(b). The second-order VAs

[1] Note that we can also interchange the tasks of the fixed anchor and the mobile agent, i.e. the mobile transmits the radio frequency (RF) waveform, and the fixed anchor performs the position estimation.

are then constructed from the first-order VAs, again by mirroring their position with respect to the wall segments as shown in Fig. 2.1(c). This results in two second-order VAs at the same coordinates, therefore we can merge these two and model them by a single second-order VA. With this procedure we can construct a set of VAs for an arbitrary floor plan, and for any desired VA order.

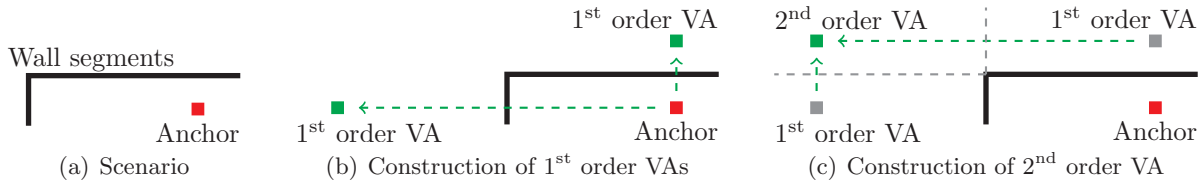

(a) Scenario (b) Construction of 1st order VAs (c) Construction of 2nd order VA

Figure 2.1: *Construction of VAs in the 2D plane. (a) shows the scenario, which consists of two wall segments and a fixed anchor. The first-order VAs are constructed by mirroring the anchor position with respect to the wall segments (b). For the second-order VAs we again have to mirror the first-order VAs (c).*

Now that we have a set of VAs, we can look at how these help to model deterministic signal reflections. We assume that the fixed anchor transmits a waveform, which propagates along different paths towards the receiver as it is illustrated in Fig. 2.2. The figure indicates the LOS component as well as first and second-order reflections. Note that the distances which the waves propagate on each path are equal to the distances between the VAs and the mobile agent. With the time-of-flight (TOF) being proportional to the traveled distance, we can specify the TOFs $\{\Delta t_k \in \mathbb{R} : k = 1 \dots K\}$ of the individual K received MPCs by

$$\Delta t_k = \frac{1}{c}\|\mathbf{p} - \mathbf{p}_k\|,$$

where $c \approx 3 \cdot 10^8$ m/s is the speed of light, and the vectors $\mathbf{p}$ and $\mathbf{p}_k$ denote the position of the mobile agent and of the k-th VA, respectively. From the illustration we can also see, that the angle of incident of MPCs can be modeled using VAs. The k-th MPC arrives in the direction $\mathbf{p} - \mathbf{p}_k$, with the angle written as ϕ_k.

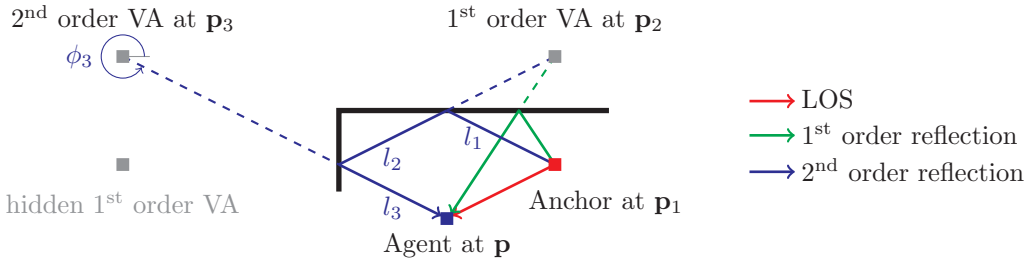

Figure 2.2: *Modeling signal reflections using VAs. Both, the distance which the wave needs to travel, as well as the angle of incident can be modeled using VAs (e.g. for the second-order reflection:* $l_1 + l_2 + l_3 = ||\mathbf{p} - \mathbf{p}_3||$, $\measuredangle(\mathbf{p} - \mathbf{p}_3) = \phi_3$*).*

However, we have to take into account that in general not all VAs are visible at the agent position. E.g. in Fig. 2.2 the mobile agent does not receive a MPC from the hidden first-order VA. The visibility of this specific VA is limited to an area above the agent and can be seen in

Fig. 2.3. Therefore $\{\mathbf{p}_k : k = 1 \dots K\}$ denotes the set of visible VAs for a specific agent position. Determining visibilities of VAs while performing localization is very expansive. But this can easily be avoided by precomputing the visibilities by e.g. using ray tracing, and then storing the results in a lookup table.

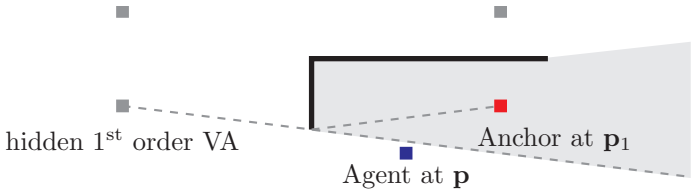

Figure 2.3: *Visibility of a specific VA. The VA at* $\mathbf{p}_3$ *is not visible at the agent position. Its visibility is indicated by the shaded area.*

Finally, we are able to summarize the requirements for a full scenario description: It can either be provided by a floor plan with the anchor position given, or by a set of VAs with the corresponding visibilities, where the later is for our purpose not only sufficient, but also beneficial.

2.4 Clock Asynchronism

If we assume perfect clock synchronization between transmitter and receiver, i.e. both use the same timebase t, we can easily determine the arrival times of the deterministic MPCs. Think of a signal transmitted at time $t = 0$, then the k-th deterministic MPC arrives at the receiver after $\Delta t_k = \frac{1}{c}\|\mathbf{p} - \mathbf{p}_k\|$. However, the requirements on suitable clock synchronization are very high. When e.g. using a UWB pulse for ranging, then even a small synchronization offset of 1 ns results in an error of $1\,\text{ns} \triangleq c \cdot 1\,\text{ns} = 30\,\text{cm}$. The desired sub-nanosecond synchronization accuracy would require immense effort and would most probably be unjustifiable. On the other hand just neglecting such a synchronization error would result in an unpredictable and large localization error when performing indoor localization.

Therefore, we have to be aware of the clock asynchronism, and take it into consideration during the whole analysis. This requires to study and model the clock offset. The model needs to be valid for a finite observation time $T_{obs} \in \mathbb{R}$, which obviously needs to be larger than the information carrying part of the channel impulse response (CIR), i.e. until the last considered deterministic MPC is received. With typical values for the root mean square (RMS) delay spread τ_{rms} in an indoor environment being somewhere between 10 ns and 300 ns, an observation time of $T_{obs} = 500\,\text{ns}$ still covers a TOF of at least 200 ns for the first deterministic MPC. This corresponds to a maximum distance of 60 meters between the anchor and the mobile agent, and therefore is clearly sufficient. When limiting the observation time to values in the order of several hundred nanoseconds, it is appropriate to apply a short time model as it is e.g. used for UWB ranging in [1],

$$C_{agent}(t_{true}) = (1 + \zeta)t_{true} + \xi, \qquad 0 \le t_{true} \le T_{obs}. \tag{2.1}$$

Here the local clock of the agent $C_{agent}(t_{true})$ is given as a function of the true time $t_{true} \in [0, T_{obs}]$, and considers an initial clock offset ξ, as well as a drift linearly depending on the true

time modeled by $\zeta = \frac{\mathrm{d}C_{agent}(t_{true})}{\mathrm{d}t_{true}}$. The clock offset causes a shift of the received signal, while it is compressed or spread by the drift.

Applying the model (2.1) on e.g. a crystal clock makes some more simplifications evident: In this case typical values the frequency stability are in the order of a few parts per million (ppm), e.g. when considering a room temperature crystal oscillators (RTXO) the temperature stability dominates the frequency error with 2.5ppm over a 0 to 50 degree range followed by aging with a rate of less than 0.3ppm for a 30-days period [22]. Assuming a crystal oscillator aged for ten years, this causes a clock error in the range of picoseconds during the observation time, which is clearly negligible when considering pulse durations in the order of nanoseconds. For the present problem we can therefore simplify the expression for the local clock to

$$C_{agent}(t_{true}) \approx t_{true} + \xi, \qquad 0 \leq t_{true} \leq T_{obs}. \tag{2.2}$$

In the following we will express the received signal in the timebase of the agent, which we denote as $t := C_{agent}(t_{true})$. With this definition it is sufficient to only consider the clock offset ξ. For the derivations in Chapter 3 and 4 it is important to mention, that we model ξ as an unknown but deterministic parameter, since we do not consider a probability density function (PDF) for it.

2.5 Modeling the Received Signal

With the findings of the previous chapters we are able to model the deterministic signal reflections. In order to achieve a realistic signal model, we also have to consider scattering and reflections on small surfaces. This is achieved by adapting the hybrid model of [6]. It accounts for deterministic components $\tilde{s}(t)$, diffuse multipath $n_c(t)$ and observation noise $w(t)$ as a function of the agent time t. Without loss of generality we assume that the anchor transmits the RF waveform at the true time $t_{true} = 0$. The baseband model $r(t) \in \mathbb{C}$ for the received signal in the timebase of the receiver is then given by

$$r(t) = \tilde{s}(t) + n_c(t) + w(t).$$

The deterministic part $\tilde{s}(t)$ consists of K pulses, one from each visible VA. The pulses are shifted to the corresponding arrival times τ_k and have amplitudes $\alpha_k \in \mathbb{C}$,

$$\tilde{s}(t) = \sum_{k=1}^{K} \alpha_k s(t - \tau_k).$$

The pulse-shapes of the MPCs are defined by the transmit pulse $s(t)$. We denote its pulse-duration by T_p, and its Fourier-transform as $\mathcal{F}\{s(t)\} = S(f)$. The amplitudes depend on the properties of the reflecting surfaces, and are not further specified. The arrival-times can easily be stated using the previously discussed concept of VAs and considering the clock offset. They are given by

$$\tau_k = \frac{1}{c}\|\mathbf{p} - \mathbf{p}_k\| + \xi. \tag{2.3}$$

The diffuse components are modeled by making assumptions about the random nature of the

channel. We model the frequency selectivity of the channel by specifying its power delay profile (PDP) $S_\nu(\tau)$. Assuming uncorrelated scattering its autocorrelation function (ACF) is given by

$$K_\nu(\tau, u) = \mathrm{E}\{\nu(\tau)\nu^*(u)\} = S_\nu(\tau)\delta(\tau - u).$$

where $\nu(\tau)$ is a Gaussian random process (RP) representing the CIR of the diffuse part of the channel. The contribution to the received signal is then given by convolving the transmit pulse with a realization of the diffuse CIR taking account for the clock offset, and is present as a colored Gaussian process,

$$n_c(t) = \int_{-\infty}^{\infty} s(\lambda)\nu(t - \xi - \lambda)d\lambda. \tag{2.4}$$

Note that we only consider frequency selectivity of the channel, and not time variability. Furthermore we assume a spatial stationarity of $\nu(t)$ in the vicinity of the inspected position.

Finally the observation noise $w(t)$ is modeled as additive white gaussian noise (AWGN), with double sided power spectral density (PSD) of $N_0/2$. This leads to the final signal model

$$r(t) = \sum_{k=1}^{K} \alpha_k s(t - \tau_k) + \int_{-\infty}^{\infty} s(\lambda)\nu(t - \xi - \lambda)d\lambda + w(t), \tag{2.5}$$

which is represented as a realization of a complex Gaussian RP. An example is illustrated in Fig. 2.4. It shows the composition of the received signal for the scenario described in Section 2.8. This model was verified in [23]. Measurements have shown, that the deterministic MPCs are

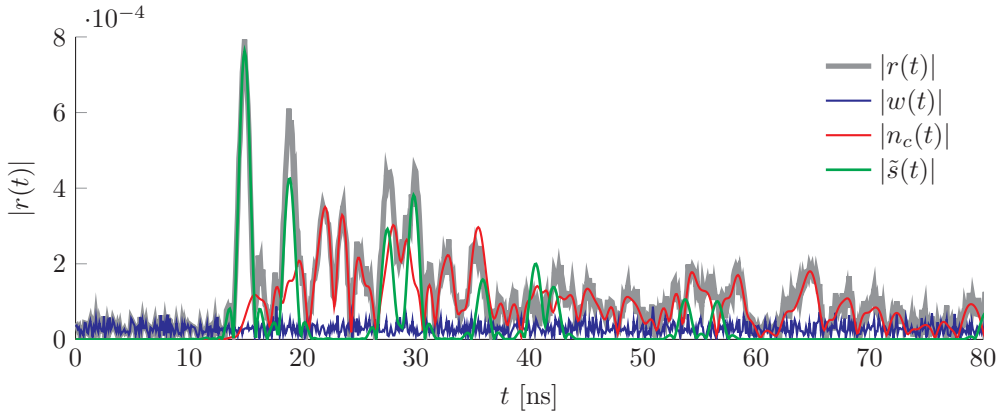

Figure 2.4: *Illustration of an example signal $r(t)$. Also shown are the deterministic components $\tilde{s}(t)$, a realization of the diffuse part $n_c(t)$ and the observation noise $w(t)$. This signal was generated from the signal model (2.5) with the floor plan and parameters defined in Section 2.8 for the agent position* $\mathbf{p} = [4, 5]^T$.

relevant features of the received signal and explain up to 90 % of the engergy capture.

2.6 The Estimation Problem at a First Glance

From a mathematical point of view, the continuous time waveform $r(t)$ results from a probabilistic mapping from the multidimensional parameter space to the continuous-time observation space. The problem is present as a signal with unknown nonrandom[2] parameters in colored noise. Goal is to find a suitable[3] estimation rule that yields estimates $\hat{\mathbf{p}}(r(t))$ of the true agent position $\mathbf{p}$ based on the observation $r(t)$, with $t \in [0, T_{obs}]$.

The considerations of the previous sections help to look at the problem from another point of view. Especially the concept of VAs is of major importance, since it indicates that all VAs act like fixed and synchronized anchors, but all using the same transmit pulse. This approach allows to figure out similarities to existing localization systems as well as potential challenges.

We start by making the following assumptions: We assume that we can extract the arrival times $\{\tau_k\}$ and map them to the corresponding VAs. Then, if the clock offset is known, the problem is exactly the one when performing TOA estimation with K anchors. In this case the MPCs define circles around each VA, with radii $\|\mathbf{p} - \mathbf{p}_k\| = \tau_k \cdot c$ as illustrated in Fig. 2.5(a). The position of the mobile is then found at the intersection off all these circles. Note that we need at least three VAs when 2D localization is performed. In 3D we have to deal with spheres instead of circles, and at least four anchors are needed[4].

In the present case with an unknown clock offset the absolute arrival times of isolated MPCs do not carry information which could be used for localization. On the other hand, the difference of arrival times gives some meaningful information, more precisely they define hyperbolas,

$$\tau_i - \tau_j = \frac{1}{c}\|\mathbf{p} - \mathbf{p}_i\| + \xi - \frac{1}{c}\|\mathbf{p} - \mathbf{p}_j\| - \xi = \frac{1}{c}\left(\|\mathbf{p} - \mathbf{p}_i\| - \|\mathbf{p} - \mathbf{p}_j\|\right).$$

This signal metric is referred to as TDOA, and position estimation using TDOA is often called hyperbolic localization. From now on we refer to multipath-assisted localization in presence of a clock offset as the TDOA case. In contrast to a conventional TDOA system, in the given scenario the assignment of the deterministic MPCs to the corresponding VAs is not given[5]. Since the contribution of each VA only differs in phase and amplitude, we cannot ensure proper assignment between MPCs and VAs. Even if we know the involved set of K VAs and MPCs, there are still $K!$ (factorial of K) possibilities for assigning MPCs to VAs. From the rather large set of resulting hyperbolas the true set has to be chosen.

In general even these assumptions are too optimistic. We will already face difficulties when estimating the correct set of arrival times $\{\tau_k\}$ of the deterministic MPCs, which result in a degradation of the localization performance. This is caused by multiple factors, such as the disturbance caused by diffuse multipath, hidden VAs, noise etc. An important limiting factor is PO. We refer to a PO situation if two MPCs arrive at almost equal times, more precisely if the arrival times are in the range of $|\tau_i - \tau_j| \leq T_p$. This causes that the pulses are merged, which can lead to destructive interference and make the estimation impossible. This problem is illustrated in Fig. 2.6.

The discussion above clearly shows the complexity of the given estimation problem. In order to overcome these difficulties, a suitable estimator has to be able to extract signal metrics,

[2] It is nonrandom, since we do not take any knowledge about the distribution of the parameters into account.
[3] We will discuss estimator performance measures in Section 3.2.
[4] Holds if we assume no further information about the floor plan and position of the agent.
[5] This is also the case if the clock offset is known, i.e. in the TOA case.

perform data association and deal with diffuse multipath, PO situations, blocked signal paths, room symmetries and so on. The estimator presented in Chapter 4 performs all these steps implicitly, by examining the entire received signal with statistical methods.

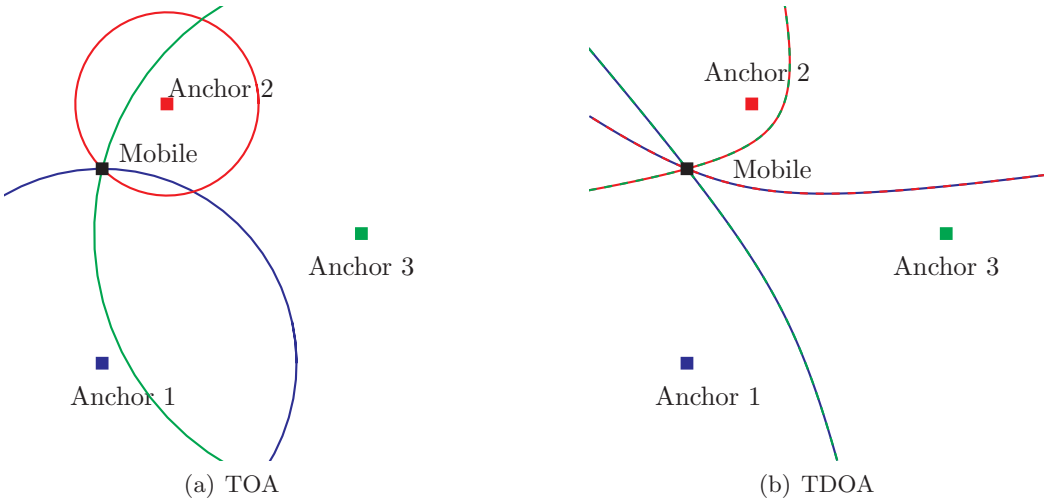

Figure 2.5: *Illustration of (a) TOA and (b) TDOA. The TOA metric defines circles, while the TDOA metric defines hyperbolas. The agent is located at the intersection point of all the circles/hyperbolas.*

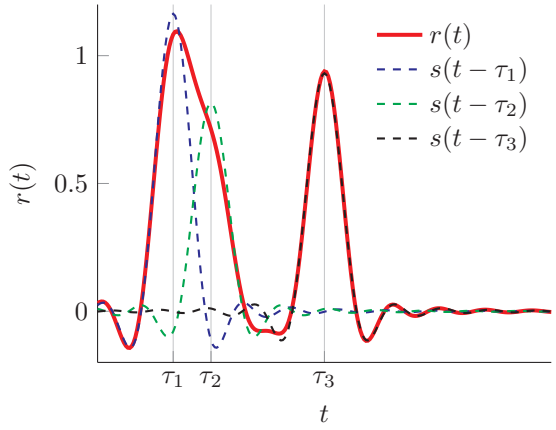

Figure 2.6: *Illustration of PO. Shown are three MPCs arriving at $\tau_1 \dots \tau_3$. Note that $\tau_2 - \tau_1 \approx T_p$, therefore PO occurs. On the other hand the MPC a τ_3 is far off the other pulses, and can easily be identified.*

2.7 Extension to Multiple Transmitting Anchors

So far we have only looked at the case, where a single anchor was used for localization. Now we will extend the localization system also to $J > 1$ anchors. In the numerical evaluation in Section 3.6 we will see that using multiple anchors has several advantages, especially in regions

where PO occurs, or in areas where only few VAs are visible.

When considering a system with multiple anchors, we distinguish between two different scenarios: (i) Anchors all have their own clock, without any synchronization at all. (ii) Anchors could be synchronized among each other. Of course also hybrid forms are possible, but we restrict the analysis to these two cases. Note that in either case we assume that there is no synchronization between the anchors and the mobile agent.

We can model the received signal independently of the above mentioned scenarios. We can always see it as a composition of the received signals $r^{(j)}(t)$ from each anchor, denoted as $\mathbf{r}^{(j)}$, where $1 \leq j \leq J$ refers to the corresponding anchor. Each $r^{(j)}(t)$ is modeled as in (2.5) with its own set of parameters. Furthermore, we will assume that each anchor uses an orthogonal signal waveform, such that we can distinguish the signals from the different anchors. In the simplest case these orthogonal signals can be achieved by e.g. shifting the transmit-signals from the different anchors in time. With this assumption, we are always able to extract the contributions $\mathbf{r}^{(j)}$ from the individual anchors without any loss of information. The stacked signal vector of all received signals is given by

$$\mathbf{r}_{\mathrm{M}} = [\mathbf{r}^{(1)^T}\ \mathbf{r}^{(2)^T}\ \ldots\ \mathbf{r}^{(J)^T}]^T.$$

Based on this extended signal model, the position of the mobile agent is then estimated by extracting information of this observation, i.e. $\hat{\mathbf{p}}(\mathbf{r}_{\mathrm{M}})$.

When looking at a problem which involves multiple anchors, parameters belonging to the j-th anchor are labeled by a superscript, e.g. $\alpha_k^{(j)}$. If a symbol is common to all anchors, e.g. the signal bandwidth $\beta^{(1)} = \beta^{(2)} = \cdots = \beta^{(J)}$, we will simply drop the anchor index and instead write β.

2.8 Scenario for Numerical Evaluation

In the following two chapters, we will perform numerical evaluation of the theoretical limits of position estimation and of an estimator implementation. In order to be able to find meaningful interpretations of the simulation results, we have to reduce the complexity of a real scenario. Therefore we use the simple scenario adapted from [6], which shall be introduced in the following.

The scenario is illustrated in Fig. 2.7. It consists of an L-shaped room with two fixed anchors at the positions $\mathbf{p}_1^{(1)} = [8, 7]^T$ and $\mathbf{p}_1^{(2)} = [1, 3]^T$. Constructing the corresponding VAs up to order two yields the VAs in Fig. 2.7(b). The blue and red-colored VAs belong to the first and second anchor, respectively.

In this scenario both anchors transmit root-raised-cosine (RRC) pulses with unit energy ($\varepsilon_s = \int_{-\infty}^{\infty} s^2(t)\mathrm{d}t = 1$) modulated onto a carrier with frequency $f_c = 7\,\mathrm{GHz}$. Transmitter and receiver antennas have identical polarization, an omnidirectional propagation pattern (i.e. power is radiated uniformly in all directions in the 2D plane), and antenna gain of $G_T = G_R = 1$. Wave propagation is modeled using the Friis transmission equation[6]. It specifies the amount of power at the receiver antenna under ideal conditions, i.e. for the LOS signal. With the

[6] Note that although we define how to model amplitudes of MPCs for numerical evaluation, we do not need this for deriving the CRLB or the MLE.

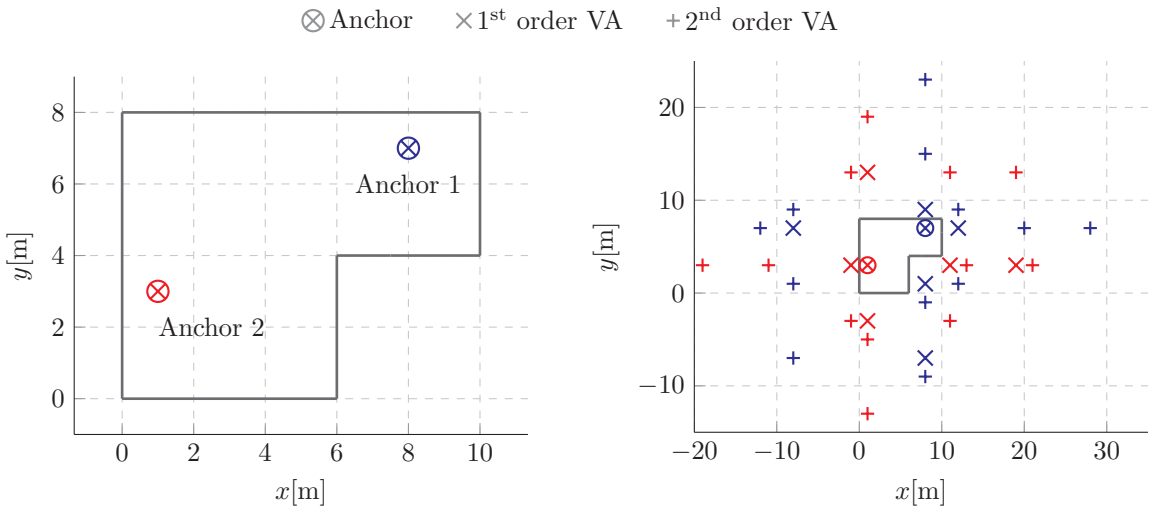

(a) Floorplan and two fixed anchors

(b) The set of 1st and 2nd order VAs

Figure 2.7: *Floorplan of an example room, its anchors and VAs. Fig. 2.7(a) shows the floor plan of the L-shaped room, with two anchors at* $\mathbf{p}_1^{(1)} = [8, 7]^T$ *and* $\mathbf{p}_1^{(2)} = [1, 3]^T$*. In (b) a overview of the VAs up to order two is illustrated. The colors indicate the affiliation of the VAs to the anchors.*

energy of the transmit pulse being $\varepsilon_s = \int_{-\infty}^{\infty} s^2(t)\mathrm{d}t := 1$ the energy of the k-th MPC is given as $\varepsilon_k = \int_{-\infty}^{\infty} |\alpha_k|^2 s^2(t)\mathrm{d}t = |\alpha_k|^2$. We can then express the energies as

$$|\alpha_k|^2 = G_k\, G_T\, G_R \left(\frac{\lambda}{4\pi||\mathbf{p} - \mathbf{p}_k||}\right)^2 = G_k \left(\frac{c}{4\pi f_c||\mathbf{p} - \mathbf{p}_k||}\right)^2,$$

where the term in the braces is the inverse of the free-space path loss, and λ is the wavelength $\lambda = \frac{c}{f_c}$. Since the Friis transmission equation does only considers LOS signals, G_k is introduced to account for the attenuation caused by signal reflections. It is chosen to be $-3\,\mathrm{dB}$ per reflection, i.e.

$$G_k = \begin{cases} 1 \triangleq 0\,\mathrm{dB} & \text{for the LOS signal,} \\ 10^{-3/10} \triangleq -3\,\mathrm{dB} & \text{for a } 1^{\text{st}} \text{ order reflection,} \\ 10^{-6/10} \triangleq -6\,\mathrm{dB} & \text{for a } 2^{\text{nd}} \text{ order reflection.} \end{cases}$$

Also the phase of the received signal is assumed to be distance depending,

$$\arg\{\alpha_k\} = 2\pi f_c \frac{1}{c}||\mathbf{p} - \mathbf{p}_k||.$$

The PDP of the diffuse multipath is modeled by a double exponential decay [24]

$$S_\nu(\tau) = \Omega_1 \frac{\gamma_1 + \gamma_{rise}}{\gamma_1(\gamma_1 + \gamma_{rise}(1 - \chi))}(1 - \chi \mathrm{e}^{-\tau/\gamma_{rise}})\mathrm{e}^{-\tau/\gamma_1}.$$

Its shape parameters (γ_1, γ_{rise}, χ) and energy Ω_1 were chosen as in [6], and result in a RMS delay spread of $\tau_{rms} \approx 20\,\mathrm{ns}$, which is appropriate for an indoor environment.

All the simulation parameters are summarized in Tab. 2.1, and are used unless otherwise mentioned. A realization of the received signal based on these parameters is shown in Fig. 2.4.

	Parameter	Value	Description
Deterministic MPCs		2	maximum order of reflections
		$-3\,\mathrm{dB}$	attenuation per reflection
Signal parameters	f_c	$7\,\mathrm{GHz}$	carrier frequency
	T_p	$1\,\mathrm{ns},\ (0.5\,\mathrm{ns}, 2\,\mathrm{ns})$	transmit-pulse duration
		RRC	pulse shape
	R	0.6	roll-off factor
	ε_s	1	energy of transmit-pulse
Diffuse MPC parameters	Ω_1	$1.16 \cdot 10^{-6}$	normalized power of diffuse MPC
	γ_1	$20\,\mathrm{ns}$	shape parameters
	γ_{rise}	$5\,\mathrm{ns}$	
	χ	0.98	
AWGN	N_0	10^{-8}	AWGN density

Table 2.1: *Parameters for the example scenario*

3 Cramér-Rao Lower Bound on the Position Estimation

3.1 Introduction

In this chapter we analyze the performance of estimators for the problem defined in Chapter 2. Since the influence of the channel parameters on the TOA case was already analyzed in [6], we will especially focus on the influence of the unknown clock offset. Therefore we will compare the performance of the TOA and TDOA system. Furthermore, we will see how we can prevent the performance degradation by varying design parameters (such as signal-bandwidth) or by enhancing the topology by additional transmitting anchors. The derivations are very close to the ones found in [6] and [2].

3.2 Estimator Performance Characterization

To assess the estimator performance we need to find a suitable performance measure. Since the estimator is a functional of a random process, the estimates are random variables. Therefore, we need to use statistical methods for the characterization. We will restrict our analysis to the class of *unbiased estimators*, which yield the true agent position *on average*,

$$\mathrm{E}\{\hat{\mathbf{p}}\} = \mathbf{p}. \tag{3.1}$$

We can further specify the performance by determining the variance of the position estimates $\mathrm{var}\{\hat{x}\}$ and $\mathrm{var}\{\hat{y}\}$. An estimator with low variance means that the position estimates are on average distributed closer to the true position, which makes it superior to one with larger variance. Even more meaningful is the consideration of the covariance matrix of the estimates,

$$\mathbf{C}_{\hat{\mathbf{p}}} = \mathrm{E}\Big\{ (\hat{\mathbf{p}} - \mathrm{E}\{\hat{\mathbf{p}}\}) (\hat{\mathbf{p}} - \mathrm{E}\{\hat{\mathbf{p}}\})^T \Big\} \ .$$

Especially, if we assume the position estimates to be jointly Gaussian, then in [25] it is shown that the covariance-matrix defines *concentration ellipses*, which are described in the following. In this case the PDF is given as

$$f_{\hat{\mathbf{p}}}(\hat{\mathbf{p}}) = \frac{1}{2\pi\sqrt{\det \mathbf{C}_{\hat{\mathbf{p}}}}} \exp\left(-\frac{1}{2}(\hat{\mathbf{p}} - \mathrm{E}\{\hat{\mathbf{p}}\})^T \mathbf{C}_{\hat{\mathbf{p}}}^{-1}(\hat{\mathbf{p}} - \mathrm{E}\{\hat{\mathbf{p}}\})\right),$$

and has its equal height if the exponent is held constant. With (3.1) we can specify the set $\mathcal{E}$ of points on this locus as

$$\mathcal{E} = \left\{\mathbf{p}_{eq} \in \mathbb{R}^2 : (\mathbf{p}_{eq} - \mathbf{p})^T \mathbf{C}_{\hat{\mathbf{p}}}^{-1}(\mathbf{p}_{eq} - \mathbf{p}) = C^2\right\},\ C \in \mathbb{R}. \tag{3.2}$$

Eq. (3.2) defines an ellipse centered around the true agent position $\mathbf{p}$ and provides a geometrical interpretation of the covariance matrix. The probability that the estimates are within this ellipse is given in [25] as

$$P = 1 - \exp\left(-\frac{C^2}{2}\right).$$

Therefore, the covariance matrix gives a measure of the concentration of the density. The orientation of the ellipse is defined by the eigenvectors of the covariance matrix $\mathbf{C}_{\hat{\mathbf{p}}}$, while the length of the major and minor axes are defined by the square-root of its eigenvalues and the choice of C. In the following we will always choose $C = 1$, and refer to the resulting ellipse as *concentration ellipse*.

However, we cannot claim that the position estimates are jointly Gaussian. But even in this case, the concentration ellipse roughly indicates the spread of the estimates around the agent position, and hereby provides some useful information.

The covariance matrix $\mathbf{C}_{\hat{\mathbf{p}}}$ yields a meaningful performance measure which is commonly used to evaluate estimators. But for our task it has a major disadvantage: it depends on the actual estimator implementation. To analyze our problem it would be necessary to find and implement different estimators and compare the results. This would not only be very time-consuming, but also not very meaningful, since this approach is not conclusive.

3.3 The Cramér-Rao Lower Bound

The CRLB helps to circumvent this problem. It provides us with a lower bound on the variance of *any* unbiased estimator, without the need of finding the actual estimator. As soon as we have determined this lower bound, it does not necessarily mean that we can find an estimator which attains the CRLB, but we can still use the result as a benchmark to compare any estimator against it. Furthermore, it helps to analyze the influence of the different parameters on the localization performance, and hereby helps to make good decisions when implementing such a system. Different bounds exist, but the CRLB is very popular for such a problem, since it is easy to derive for Gaussian signal models, and known to hold for high signal-to-noise ratios (SNRs).

We will now state the CRLB theorem as it can be found in many textbooks (e.g. in [25, 26]). We will also briefly discuss the involved terms in general. How to apply the CRLB to our problem will then be elaborated in the following sections.

Let $\hat{\boldsymbol{\theta}}$ be a vector containing the estimates of a parameter vector $\boldsymbol{\theta} \in \mathbb{R}^{D_{\boldsymbol{\theta}}}$,

$$\hat{\boldsymbol{\theta}} = [\hat{\theta}_1, \hat{\theta}_2, \ldots, \hat{\theta}_{D_{\boldsymbol{\theta}}}]^T \in \mathbb{R}^{D_{\boldsymbol{\theta}}} \ ,$$

with the covariance matrix

$$\mathbf{C}_{\hat{\boldsymbol{\theta}}} = \mathrm{E}\left\{ \left(\hat{\boldsymbol{\theta}} - \mathrm{E}\left\{ \hat{\boldsymbol{\theta}} \right\} \right) \left(\hat{\boldsymbol{\theta}} - \mathrm{E}\left\{ \hat{\boldsymbol{\theta}} \right\} \right)^T \right\} \ , \tag{3.3}$$

then the CRLB states that the covariance satisfies

$$\mathbf{C}_{\hat{\boldsymbol{\theta}}} - \mathbf{J}_{\boldsymbol{\theta}}^{-1}(\boldsymbol{\theta}) \succeq \mathbf{0} \ , \tag{3.4}$$

where $\mathbf{J}_{\boldsymbol{\theta}}(\boldsymbol{\theta})$ is the Fisher information matrix (FIM)[7] and the $\succeq$ sign indicates a positive-semidefinite matrix. The diagonal elements of a positive-semidefinite matrix are always positive, therefore we can express the lower bound on the variance of the parameters as the diagonal elements of the inverted FIM, given by

$$\mathrm{var}\left\{ \hat{\theta}_i \right\} = [\mathbf{C}_{\hat{\boldsymbol{\theta}}}]_{i,i} \geq [\mathbf{J}_{\boldsymbol{\theta}}^{-1}(\boldsymbol{\theta})]_{i,i} \ .$$

The FIM $\mathbf{J}_{\boldsymbol{\theta}}(\boldsymbol{\theta})$ is a measure of how much information for the estimation of the parameter vector $\boldsymbol{\theta}$ is contained in the observation $\mathbf{r}$. Assuming that the regularity condition $\mathrm{E}\left\{ \frac{\partial \ln \ f(\mathbf{r};\boldsymbol{\theta})}{\partial \boldsymbol{\theta}} \right\} = \mathbf{0}$ is fulfilled, its elements are given by

$$[\mathbf{J}_{\boldsymbol{\theta}}(\boldsymbol{\theta})]_{i,j} = -\mathrm{E}\left\{ \frac{\partial^2 \ln \ f(\mathbf{r};\boldsymbol{\theta})}{\partial \theta_i \partial \theta_j} \right\} = \mathrm{E}\left\{ \frac{\partial \ln \ f(\mathbf{r};\boldsymbol{\theta})}{\partial \theta_i} \frac{\partial \ln \ f(\mathbf{r};\boldsymbol{\theta})}{\partial \theta_j} \right\}, \tag{3.5}$$

where $f(\mathbf{r};\boldsymbol{\theta})$ is the probability density for the observation $\mathbf{r}$ given the parameter vector $\boldsymbol{\theta}$ [8]. But in this case we look at it as a function of $\boldsymbol{\theta}$, where the observation $\mathbf{r}$ is given. Therefore it is called the LHF of $\boldsymbol{\theta}$. This function plays an important role, and its derivation is a major task when determining the CRLB.

The CRLB-theorem indicates the next steps: in order to be able to compute the FIM, we need to know the structure of the LHF. As soon as we have the FIM, the computation of the CRLB is accomplished by a matrix inversion.

3.4 Localization with a Single Transmitting Anchor

We have now discussed the main ideas of the CRLB, and we will now look at the problem of estimating the position of an agent for the case where only one transmitting anchor is given. Later on we will also look at the problem when using multiple anchors.

[7] The used notation emphasizes that $\mathbf{J}_{\boldsymbol{\theta}}(\boldsymbol{\theta})$ is the FIM for the parameter vector $\boldsymbol{\theta}$ parameterized by $\boldsymbol{\theta}$. For simplicity we will sometimes omit the argument and instead write $\mathbf{J}_{\boldsymbol{\theta}}$

[8] We will here use the notation as in [26] to emphasize that $\boldsymbol{\theta}$ is an unknown but deterministic parameter, and no random vector.

3.4.1 The Approach

The first step is to define the parameter vector $\boldsymbol{\theta}$. It has to contain all parameters, on which the received signal depends. The agent position $\mathbf{p}$ is the primary parameter of interest, so we have to include this parameter. Furthermore, we have to add all other parameters, on which the received signal depends, even if we are not interested in the CRLB of those – these parameters are nuisance parameters. Including the clock offset ξ allows together with $\mathbf{p}$ to compute all arrival-times $\{\tau_k : 1 \leq k \leq K\}$. At last we also have to add the path-amplitudes to the parameter vector. Of course the received signal does also depend on the parameters describing the diffuse multipath, but these can be excluded, since we assume stationarity in the close vicinity of the position, where we examine the CRLB. The AWGN is assumed to be stationary in general. The resulting vector is then written as

$$\boldsymbol{\theta} = [\mathbf{p}^T \; \xi \; \boldsymbol{\alpha}_R^T \; \boldsymbol{\alpha}_I^T]^T \in \mathbb{R}^{D_{\boldsymbol{\theta}}}, \; D_{\boldsymbol{\theta}} = 2K + 3 \; . \tag{3.6}$$

The order of the elements in $\boldsymbol{\theta}$ is arbitrary, but if we formulate it as in (3.6) we will have an advantage for the further evaluation. More precisely it makes it easier to compute the EFIM as we will see in Section 3.4.4. Now that we have defined the parameter vector, we could express the LHF for $\boldsymbol{\theta}$, and then compute the FIM.

Alternatively we can use the same approach as in [2, 6]. There the FIM was computed in two steps: At first the FIM $\mathbf{J}_{\boldsymbol{\psi}}(\boldsymbol{\psi})$ for the signal parameter vector

$$\boldsymbol{\psi} = [\boldsymbol{\tau}^T \; \boldsymbol{\alpha}_R^T \; \boldsymbol{\alpha}_I^T]^T \in \mathbb{R}^{D_{\boldsymbol{\psi}}}, \; D_{\boldsymbol{\psi}} = 3K \tag{3.7}$$

was computed and then a parameter transformation was used to compute the final FIM $\mathbf{J}_{\boldsymbol{\theta}}(\boldsymbol{\theta})$. Note that $\boldsymbol{\psi}$ is expressed purely in terms of the multipath parameters (arrival-times and amplitudes of the MPCs), whereas $\boldsymbol{\theta}$ introduces the agent position and clock offset.

Expressing the LHF and the FIM for $\boldsymbol{\psi}$ has advantages: it is more intuitive, because the arrival times are closer related to the actual observation $\mathbf{r}$. They are the primarily accessible parameters when looking at the received waveform. But even more important for our problem is, that this provides a separation of the problem: when determining $\mathbf{J}_{\boldsymbol{\psi}}(\boldsymbol{\psi})$ we do not care about the estimation of the agent position but only on the estimation of the MPCs. The underlying geometrical relation is not of interest, therefore this problem is identical for TOA and TDOA. This allows us to reuse the FIM $\mathbf{J}_{\boldsymbol{\psi}}(\boldsymbol{\psi})$ from [6], and reduces the problem of computing the CRLB of the agent position to finding a suitable parameter transformation.

3.4.2 The Likelihood Function

In Section 2.5 we modeled the received signal as a complex-valued colored Gaussian process. When deriving the LHF the main difficulty arises because of the time-continuous and colored nature of the signal, since in general no analytical solution exists for the PDF or LHF for such a signal. In order to derive a LHF, some sort of whitening is required, i.e. we need to decorrelate the RP. This decorrelation can be achieved using the Karhunen-Loève transformation [25], which is basically an orthogonal series representation when using a special set of basis functions. This approach is used in [6] for deriving the LHF for the multipath parameters $\boldsymbol{\psi}$. However, because of the importance of the LHF we will reflect the main idea here.

Assuming that we have a set of orthogonal basis functions $\{\varphi_i(t) : \mathbb{R} \to \mathbb{R}, \, i = 0 \ldots N-1\}$,

i.e. a set of functions which fulfill

$$\int_0^{T_{obs}} \varphi_i(t)\varphi_j(t)\mathrm{d}t = 0 \quad \text{for } i \neq j,\ i,j = 0 \dots N-1, \tag{3.8}$$

with N approaching infinity, we can represent any received signal in this basis using

$$r(t) = \lim_{N\to\infty} \sum_{i=0}^{N-1} c_i \varphi_i(t), \qquad 0 \leq t \leq T_{obs}.$$

The coefficient c_i for a particular basis function is then given by the projection of the received signal onto the corresponding basis function,

$$c_i = \int_0^{T_{obs}} r(t)\varphi_i(t)\mathrm{d}t\ .$$

With a clever choice of the orthogonal basis, these coefficients are statistically independent Gaussian random variables, for which we can easily give the joint PDF. This is exactly the case, if we choose the basis functions to be eigenfunctions of the covariance $K_c(t,u)$ of the colored noise process,

$$\lambda_i \varphi_i(t) = \int_0^{T_{obs}} K_c(t,u)\varphi_i(u)\mathrm{d}u, \qquad 0 \leq t \leq T_{obs}. \tag{3.9}$$

Performing the transformation using a basis which fulfills both requirements, i.e. (3.8) and (3.9), is referred to as the Karhunen-Loève transformation [25].

For the given problem it turns out, that a finite set of N eigenfunctions is given by pulses shifted in time by the pulse duration T_p,

$$\varphi_i(t) = s(t - iT_p), \qquad i = 0 \dots N-1. \tag{3.10}$$

Furthermore, assuming perfect autocorrelation properties and unit energy of the transmit pulse, these yield an orthonormal basis. Performing the steps indicated above, i.e. formulating the joint PDF in terms of the coefficients, leads after some simplifications to the LHF [6]

$$\begin{aligned} f(\mathbf{r};\boldsymbol{\psi}) \propto \exp\Bigg\{ & \frac{2}{N_0}\int_0^{T_0} \mathrm{Re}\Bigg\{ r(t) - \sum_{k=1}^{K} w_k^2 \alpha_k^* s(t-\tau_k) \Bigg\} \mathrm{d}t \\ & -\frac{1}{N_0}\int_0^{T_0} \sum_{k'=1}^{K} \alpha_{k'} s(t-\tau_{k'}) \sum_{k=1}^{K} w_k^2 \alpha_k^* s(t-\tau_k)\mathrm{d}t \Bigg\}. \end{aligned} \tag{3.11}$$

Note that the difference between (3.11) and a standard LHF is only given by the weights w_k which account for the whitening operation. These weights are given by [6]

$$w_k^2 = \frac{N_0}{N_0 + T_p S_\nu(\tau_k - \xi)}. \tag{3.12}$$

However it is important to mention, that the above assumptions clearly restrict the validity of the LHF (3.11). First of all, as we have already stated, we assume the pulses shifted by T_p to be orthogonal. For the RRC pulses specified in Section 2.8 this requirement is not fulfilled, therefore

the result (3.11) is only an approximation. Even more important is, that the orthonormal basis $\{\varphi_i(t)\}$ is in general not a complete basis. Clearly, if an MPC has an arrival time different from a multiple of T_p, it can not be fully represented using this basis. However, for our purposes (3.11) still yields a good approximation when neglecting PO as it is done in Section 3.4.5. For completeness further investigations on the validity of the LHF are in progress.

3.4.3 The Fisher Information Matrix

The FIM $\mathbf{J}_{\boldsymbol{\psi}}(\boldsymbol{\psi})$ can now be computed according to (3.5) (substituting $\boldsymbol{\theta}$ by $\boldsymbol{\psi}$ and θ_i by ψ_i), and it is given in [6] as

$$\mathbf{J}_{\boldsymbol{\psi}} = \begin{bmatrix} \boldsymbol{\Lambda}_A & \boldsymbol{\Lambda}_B \\ \boldsymbol{\Lambda}_B^T & \boldsymbol{\Lambda}_C \end{bmatrix}, \quad \boldsymbol{\Lambda}_B = [\boldsymbol{\Lambda}_B^R, \boldsymbol{\Lambda}_B^I], \quad \boldsymbol{\Lambda}_C = \begin{bmatrix} \boldsymbol{\Lambda}_C' & \mathbf{0} \\ \mathbf{0} & \boldsymbol{\Lambda}_C' \end{bmatrix}. \tag{3.13}$$

The elements of the FIM can be computed using [6]

$$[\boldsymbol{\Lambda}_A]_{k,k'} = \frac{2}{N_0} \mathrm{Re}\{\alpha_k \alpha_{k'}^*\}\, w_k^2 \frac{\partial^2 R_s(\tau_k - \tau_{k'})}{\partial \tau_k \partial \tau_{k'}}, \tag{3.14}$$

$$[\boldsymbol{\Lambda}_B^R]_{k,k'} = \frac{2}{N_0} \alpha_k^R w_k^2 \frac{\partial R_s(\tau_k - \tau_{k'})}{\partial \tau_k}, \tag{3.15}$$

$$[\boldsymbol{\Lambda}_B^I]_{k,k'} = \frac{2}{N_0} \alpha_k^I w_k^2 \frac{\partial R_s(\tau_k - \tau_{k'})}{\partial \tau_k}, \tag{3.16}$$

$$[\boldsymbol{\Lambda}_C']_{k,k'} = \frac{2}{N_0} w_k^2 R_s(\tau_k - \tau_{k'}), \tag{3.17}$$

where $R_s(\tau)$ is the ACF of the transmit pulse $s(t)$.

In order to arrive at the final FIM $\mathbf{J}_{\boldsymbol{\theta}}(\boldsymbol{\theta})$ we have to perform the parameter transformation. We can write the partial derivatives in (3.5) using the chain rule,

$$\frac{\partial \ln\, f(\mathbf{r};\boldsymbol{\theta})}{\partial \theta_i} = \sum_{j=1}^{D_{\boldsymbol{\psi}}} \frac{\partial \ln\, f(\mathbf{r};\boldsymbol{\psi})}{\partial \psi_j} \frac{\partial \psi_j}{\partial \theta_i}. \tag{3.18}$$

With (3.18) in (3.5) we can already express the elements of $\mathbf{J}_{\boldsymbol{\theta}}(\boldsymbol{\theta})$ in terms of the elements of $\mathbf{J}_{\boldsymbol{\psi}}(\boldsymbol{\psi})$. But we can even go one step further by expressing the FIM in matrix notation,

$$\mathbf{J}_{\boldsymbol{\theta}}(\boldsymbol{\theta}) = \mathrm{E}\left\{ \left[\frac{\partial \ln\, f(\mathbf{r};\boldsymbol{\theta})}{\partial \boldsymbol{\theta}}\right] \left[\frac{\partial \ln\, f(\mathbf{r};\boldsymbol{\theta})}{\partial \boldsymbol{\theta}}\right]^T \right\}.$$

The term $\frac{\partial \ln\, f(\mathbf{r};\boldsymbol{\theta})}{\partial \boldsymbol{\theta}}$ is the gradient of the log-LHF, which is a column vector containing all the partial derivatives of the log-LHF with respect to the elements of $\boldsymbol{\theta}$. Equally as in (3.18) we can express the gradient using the chain rule,

$$\frac{\partial \ln\, f(\mathbf{r};\boldsymbol{\theta})}{\partial \boldsymbol{\theta}} = \left(\frac{\partial \boldsymbol{\psi}}{\partial \boldsymbol{\theta}}\right)^T \frac{\partial \ln\, f(\mathbf{r};\boldsymbol{\psi})}{\partial \boldsymbol{\psi}}.$$

Here $\frac{\partial \boldsymbol{\psi}}{\partial \boldsymbol{\theta}}$ is the Jacobian matrix, which contains all the partial derivatives of the elements of $\boldsymbol{\psi}$

with respect to the elements of $\boldsymbol{\theta}$,

$$\frac{\partial \boldsymbol{\psi}}{\partial \boldsymbol{\theta}} = \begin{bmatrix} \frac{\partial \psi_1}{\partial \theta_1} & \frac{\partial \psi_1}{\partial \theta_2} & \cdots & \frac{\partial \psi_1}{\partial \theta_N} \\ \frac{\partial \psi_2}{\partial \theta_1} & \frac{\partial \psi_2}{\partial \theta_2} & \cdots & \frac{\partial \psi_2}{\partial \theta_N} \\ \vdots & \vdots & \ddots & \vdots \\ \frac{\partial \psi_L}{\partial \theta_1} & \frac{\partial \psi_L}{\partial \theta_2} & \cdots & \frac{\partial \psi_L}{\partial \theta_N} \end{bmatrix}.$$

Finally we are able to express $\mathbf{J}_{\boldsymbol{\theta}}(\boldsymbol{\theta})$ using the given $\mathbf{J}_{\boldsymbol{\psi}}(\boldsymbol{\psi})$,

$$\begin{aligned} \mathbf{J}_{\boldsymbol{\theta}}(\boldsymbol{\theta}) &= \left[\frac{\partial \boldsymbol{\psi}}{\partial \boldsymbol{\theta}}\right]^T \mathrm{E}\left\{ \left[\frac{\partial \ln\ f(\mathbf{r};\boldsymbol{\psi})}{\partial \boldsymbol{\psi}}\right] \left[\frac{\partial \ln\ f(\mathbf{r};\boldsymbol{\psi})}{\partial \boldsymbol{\psi}}\right]^T \right\} \left[\frac{\partial \boldsymbol{\psi}}{\partial \boldsymbol{\theta}}\right] \\ &= \left[\frac{\partial \boldsymbol{\psi}}{\partial \boldsymbol{\theta}}\right]^T \mathbf{J}_{\boldsymbol{\psi}}(\boldsymbol{\psi}) \left[\frac{\partial \boldsymbol{\psi}}{\partial \boldsymbol{\theta}}\right] \\ &= \mathbf{T}^T \mathbf{J}_{\boldsymbol{\psi}} \mathbf{T}. \end{aligned} \tag{3.19}$$

So the transformation matrix $\mathbf{T} \in \mathbb{R}^{D_{\boldsymbol{\psi}} \times D_{\boldsymbol{\theta}}}$ is the key element which connects the FIM for the MPCs with the desired FIM for $\boldsymbol{\theta}$. We will now take a closer look at this transformation matrix. We have already partitioned the parameter vectors $\boldsymbol{\psi}$ and $\boldsymbol{\theta}$ to subvectors when we defined them (3.7, 3.6), so it also makes sense to express the Jacobian matrix in terms of these subvectors and partition it as following,

$$\mathbf{T} = \frac{\partial \boldsymbol{\psi}}{\partial \boldsymbol{\theta}} = \begin{bmatrix} \frac{\partial \boldsymbol{\tau}}{\partial \mathbf{p}} & \frac{\partial \boldsymbol{\tau}}{\partial \xi} & \frac{\partial \boldsymbol{\tau}}{\partial \boldsymbol{\alpha}_R} & \frac{\partial \boldsymbol{\tau}}{\partial \boldsymbol{\alpha}_I} \\ \frac{\partial \boldsymbol{\alpha}_R}{\partial \mathbf{p}} & \frac{\partial \boldsymbol{\alpha}_R}{\partial \xi} & \frac{\partial \boldsymbol{\alpha}_R}{\partial \boldsymbol{\alpha}_R} & \frac{\partial \boldsymbol{\alpha}_R}{\partial \boldsymbol{\alpha}_I} \\ \frac{\partial \boldsymbol{\alpha}_I}{\partial \mathbf{p}} & \frac{\partial \boldsymbol{\alpha}_I}{\partial \xi} & \frac{\partial \boldsymbol{\alpha}_I}{\partial \boldsymbol{\alpha}_R} & \frac{\partial \boldsymbol{\alpha}_I}{\partial \boldsymbol{\alpha}_I} \end{bmatrix}.$$

With this representation it is trivial to determine all these submatrices:

The first submatrix $\frac{\partial \boldsymbol{\tau}}{\partial \mathbf{p}}$ assembles how the arrival-times relate to the agent position. Because of the importance of this submatrix we will define the new symbol $\mathbf{H} \in \mathbb{R}^{K \times 2}$. Using (2.3) leads to

$$\mathbf{H} = \frac{\partial \boldsymbol{\tau}}{\partial \mathbf{p}} = \begin{bmatrix} \frac{\partial \tau_1}{\partial x} & \frac{\partial \tau_1}{\partial y} \\ \frac{\partial \tau_2}{\partial x} & \frac{\partial \tau_2}{\partial y} \\ \vdots & \vdots \\ \frac{\partial \tau_K}{\partial x} & \frac{\partial \tau_K}{\partial y} \end{bmatrix} = \begin{bmatrix} \frac{1}{c}\cos(\phi_1) & \frac{1}{c}\sin(\phi_1) \\ \frac{1}{c}\cos(\phi_2) & \frac{1}{c}\sin(\phi_2) \\ \vdots & \vdots \\ \frac{1}{c}\cos(\phi_K) & \frac{1}{c}\sin(\phi_K) \end{bmatrix}. \tag{3.20}$$

Here the variables ϕ_i refer to the angle of incident of the i-th MPC. Note that when comparing (3.20) with the result in [6], we can see that $\mathbf{H}$ is equal for both cases, no matter whether we consider the TOA- or the TDOA-case.

The vector $\frac{\partial \boldsymbol{\tau}}{\partial \xi}$ is determined by the derivative of (2.3) with respect to ξ and yields

$$\mathbf{k} = \frac{\partial \boldsymbol{\tau}}{\partial \xi} = [1, 1, \ldots, 1]^T \in \mathbb{R}^{K \times 1}.$$

All remaining submatrices contain either the partial derivatives of the path amplitudes with

respect to the other parameters or vice versa. Since the path amplitudes do not depend on any other parameters except of themselves, all terms with the exception of $\frac{\partial \alpha_k}{\partial \alpha_k} = 1$, $k = 1, \ldots, K$ are zero matrices.

The fully assembled transformation matrix $\mathbf{T}$ is thus given by

$$\mathbf{T} = \begin{bmatrix} \frac{\partial \boldsymbol{\tau}}{\partial \mathbf{p}} & \frac{\partial \boldsymbol{\tau}}{\partial \xi} & \mathbf{0} & \mathbf{0} \\ \mathbf{0} & \mathbf{0} & \mathbf{I}_{K\times K} & \mathbf{0} \\ \mathbf{0} & \mathbf{0} & \mathbf{0} & \mathbf{I}_{K\times K} \end{bmatrix} = \begin{bmatrix} \mathbf{H}_{K\times 2} & \mathbf{k}_{K\times 1} & \mathbf{0}_{K\times 2K} \\ \mathbf{0}_{2K\times 2} & \mathbf{0}_{2K\times 1} & \mathbf{I}_{2K\times 2K} \end{bmatrix},$$

where $\mathbf{I}$ is the identity matrix. The only thing that is left in order to formulate the final FIM is to repartition the transformation matrix in a way, so that blockwise matrix multiplication can be performed. This is achieved as follows,

$$\mathbf{T} = \left[\begin{array}{c|cc} \mathbf{H} & \mathbf{k} & \mathbf{0} \\ \hline \mathbf{0} & \mathbf{0} & \mathbf{I} \end{array}\right] = \begin{bmatrix} \mathbf{H} & \mathbf{K} \\ \mathbf{0} & \mathbf{L} \end{bmatrix},$$

with

$$\mathbf{K} = [\mathbf{k}, \mathbf{0}] = \begin{bmatrix} 1 & 0 & \cdots & 0 \\ \vdots & \vdots & & \vdots \\ 1 & 0 & \cdots & 0 \end{bmatrix}, \quad \mathbf{K} \in \mathbb{R}^{K\times 2K+1}, \tag{3.21}$$

and

$$\mathbf{L} = [\mathbf{0}, \mathbf{I}] = \begin{bmatrix} 0 & 1 & & \\ \vdots & & \ddots & \\ 0 & & & 1 \end{bmatrix}, \quad \mathbf{L} \in \mathbb{R}^{2K\times 2K+1}. \tag{3.22}$$

Applying the parameter transformation (3.19) is now straight forward and results in the final FIM $\mathbf{J}_{\boldsymbol{\theta}}(\boldsymbol{\theta}) \in \mathbb{R}^{D_{\boldsymbol{\theta}}\times D_{\boldsymbol{\theta}}}$

$$\mathbf{J}_{\boldsymbol{\theta}}(\boldsymbol{\theta}) = \begin{bmatrix} \mathbf{H}^T\boldsymbol{\Lambda}_A\mathbf{H} & \mathbf{H}^T\boldsymbol{\Lambda}_A\mathbf{K} + \mathbf{H}^T\boldsymbol{\Lambda}_B\mathbf{L} \\ \mathbf{K}^T\boldsymbol{\Lambda}_A\mathbf{H} + \mathbf{L}^T\boldsymbol{\Lambda}_B\mathbf{H} & \mathbf{K}^T\boldsymbol{\Lambda}_A\mathbf{K} + \mathbf{K}^T\boldsymbol{\Lambda}_B\mathbf{L} + \mathbf{L}^T\boldsymbol{\Lambda}_B\mathbf{K} + \mathbf{L}^T\boldsymbol{\Lambda}_C\mathbf{L} \end{bmatrix}. \tag{3.23}$$

With (3.23) we can now easily compute the CRLB for the estimates of the position by inversion of the FIM. The bounds for the variances of the $\hat{x}$ and $\hat{y}$ estimates are given by

$$\mathrm{var}\{\hat{x}\} \geq [\mathbf{J}_{\boldsymbol{\theta}}(\boldsymbol{\theta})^{-1}]_{1,1}, \ \mathrm{var}\{\hat{y}\} \geq [\mathbf{J}_{\boldsymbol{\theta}}(\boldsymbol{\theta})^{-1}]_{2,2}. \tag{3.24}$$

Note that we wrote the FIM as a function of $\boldsymbol{\theta}$, while the elements of $\mathbf{J}_{\boldsymbol{\psi}}(\boldsymbol{\psi})$ were parametrized by $\boldsymbol{\psi}$. This is of course valid, since we can express the elements of $\boldsymbol{\psi}$ as a function of $\boldsymbol{\theta}$. However, $\boldsymbol{\theta}$ also contains the clock offset ξ, but its value does not affect the FIM. Consequently it would be appropriate to write $\mathbf{J}_{\boldsymbol{\theta}}(\mathbf{p}, \boldsymbol{\alpha}_R, \boldsymbol{\alpha}_I)$, but for simplicity we will keep the current notation.

Hereby, we have succeeded in computing the CRLB of the position estimates. But for several reasons the result (3.23) is not satisfying:

- It gives us no insight, how the different parameters affect the CRLB.

- The high dimensionality of the matrix and the matrix inversion makes it difficult to learn about the relevant terms.
- A geometrical interpretation is not possible.

3.4.4 Equivalent FIM and Position Error Bound

We saw in the previous section that the FIM is a matrix of high dimensionality, which makes further analysis difficult. To simplify the problem we will use the notion of the EFIM and the definition of the PEB, which were both introduced in [2] and also used in [6].

The EFIM allows to formulate the CRLB specifically for the parameter of interest (in our case the agent position $\mathbf{p}$) as opposed to the whole parameter vector $\boldsymbol{\theta}$, which also contains the nuisance parameters. The definition of the EFIM results from the property, that principal submatrices of a positive-semidefinite matrix are also positive-semidefinite. We have placed the position vector as the first entry of $\boldsymbol{\theta}$, therefore the covariance matrix $\mathbf{C}_{\hat{\mathbf{p}}}$ is the upper left submatrix of $\mathbf{C}_{\hat{\boldsymbol{\theta}}}$,

$$\mathbf{C}_{\hat{\boldsymbol{\theta}}} = \begin{bmatrix} \mathbf{C}_{\hat{\mathbf{p}}} & \cdots \\ \cdots & \cdots \end{bmatrix}.$$

Formulating (3.4) using $\mathbf{C}_{\hat{\mathbf{p}}}$ results in

$$\mathbf{C}_{\hat{\boldsymbol{\theta}}} - \mathbf{J}_{\boldsymbol{\theta}}^{-1}(\boldsymbol{\theta}) = \begin{bmatrix} \mathbf{C}_{\hat{\mathbf{p}}} - [\mathbf{J}_{\boldsymbol{\theta}}^{-1}(\boldsymbol{\theta})]_{2\times 2} & \cdots \\ \cdots & \cdots \end{bmatrix} \succeq \mathbf{0}\ .$$

Here the matrix $\mathbf{C}_{\hat{\mathbf{p}}} - [\mathbf{J}_{\boldsymbol{\theta}}^{-1}(\boldsymbol{\theta})]_{2\times 2}$ is a principal submatrix of $\mathbf{C}_{\hat{\boldsymbol{\theta}}} - \mathbf{J}_{\boldsymbol{\theta}}^{-1}(\boldsymbol{\theta})$, therefore it is positive-semidefinite too. With the definition of the EFIM $\mathbf{J}_{\mathbf{p}}(\boldsymbol{\theta}) \in \mathbb{R}^{2\times 2}$ satisfying

$$\mathbf{J}_{\mathbf{p}}^{-1} = [\mathbf{J}_{\boldsymbol{\theta}}^{-1}]_{2\times 2}, \tag{3.25}$$

we can express the CRLB for the position by using the following inequality

$$\mathbf{C}_{\hat{\mathbf{p}}} - \mathbf{J}_{\mathbf{p}}^{-1}(\boldsymbol{\theta}) \succeq \mathbf{0}\ . \tag{3.26}$$

As we can see the EFIM is still parametrized by $\boldsymbol{\theta}$. However, in contrast to the original FIM it assembles the influence of all the parameters on the position estimates in a 2×2 matrix.

The reduced dimensionality of the EFIM makes further analysis much easier. In addition the formulation of the CRLB using (3.26) allows to make a statement about the concentration ellipse, which was introduced in Section 3.2, Eq. (3.2), as a measure for the estimator performance. In [25] it is shown, that the minimum size of the concentration ellipse (3.2) of any unbiased estimator is bounded by the ellipse

$$\mathcal{E}_{min} = \left\{ \mathbf{p}_{eq} \in \mathbb{R}^2 : (\mathbf{p}_{eq} - \mathbf{p})^T \mathbf{J}_{\mathbf{p}} (\mathbf{p}_{eq} - \mathbf{p}) = C^2 \right\},\ C \in \mathbb{R}. \tag{3.27}$$

From now in we will use $C = 1$ and refer to the resulting ellipses as *error ellipses*. Similar as for the concentration ellipse its size is determined by the eigenvalues of $\mathbf{J}_{\mathbf{p}}^{-1}$, while the orientation is defined by its eigenvectors. Because of the importance of this result, it is worth to notice again: By computing the EFIM (3.25), we immediately obtain the bound of the concentration ellipse

of any unbiased estimator. This is illustrated in Fig. 3.1, where also the lengths of the minor and major axes are indicated.

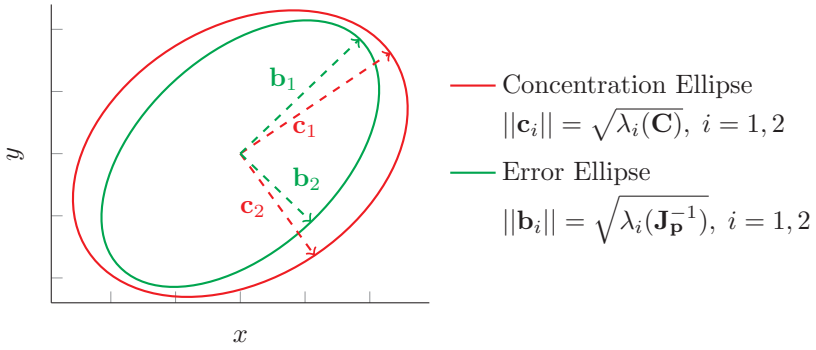

Figure 3.1: *Illustration of an error ellipse and a concentration ellipse: The minimum size of the concentration ellipse of any unbiased estimator is bounded by the error ellipse* (3.27)*. The axes of the ellipses are denoted as* $\mathbf{b}_i$ *and* $\mathbf{c}_i$*.*

With the EFIM we can also introduce the scalar PEB which is defined as [2]

$$\text{PEB} := \sqrt{\text{Tr}\left(\mathbf{J}_\mathbf{p}^{-1}\right)} = \sqrt{||\mathbf{b}_1||^2 + ||\mathbf{b}_2||^2}\ . \tag{3.28}$$

It is especially helpful to visualize the localization performance across a floor plan. Furthermore, it can be easily seen that the PEB represents a performance measure independent of the coordinate system, i.e. a rotation of the coordinate system does not affect the PEB.

We will now compute the EFIM for the given problem. The position vector $\mathbf{p}$ was placed as the first element in $\boldsymbol{\theta}$. This arrangement makes it possible to compute the EFIM using the Schur Complement,

$$\begin{bmatrix}\mathbf{A} & \mathbf{B}\\ \mathbf{C} & \mathbf{D}\end{bmatrix}^{-1} = \begin{bmatrix}(\mathbf{A} - \mathbf{B}\mathbf{D}^{-1}\mathbf{C})^{-1} & \dots\\ \dots & \dots\end{bmatrix}\ .$$

Now we need to take care that the matrix $\mathbf{A}$ represents the upper left 2×2 submatrix of $\mathbf{J}_{\boldsymbol{\theta}}(\boldsymbol{\theta})$ (3.23), and the matrices $\mathbf{B} \dots \mathbf{D}$ represent the remaining parts of the FIM. Then the EFIM is given by

$$\mathbf{J}_\mathbf{p} = \mathbf{A} - \mathbf{B}\mathbf{D}^{-1}\mathbf{C}.$$

This does not require a repartitioning, and we define the submatrices as

$$\mathbf{A} := \mathbf{H}^T\boldsymbol{\Lambda}_A\mathbf{H} \qquad \mathbf{A} \in \mathbb{R}^{2\times 2}\ , \tag{3.29}$$

$$\mathbf{B} = \mathbf{C}^T := \mathbf{H}^T\boldsymbol{\Lambda}_A\mathbf{K} + \mathbf{H}^T\boldsymbol{\Lambda}_B\mathbf{L} \qquad \mathbf{B}, \mathbf{C}^T \in \mathbb{R}^{2\times 2K+1}\ , \tag{3.30}$$

$$\mathbf{D} := \mathbf{K}^T\boldsymbol{\Lambda}_A\mathbf{K} + \mathbf{K}^T\boldsymbol{\Lambda}_B\mathbf{L} + \mathbf{L}^T\boldsymbol{\Lambda}_B\mathbf{K} + \mathbf{L}^T\boldsymbol{\Lambda}_C\mathbf{L} \qquad \mathbf{D} \in \mathbb{R}^{2K+1\times 2K+1}\ . \tag{3.31}$$

Finally, the 2×2 EFIM for the position estimates is given by

$$\begin{aligned}\mathbf{J_p} &= \mathbf{H}^T\mathbf{\Lambda}_A\mathbf{H} - (\mathbf{H}^T\mathbf{\Lambda}_A\mathbf{K} + \mathbf{H}^T\mathbf{\Lambda}_B\mathbf{L}) \\ &\quad (\mathbf{K}^T\mathbf{\Lambda}_A\mathbf{K} + \mathbf{K}^T\mathbf{\Lambda}_B\mathbf{L} + \mathbf{L}^T\mathbf{\Lambda}_B\mathbf{K} + \mathbf{L}^T\mathbf{\Lambda}_C\mathbf{L})^{-1}(\mathbf{K}^T\mathbf{\Lambda}_A\mathbf{H} + \mathbf{L}^T\mathbf{\Lambda}_B\mathbf{H}) \qquad (3.32a) \\ &= \mathbf{H}^T\big[\mathbf{\Lambda}_A - (\mathbf{\Lambda}_A\mathbf{K} + \mathbf{\Lambda}_B\mathbf{L})(\mathbf{K}^T\mathbf{\Lambda}_A\mathbf{K} + \mathbf{K}^T\mathbf{\Lambda}_B\mathbf{L} + \mathbf{L}^T\mathbf{\Lambda}_B\mathbf{K} + \mathbf{L}^T\mathbf{\Lambda}_C\mathbf{L})^{-1} \\ &\quad (\mathbf{K}^T\mathbf{\Lambda}_A + \mathbf{L}^T\mathbf{\Lambda}_B)\big]\mathbf{H}. \qquad (3.32b)\end{aligned}$$

When comparing (3.32a) with [6], then we can see that the first term $\mathbf{H}^T\mathbf{\Lambda}_A\mathbf{H}$ is exactly the result of the EFIM for TOA, under the condition that we neglect PO. From this we can immediately conclude, that the subtractive term in (3.32a) accounts for the estimation of the clock offset as well as for the influence of PO. Since the later also affects the estimation of the clock offset, it is difficult to distinguish the source of the deterioration. One possible way to gain more insight is to only consider the case where we neglect PO. This will help to quantify the influence of the clock offset with respect to the TOA scenario and will help us to find countermeasures. We will look at this case in detail in the following section.

3.4.5 Neglecting Path Overlap

As mentioned above, it makes sense to neglect PO in order to quantify the impact of the unknown clock offset. This means that we will now assume that we can always distinguish individual MPCs from each other, even if the arrival times are very close to each other and PO occurs. In reality this is clearly not always the case. However, there is also a different motivation for considering this case: Actually the information about positions where PO occurs is contained in the knowledge of the floor plan and anchor position. Therefore, one could reformulate the problem ignoring MPCs which lead to PO. This is actually a very reasonable approach when implementing an estimator as we will see in Chapter 4. From this point of view, considering the case when neglecting PO could even be more meaningful than the case where we account for PO.

We will start the analysis by going some steps back, and again look at the FIM $\mathbf{J}_{\boldsymbol{\psi}}(\boldsymbol{\psi})$ in (3.13). Note that all off-diagonal elements determine how the estimation of parameters is affected among the estimation of the others. For example the estimation of the amplitudes and arrival times of MPCs is connected, and they cannot be estimated individually. In $\mathbf{J}_{\boldsymbol{\psi}}(\boldsymbol{\psi})$ the submatrix $\mathbf{\Lambda}_B$ describes this dependency. $\mathbf{\Lambda}_A$ on the other hand describes the dependence between the estimation of the arrival times of individual MPCs. From intuition we can say that when assuming orthogonal signals from the VAs, $\mathbf{\Lambda}_A$ and $\mathbf{\Lambda}_C$ have to be diagonal since individual MPCs do not influence each other. Another way is to simply look at the case where no PO occurs, that is if the arrival times of the MPCs are sufficiently spaced in time,

$$|\tau_k - \tau_{k'}| \gg T_p,\ k, k' = 1 \dots K,\ k \neq k'.$$

For a transmit pulse with appropriate autocorrelation properties, the ACF $R_s(\tau_k - \tau_{k'})$ and also its derivatives will be zero. Therefore the FIM (3.13) is reduced to a diagonal matrix, i.e. $\mathbf{\Lambda}_A$ and $\mathbf{\Lambda}_C$ are diagonal, while $\mathbf{\Lambda}_B$ is a zero matrix. To indicate that we neglect PO, we will mark all used symbols with a tilde and write

$$\tilde{\mathbf{J}}(\boldsymbol{\psi}) = \begin{bmatrix} \tilde{\mathbf{\Lambda}}_A & \tilde{\mathbf{\Lambda}}_B \\ \tilde{\mathbf{\Lambda}}_B^T & \tilde{\mathbf{\Lambda}}_C \end{bmatrix} = \begin{bmatrix} \tilde{\mathbf{\Lambda}}_A & \mathbf{0} \\ \mathbf{0} & \tilde{\mathbf{\Lambda}}_C \end{bmatrix},$$

$$\tilde{\mathbf{\Lambda}}_A = \mathrm{diag}([\mathbf{\Lambda}_A]_{1,1}\ [\mathbf{\Lambda}_A]_{2,2}\ \dots\ [\mathbf{\Lambda}_A]_{K,K}), \qquad \tilde{\mathbf{\Lambda}}_C = \mathrm{diag}([\mathbf{\Lambda}_C]_{1,1}\ [\mathbf{\Lambda}_C]_{2,2}\ \dots\ [\mathbf{\Lambda}_C]_{K,K}).$$

Note that because of the diagonal structure of the FIM the CRLB of the arrival times are now given by the inverse of the corresponding diagonal elements,

$$\mathrm{var}\{\hat{\tau}_k\} \geq [\tilde{\mathbf{J}}(\boldsymbol{\psi})^{-1}]_{k,k} = [\tilde{\mathbf{\Lambda}}_A^{-1}]_{k,k} = \frac{1}{[\tilde{\mathbf{\Lambda}}_A]_{k,k}},\ 1 \leq k \leq K.$$

The diagonal elements of $\tilde{\mathbf{\Lambda}}_A$ play a major role not only when estimating the arrival times τ_k, but also when estimating the agent position. Therefore we take a closer look at these. From (3.14) follows for the diagonal elements with $k = k'$ [6]

$$\begin{aligned}[\mathbf{\Lambda}_A]_{k,k} &= 2\frac{|\alpha_k|^2}{N_0} w_k^2 \frac{\partial^2 R_s(\tau_k - \tau_{k'})}{\partial \tau_k \partial \tau_{k'}}\bigg|_{\tau_{k'}=\tau_k} = -2 \underbrace{\frac{|\alpha_k|^2}{N_0} w_k^2}_{\mathrm{SINR}_k} \underbrace{\frac{\partial^2 R_s(\tau)}{\partial \tau^2}\bigg|_{\tau=0}}_{-4\pi^2\beta^2} \\ &= 8\pi^2 \beta^2\, \mathrm{SINR}_k, \end{aligned} \tag{3.33}$$

where $\mathrm{SINR}_k = \frac{|\alpha_k|^2}{N_0} w_k^2$ is the SINR [6] of the k-th MPC, and β is the RMS bandwidth of the transmit pulse,

$$\beta^2 = \frac{\int_{-\infty}^{\infty} f^2 |S(f)|^2 \mathrm{d}f}{\int_{-\infty}^{\infty} |S(f)|^2 \mathrm{d}f}. \tag{3.34}$$

We assume that the energy of the transmit pulse is normalized to one, therefore the denominator of (3.34) is one and $\beta^2 = \int_{-\infty}^{\infty} f^2 |S(f)|^2 \mathrm{d}f$. The connection of the second derivative of the ACF and the effective bandwidth is derived by using the Fourier-transformation of the ACF,

$$\begin{aligned} &\mathcal{F}\{R_s(\tau)\} = |S(f)|^2, \\ &R_s(\tau) = \int_{-\infty}^{\infty} |S(f)|^2 \mathrm{e}^{j2\pi f\tau}\, \mathrm{d}f, \\ &\frac{\partial^2 R_s(\tau)}{\partial \tau^2}\bigg|_{\tau=0} = -4\pi^2 \int_{-\infty}^{\infty} f^2 |S(f)|^2 \mathrm{e}^{j2\pi f\tau} \mathrm{d}f \ \bigg|_{\tau=0} = -4\pi^2\beta^2. \end{aligned}$$

With (3.33) we can now express the CRLB for the arrival times estimates as

$$\mathrm{var}\{\hat{\tau}_k\} \geq [\tilde{\mathbf{J}}(\boldsymbol{\psi})^{-1}]_{k,k} = \frac{1}{8\pi^2\beta^2\, \mathrm{SINR}_k},\ 1 \leq k \leq K,$$

which clearly emphasizes the importance of the signal bandwidth and the SINRs of the MPCs. Therefore, a high signal bandwidth as well as high SINRs are beneficial for the estimation of arrival times.

Since the estimation of the agent position is closely related to the estimation of arrival times, we can already assume that the bandwidth and SINRs of the MPCs also play an important role for the EFIM $\tilde{\mathbf{J}}_{\mathbf{p}}$. We obtain $\tilde{\mathbf{J}}_{\mathbf{p}}$ by replacing the elements of $\mathbf{J}_{\boldsymbol{\psi}}(\boldsymbol{\psi})$ in (3.32a) by the elements of $\tilde{\mathbf{J}}_{\boldsymbol{\psi}}(\boldsymbol{\psi})$,

$$\tilde{\mathbf{J}}_{\mathbf{p}} = \mathbf{H}^T \tilde{\mathbf{\Lambda}}_A \mathbf{H} - (\mathbf{H}^T \tilde{\mathbf{\Lambda}}_A \mathbf{K})(\mathbf{K}^T \tilde{\mathbf{\Lambda}}_A \mathbf{K} + \mathbf{L}^T \tilde{\mathbf{\Lambda}}_C \mathbf{L})^{-1} (\mathbf{K}^T \tilde{\mathbf{\Lambda}}_A \mathbf{H}). \tag{3.35}$$

Note that this result has a minor flaw: we already saw that the arrival times can be estimated individually from the amplitudes, but now $\tilde{\mathbf{\Lambda}}_C$ appears, which clearly shows some inconsistence. However, in Appendix A.1 it is shown, that when plugging in the definitions of $\mathbf{H}$, $\mathbf{K}$ and $\mathbf{L}$ the matrix $\tilde{\mathbf{\Lambda}}_C$ vanishes, which confirms our idea.

I decided here to take another approach instead of plugging in the matrices. It is easier and it gives us more insight if we first compute a 3×3 EFIM $\mathbf{J}_{\mathbf{p},\xi}$ for a parameter vector $[\mathbf{p}^T\ \xi]^T$, and use this result to compute the 2×2 EFIM for $\mathbf{p}$. In order to compute $\mathbf{J}_{\mathbf{p},\xi}$ we partition the transformation matrix $\mathbf{T}$ slightly different,

$$\mathbf{T} = \left[\begin{array}{cc|c} \mathbf{H}_{K\times 2} & \mathbf{k}_{K\times 1} & \mathbf{0}_{K\times 2K} \\ \hline \mathbf{0}_{2K\times 2} & \mathbf{0}_{2K\times 1} & \mathbf{I}_{2K\times 2K} \end{array}\right] = \begin{bmatrix} \mathbf{G}_{K\times 3} & \mathbf{0} \\ \mathbf{0} & \mathbf{I}_{2K\times 2K} \end{bmatrix}, \tag{3.36}$$

with

$$\mathbf{G}_{K\times 3} = [\mathbf{H}_{K\times 2}\ \mathbf{k}_{K\times 1}]. \tag{3.37}$$

Applying the transformation and computing the EFIM results in

$$\mathbf{J}_{\mathbf{p},\xi} = \mathbf{G}^T\mathbf{\Lambda}_A\mathbf{G} - \mathbf{G}^T\mathbf{\Lambda}_B\mathbf{\Lambda}_C^{-1}\mathbf{\Lambda}_B^T\mathbf{G}.$$

When neglecting PO this reduces to

$$\begin{aligned} \tilde{\mathbf{J}}_{\mathbf{p},\xi} &= \mathbf{G}^T\tilde{\mathbf{\Lambda}}_A\mathbf{G} \\ &= 8\pi\beta^2 \sum_{k=1}^{K} \mathrm{SINR}_k\, \mathbf{J}_{\mathbf{r},3}(\phi_k), \end{aligned} \tag{3.38}$$

where $\mathbf{J}_{\mathbf{r},3}(\phi_k)$ is the matrix

$$\mathbf{J}_{\mathbf{r},3}(\phi_k) = \begin{bmatrix} \frac{1}{c^2}\cos^2(\phi_k) & \frac{1}{c^2}\cos(\phi_k)\sin(\phi_k) & \frac{1}{c}\cos(\phi_k) \\ \frac{1}{c^2}\cos(\phi_k)\sin(\phi_k) & \frac{1}{c^2}\sin^2(\phi_k) & \frac{1}{c}\sin(\phi_k) \\ \frac{1}{c}\cos(\phi_k) & \frac{1}{c}\sin(\phi_k) & 1 \end{bmatrix}.$$

When looking at the result (3.38), one can immediately see that it is in canonical form, i.e. it is given as the sum of the contributions of each VA. While the contribution of the k-th VA is scaled by its SINR, the whole EFIM is scaled by the effective bandwidth. The matrix $\mathbf{J}_{\mathbf{r},3}$ can be represented as

$$\mathbf{J}_{\mathbf{r},3}(\phi_k) = \mathbf{v}\mathbf{v}^T, \qquad \mathbf{v} = \begin{bmatrix} \frac{1}{c}\cos(\phi_k) & \frac{1}{c}\sin(\phi_k) & 1 \end{bmatrix}^T,$$

and is therefore a rank one matrix with one nonzero eigenvalue

$$\lambda_1(\mathbf{J}_{\mathbf{r},3}(\phi_k)) = ||\mathbf{v}||^2 = \frac{1}{c^2} + 1 \approx 1.$$

Therefore each VA adds information for the estimation of $\mathbf{p}$ and ξ.

From the result (3.38) we can now compute the EFIM $\tilde{\mathbf{J}}_{\mathbf{p}}$ by applying the Schur complement again. It can be expressed in a rather compact way with the introduction of the ranging direction

matrix $\mathbf{J}_r(\phi_k)$ [2] and an additional matrix $\mathbf{W}$ as

$$\tilde{\mathbf{J}}_{\mathbf{p}} = \frac{8\pi^2\beta^2}{c^2}\left[\sum_{k=1}^{K} \mathrm{SINR}_k\, \mathbf{J}_r(\phi_k) - \mathbf{W}\right], \tag{3.39}$$

with

$$\mathbf{J}_r(\phi_k) = \begin{bmatrix} \cos^2(\phi_k) & \cos(\phi_k)\sin(\phi_k) \\ \cos(\phi_k)\sin(\phi_k) & \sin^2(\phi_k) \end{bmatrix},$$

and

$$\mathbf{W} = \frac{1}{\sum_{k=1}^{K} \mathrm{SINR}_k}\mathbf{w}\mathbf{w}^T, \qquad \mathbf{w} = \begin{bmatrix} \sum_{k=1}^{K} \mathrm{SINR}_k \cos(\phi_k) & \sum_{k=1}^{K} \mathrm{SINR}_k \sin(\phi_k) \end{bmatrix}^T. \tag{3.40}$$

The result (3.39) finally allows some meaningful interpretation. When comparing it with the result for TOA in [6], i.e

$$\tilde{\mathbf{J}}_{\mathbf{p}}|_{\mathrm{toa}} = \frac{8\pi^2\beta^2}{c^2}\sum_{k=1}^{K} \mathrm{SINR}_k\, \mathbf{J}_r(\phi_k), \tag{3.41}$$

then the similarities between TDOA and TOA can clearly be seen: Every VA adds useful information for the estimation of the agent position in direction of ϕ_k, with the contribution being proportional to the SINR of the corresponding MPC. On the other hand, the difference between the two cases manifests itself with the subtraction of the scaled matrix $\mathbf{W}$, which therefore accounts for the influence of the clock offset estimation. From (3.40) we can clearly see that this is a rank one matrix with at maximum one nonzero eigenvalue

$$\lambda_1(\mathbf{W}) = \frac{1}{\sum_{k=1}^{K} \mathrm{SINR}_k}||\mathbf{w}||^2,$$

and the eigenvector $\mathbf{w}$. With the eigenvalue being $\lambda_1(\mathbf{W}) \geq 0$, the matrix $\mathbf{W}$ is a positive-semidefinite matrix, which means that its subtraction can reduce the information provided by the VAs. Therefore we can argue similar as in Section 3.4.4 that the minimum size of the error ellipse for TDOA is bounded by the error ellipse of the TOA system. From this property follows the inequality

$$\widetilde{\mathrm{PEB}}_{\mathrm{TDOA}} \geq \widetilde{\mathrm{PEB}}_{\mathrm{TOA}}. \tag{3.42}$$

Equality of the localization performance of TOA and TDOA is obtained for the rather unrealistic case where $\mathbf{W} = \mathbf{0}$. This case can theoretically occur, e.g. if the agent is surrounded by VAs with identical SINRs but from opposite directions. This scenario is illustrated in Fig. 3.2. Note that at least the SINRs of opposing VAs needs to be equal.

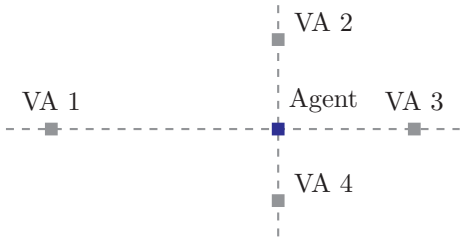

Figure 3.2: *Case study: Difference TDOA and TOA. We assume equal SINRs for all VAs. Then the condition for* $\mathbf{W} = \mathbf{0}$ *is fulfilled, therefore the TDOA system shows no performance loss compared to the TOA system.*

3.4.6 CRLB for the Estimation of the Clock Offset

With the results from the previous section the investigation of the single-anchor case is mainly done. However, from the 3×3 EFIM $\tilde{\mathbf{J}}_{\mathbf{p},\xi}$ (3.38) we can not only derive the EFIM for the position estimation, but also for the clock offset estimation. Although this is not the focus of this thesis, it is still interesting to see how well the estimation of the clock offset is possible, and how it affects the position estimation. The result is also of interest when performing the numerical evaluation in Section 3.6.2, since it gives us some hint on the requirements on suitable synchronization.

The derivation is only performed for the case when neglecting PO, and is carried out analogously to the one in Section 3.4.5. The equivalent Fisher information $\tilde{J}_\xi$ for the clock offset estimation is then given by

$$\tilde{J}_\xi = 8\pi\beta^2 \left[\sum_{k=1}^{K} \mathrm{SINR}_k - \mathbf{w}^T \left(\sum_{k=1}^{K} \mathrm{SINR}_k \, \mathbf{J}_r(\phi_k) \right)^{-1} \mathbf{w} \right]. \tag{3.43}$$

First of all the Fisher information is again scaled by the effective bandwidth, which shows the beneficial influence of a high signal bandwidth. Then the first term $\sum_{k=1}^{K} \mathrm{SINR}_k$ accumulates the contribution of each VA. The contributions are again weighted by the SINRs of the MPCs. The subtractive term accounts for the influence of the geometry.

For the rather unrealistic case where $\mathbf{w} = \mathbf{0}$, only the number of visible VAs and their SINRs determine the Fisher information. These geometrical conditions were already discussed in the previous section. Note that in this case we can estimate the clock offset even if the agent is not locatable, i.e. $\tilde{\mathbf{J}}_\mathbf{p}$ is singular. An example scenario, where an agent is located on the axis between two VAs, is illustrated in Fig. 3.3 (a). Here localization is not possible, since we do not have contributions from orthogonal directions. But if we assume equal SINRs from both VAs, then clock offset estimation is possible.

In the case that $\mathbf{w} \neq \mathbf{0}$, the matrix $\sum_{k=1}^{K} \mathrm{SINR}_k \, \mathbf{J}_r(\phi_k)$ affects the clock offset estimation. Note the similarity of this matrix with the EFIM for TOA (3.41). Provided that the agent is locatable, this matrix is always positive definite. This also holds for its inverse, meaning that

$$\mathbf{w}^T \left(\sum_{k=1}^{K} \mathrm{SINR}_k \, \mathbf{J}_r(\phi_k) \right)^{-1} \mathbf{w} \geq 0, \qquad \text{where equality holds only if } \mathbf{w} = \mathbf{0}.$$

A borderline case is illustrated in Fig. 3.3 (b) : It is understandable that here neither clock offset

(a) Clock offset estimation possible

(b) Clock offset estimation not possible

Figure 3.3: *Case study: Estimation of the clock offset. In (a) a scenario is shown, where perfect clock estimation is possible when having equal SINRs from both VAs, although localization is not possible. On the other hand in (b) the estimation of the clock offset is not possible when not having prior knowledge about the agent position.*

estimation nor localization are feasible. However, if we think of a slightly different scenario, where the agent is locatable, then we can see that the subtractive term of $\tilde{J}_\xi$ is reduced, the better the position estimation is possible. I.e. if the geometric alignment allows good localization performance in terms of TOA, also the performance of the clock offset estimation is increased, enabled by a smaller subtractive term. This again shows the connection of agent localization and clock offset estimation.

From the Fisher information (3.43) the bound for the variance of unbiased estimates is computed by inversion. With the definition of the clock error bound (CEB)

$$\mathrm{CEB} = \sqrt{J_\xi^{-1}}$$

we can express the bound of the standard deviation $\sigma_{\hat{\xi}}$ of the estimates as

$$\sigma_{\hat{\xi}} = \sqrt{\mathrm{var}\left\{\hat{\xi}\right\}} \geq \mathrm{CEB}.$$

3.5 Localization using Multiple Anchors

We will now derive the CRLB for a multipath-assisted indoor localization system using multiple anchors given the assumptions made in Section 2.7. Now the position estimation is based on multiple observations, but all from different anchors. Note that it is well known, that the FIM is additive for multiple independent observations. However, this is not helpful in the present case, since the FIMs associated with the different anchors differ in their dimensions, and are all parametrized differently. But the question arises, whether the EFIM instead of the FIM is additive in the present scenario. In order to find an answer we will derive the EFIMs for the two cases described in Section 2.7: having multiple anchors with and without synchronization.

For the derivation of the EFIM we choose the same approach as before: We first compute the FIM for the multipath parameters, and then derive the CRLB for the position by using a parameter transformation. We start by again formulating the observation as a vector consisting of the signals from the individual anchors,

$$\mathbf{r}_\mathrm{M} = [\mathbf{r}^{(1)^T}\ \mathbf{r}^{(2)^T}\ \ldots\ \mathbf{r}^{(J)^T}]^T.$$

Deriving its PDF requires the definition of the parameter vector $\boldsymbol{\psi}_\mathrm{M}$. It is beneficial to stack

the parameter vectors of the MPCs of the individual anchors as follows,

$$\boldsymbol{\psi}_{\mathrm{M}} = [{\boldsymbol{\psi}^{(1)}}^T, {\boldsymbol{\psi}^{(2)}}^T, \ldots, {\boldsymbol{\psi}^{(J)}}^T]^T.$$

Note that the number of MPCs from each anchor can be different and therefore the number of elements differs for each $\boldsymbol{\psi}^{(j)}$. The definition of $\boldsymbol{\psi}_{\mathrm{M}}$ enables us to express the joint PDF for $\mathbf{r}_{\mathrm{M}}$, which is also the desired LHF for the combined parameter vector $\boldsymbol{\psi}_{\mathrm{M}}$. Since all $\mathbf{r}^{(j)}$ are independent from each other, we obtain the joint PDF by multiplying the PDFs $f^{(j)}\left(\mathbf{r}^{(j)}; \boldsymbol{\psi}^{(j)}\right)$ of the individual anchors. The likelihood for $\boldsymbol{\psi}_{\mathrm{M}}$ is then given by

$$f_{\mathrm{M}}(\mathbf{r}_{\mathrm{M}}; \boldsymbol{\psi}_{\mathrm{M}}) = \prod_{j=1}^{J} f^{(j)}\left(\mathbf{r}^{(j)}; \boldsymbol{\psi}^{(j)}\right),$$

and the log-LHF is

$$\ln\ f_{\mathrm{M}}(\mathbf{r}_{\mathrm{M}}; \boldsymbol{\psi}_{\mathrm{M}}) = \sum_{j=1}^{J} \ln\ f^{(j)}\left(\mathbf{r}^{(j)}; \boldsymbol{\psi}^{(j)}\right). \tag{3.44}$$

The FIM can again be computed using equation (3.5), which means that we have to partially derive the log-LHF with respect to the different multipath parameters. Since the parameters of different anchors are independent from each other – they are called orthogonal parameters – this is a fairly simple task – the derivatives are all equal to zero. The remaining nonzero elements are given by the ones of FIMs $\mathbf{J}^{(j)}_{\boldsymbol{\psi}^{(j)}}$ from the individual anchors, which allows to formulate the final FIM as

$$\mathbf{J}_{\boldsymbol{\psi}_{\mathrm{M}}} = \begin{bmatrix} \mathbf{J}^{(1)}_{\boldsymbol{\psi}^{(1)}} & & \\ & \ddots & \\ & & \mathbf{J}^{(J)}_{\boldsymbol{\psi}^{(J)}} \end{bmatrix} = \mathrm{diag}\left(\mathbf{J}^{(1)}_{\boldsymbol{\psi}^{(1)}}, \mathbf{J}^{(2)}_{\boldsymbol{\psi}^{(2)}}, \ldots, \mathbf{J}^{(J)}_{\boldsymbol{\psi}^{(J)}}\right).$$

In order to compute the EFIM and CRLB for the agent position, we have to perform the parameter vector transformation. This transformation depends on the used topology, i.e. if the anchors are synchronized or not. We will examine these different cases in the next two sections.

3.5.1 Multiple Transmitting Anchors without Synchronization

We first consider the case where each anchor is operating on its own, without any synchronization at all. That means we can express the arrival times of the MPCs from the j-th anchor as

$$\tau_k^{(j)} = \frac{1}{c}\|\mathbf{p} - \mathbf{p}_k^{(j)}\| + \xi^{(j)},$$

which means that the MPCs of each anchor are delayed by its individual clock offset. The corresponding stacked parameter vector is given as

$$\boldsymbol{\theta}_{\mathrm{M}} = [\mathbf{p}^T, \xi^{(1)}, {\boldsymbol{\alpha}_R^{(1)}}^T, {\boldsymbol{\alpha}_I^{(1)}}^T, \xi^{(2)}, {\boldsymbol{\alpha}_R^{(2)}}^T, {\boldsymbol{\alpha}_I^{(2)}}^T, \ldots \xi^{(J)}, {\boldsymbol{\alpha}_R^{(J)}}^T, {\boldsymbol{\alpha}_I^{(J)}}^T]^T.$$

In $\boldsymbol{\theta}_\mathrm{M}$ the clock offset and path-amplitudes of each anchor are grouped together. This allows us to write the transformation matrix using the submatrices $\mathbf{H}$, $\mathbf{K}$ and $\mathbf{L}$, which were already defined in (3.20-3.22). Of course, it is necessary to adapt the dimensions and definitions of these matrices to match the corresponding anchors. The transformation matrix has then the form

$$\mathbf{T}_\mathrm{M} = \frac{\partial \boldsymbol{\psi}_\mathrm{M}}{\partial \boldsymbol{\theta}_\mathrm{M}} = \begin{bmatrix} \mathbf{H}^{(1)} & \mathbf{K}^{(1)} & & & \\ & \mathbf{L}^{(1)} & & & \\ \mathbf{H}^{(2)} & & \mathbf{K}^{(2)} & & \\ & & \mathbf{L}^{(2)} & & \\ \vdots & & & \ddots & \\ \mathbf{H}^{(J)} & & & & \mathbf{K}^{(J)} \\ & & & & \mathbf{L}^{(J)} \end{bmatrix}.$$

Applying the transformation yields the matrix

$$\begin{aligned} \mathbf{J}_{\boldsymbol{\theta}_\mathrm{M}} &= \mathbf{T}_\mathrm{M}^T \mathbf{J}_{\boldsymbol{\psi}_\mathrm{M}} \mathbf{T}_\mathrm{M} \\ &= \begin{bmatrix} \sum_{j=1}^{J} \mathbf{H}^{(j)T} \boldsymbol{\Lambda}_A^{(j)} \mathbf{H}^{(j)} & \mathbf{H}^{(1)T} \boldsymbol{\Lambda}_A^{(1)} \mathbf{K}^{(1)} + \mathbf{H}^{(1)T} \boldsymbol{\Lambda}_B^{(1)} \mathbf{L}^{(1)} & \cdots & \mathbf{H}^{(J)T} \boldsymbol{\Lambda}_A^{(J)} \mathbf{K}^{(J)} + \mathbf{H}^{(J)T} \boldsymbol{\Lambda}_B^{(J)} \mathbf{L}^{(J)} \\ \mathbf{K}^{(1)T} \boldsymbol{\Lambda}_A^{(1)} \mathbf{H}^{(1)} + \mathbf{L}^{(1)T} \boldsymbol{\Lambda}_B^{(1)T} \mathbf{H}^{(1)} & \mathbf{K}^{(1)T} \boldsymbol{\Lambda}_A^{(1)} \mathbf{K}^{(1)} + \mathbf{K}^{(1)T} \boldsymbol{\Lambda}_B^{(1)} \mathbf{L}^{(1)} + \mathbf{L}^{(1)T} \boldsymbol{\Lambda}_B^{(1)} \mathbf{K}^{(1)} + \mathbf{L}^{(1)T} \boldsymbol{\Lambda}_C^{(1)} \mathbf{L}^{(1)} & & \\ \vdots & & \ddots & \\ \mathbf{K}^{(J)T} \boldsymbol{\Lambda}_A^{(J)} \mathbf{H}^{(J)} + \mathbf{L}^{(J)T} \boldsymbol{\Lambda}_B^{(J)T} \mathbf{H}^{(J)} & & & \mathbf{K}^{(J)T} \boldsymbol{\Lambda}_A^{(J)} \mathbf{K}^{(J)} + \mathbf{K}^{(J)T} \boldsymbol{\Lambda}_B^{(J)} \mathbf{L}^{(J)} + \mathbf{L}^{(J)T} \boldsymbol{\Lambda}_B^{(J)} \mathbf{K}^{(J)} + \mathbf{L}^{(J)T} \boldsymbol{\Lambda}_C^{(J)} \mathbf{L}^{(J)} \end{bmatrix}. \end{aligned}$$

The structure of the FIM can be written as

$$\mathbf{J}_{\boldsymbol{\theta}_\mathrm{M}} = \begin{bmatrix} \sum_{j=1}^{J} \mathbf{A}^{(j)} & \mathbf{B}^{(1)} & \cdots & \mathbf{B}^{(J)} \\ \mathbf{B}^{(1)T} & \mathbf{D}^{(1)} & & \\ \vdots & & \ddots & \\ \mathbf{B}^{(J)T} & & & \mathbf{D}^{(J)} \end{bmatrix}, \tag{3.45}$$

where the submatrices $\mathbf{A}^{(j)}$, $\mathbf{B}^{(j)}$ and $\mathbf{D}^{(j)}$ are computed by adapting the definitions in (3.29-3.31) for the corresponding anchor. Computing the EFIM then yields

$$\begin{aligned} \mathbf{J}_\mathbf{p}\big|_{J \text{ anchors}} &= \sum_{j=1}^{J} \mathbf{A}^{(j)} - [\mathbf{B}^{(1)} \cdots \mathbf{B}^{(J)}] \begin{bmatrix} \mathbf{D}^{(1)} & & \\ & \ddots & \\ & & \mathbf{D}^{(J)} \end{bmatrix}^{-1} \begin{bmatrix} \mathbf{B}^{(1)T} \\ \vdots \\ \mathbf{B}^{(J)T} \end{bmatrix} \\ &= \sum_{j=1}^{J} \mathbf{A}^{(j)} - \mathbf{B}^{(j)} \mathbf{D}^{(j)-1} \mathbf{B}^{(j)T} \\ &= \sum_{j=1}^{J} \mathbf{J}_\mathbf{p}^{(j)}. \end{aligned}$$

The resulting EFIM is given as the sum of the EFIMs of the individual anchors, meaning that it is additive for multiple anchors without synchronization. This has the obvious advantage that it further reduces the PEB, prevents deterioration caused by PO, and enables better coverage in large indoor environments. When neglecting PO the EFIM is given by

$$\tilde{\mathbf{J}}_{\mathbf{p}}\big|_{J \text{ anchors}} = \frac{8\pi^2\beta^2}{c^2}\left[\sum_{j=1}^{J}\sum_{k=1}^{K}\mathrm{SINR}_k\,\mathbf{J}_r^{(j)}(\phi_k) - \mathbf{W}_{\mathrm{M}}\right], \tag{3.46}$$

where the subtractive term $\mathbf{W}_{\mathrm{M}}$ consists of the sum off all $\mathbf{W}^{(j)}$ as defined in (3.40),

$$\mathbf{W}_{\mathrm{M}} = \sum_{j=1}^{J}\mathbf{W}^{(j)}.$$

Since all $\mathbf{W}^{(j)}$ are positive semidefinite matrices, equal performance as for the corresponding TOA system is achieved, if the condition $\mathbf{W}^{(j)} = \mathbf{0}$ is fulfilled for each anchor. This condition was already discussed in Sections 3.4.5, and indicates that this case is not very relevant for practical scenarios.

3.5.2 Multiple Synchronized Transmitting Anchors

When considering synchronization between the anchors, we assume that all anchors have equal clock offsets $\xi^{(1)} = \cdots = \xi^{(J)} = \xi$ resulting in equal delay for the arrival times of all MPCs,

$$\tau_k^{(j)} = \frac{1}{c}\|\mathbf{p} - \mathbf{p}_k^{(j)}\| + \xi.$$

Consequently the resulting parameter vector can be formulated as

$$\boldsymbol{\theta}_{Ms} = [\mathbf{p}^T, \xi, \boldsymbol{\alpha}_R^{(1)^T}, \boldsymbol{\alpha}_I^{(1)^T}, \boldsymbol{\alpha}_R^{(2)^T}, \boldsymbol{\alpha}_I^{(2)^T}, \dots \boldsymbol{\alpha}_R^{(J)^T}, \boldsymbol{\alpha}_I^{(J)^T}]^T.$$

In the previous section the EFIM for the anchor position turned out to be additive. Now that the contributions from all anchors share the same agent position $\mathbf{p}$ and clock offset ξ, this suggests the additivity of the 3×3 EFIMs $\mathbf{J}_{\mathbf{p},\xi}^{(j)}$. With this in mind, we partition the transformation matrix in a way, which simplifies the computation of the 3×3 EFIM afterwards. In this case it shows a clear similarity to (3.36) which utilizes the matrix $\mathbf{G} \in \mathbb{R}^{K\times 3}$ (3.37). Adapting this matrix to account for the different number of MPCs by each anchor, leads to the matrices $\mathbf{G}^{(j)} \in \mathbb{R}^{K^{(j)}\times 3}$. The transformation matrix $\mathbf{T}_{\mathrm{M}}$ is then given by

$$\mathbf{T}_{Ms} = \frac{\partial \boldsymbol{\psi}_{\mathrm{M}}}{\partial \boldsymbol{\theta}_{Ms}} = \begin{bmatrix} \mathbf{G}^{(1)} & & & & \\ & \mathbf{I}^{(1)} & & & \\ \mathbf{G}^{(2)} & & & & \\ & & \mathbf{I}^{(2)} & & \\ \vdots & & & \ddots & \\ \mathbf{G}^{(J)} & & & & \\ & & & & \mathbf{I}^{(J)} \end{bmatrix},$$

with $\mathbf{I}^{(j)}$ being identity matrices with dimensions $2K^{(j)} \times 2K^{(j)}$. Applying the parameter transformation leads to the FIM $\mathbf{J}_{\boldsymbol{\theta}_{Ms}}$ for the parameter vector $\boldsymbol{\theta}_{Ms}$,

$$\begin{aligned}\mathbf{J}_{\boldsymbol{\theta}_{Ms}} &= \mathbf{T}_{Ms}^T \mathbf{J}_{\boldsymbol{\psi}_{\mathrm{M}}} \mathbf{T}_{Ms} \\ &= \begin{bmatrix} \sum_{j=1}^{J} \mathbf{G}^{(j)^T} \boldsymbol{\Lambda}_A^{(j)} \mathbf{G}^{(j)} & \mathbf{G}^{(1)^T} \boldsymbol{\Lambda}_B^{(1)} & \cdots & \mathbf{G}^{(J)^T} \boldsymbol{\Lambda}_B^{(J)} \\ \boldsymbol{\Lambda}_B^{(1)^T} \mathbf{G}^{(1)} & \boldsymbol{\Lambda}_C^{(1)} & & \\ \vdots & & \ddots & \\ \boldsymbol{\Lambda}_B^{(J)^T} \mathbf{G}^{(J)} & & & \boldsymbol{\Lambda}_C^{(J)} \end{bmatrix}.\end{aligned}$$

The computation of the 3×3 EFIM verifies our previous assumption about the additivity of the 3×3 EFIM,

$$\mathbf{J}_{\mathbf{p},\xi}\big|_{J \text{ synced anchors}} = \sum_{j=1}^{J} \left[\mathbf{G}^{(j)^T} \boldsymbol{\Lambda}_A^{(j)} \mathbf{G}^{(j)} - \mathbf{G}^{(j)^T} \boldsymbol{\Lambda}_B^{(j)} \boldsymbol{\Lambda}_C^{(j)^{-1}} \boldsymbol{\Lambda}_B^{(j)^T} \mathbf{G}^{(j)} \right].$$

Note that the expression in the sum is exactly the 3×3 EFIM $\mathbf{J}_{\mathbf{p},\xi}^{(j)}$. As it can be seen, when using multiple synchronized anchors, we have to sum up the 3×3 EFIMs from the individual anchors,

$$\mathbf{J}_{\mathbf{p},\xi}\big|_{J \text{ synced anchors}} = \sum_{j=1}^{J} \mathbf{J}_{\mathbf{p},\xi}^{(j)}.$$

In order to compute the EFIM for the agent position, it is necessary to again partition the 3×3 EFIM and compute the Schur complement. This is straight forward, therefore we will only derive and analyze the EFIM for the case when neglecting PO. In this case the 3×3 EFIM reduces to

$$\begin{aligned}\tilde{\mathbf{J}}_{\mathbf{p},\xi}\big|_{J \text{ synced anchors}} &= \sum_{j=1}^{J} \mathbf{G}^{(j)^T} \tilde{\boldsymbol{\Lambda}}_A^{(j)} \mathbf{G}^{(j)} \\ &= 8\pi\beta^2 \sum_{j=1}^{J} \sum_{k=1}^{K} \mathrm{SINR}_k^{(j)} \begin{bmatrix} \frac{1}{c^2}\cos^2(\phi_k^{(j)}) & \frac{1}{c^2}\cos(\phi_k^{(j)})\sin(\phi_k^{(j)}) & \frac{1}{c}\cos(\phi_k^{(j)}) \\ \frac{1}{c^2}\cos(\phi_k^{(j)})\sin(\phi_k^{(j)}) & \frac{1}{c^2}\sin^2(\phi_k^{(j)}) & \frac{1}{c}\sin(\phi_k^{(j)}) \\ \frac{1}{c}\cos(\phi_k^{(j)}) & \frac{1}{c}\sin(\phi_k^{(j)}) & 1 \end{bmatrix}.\end{aligned} \tag{3.47}$$

The EFIM for the agent position is then given by

$$\tilde{\mathbf{J}}_{\mathbf{p}}\big|_{J \text{ synced anchors}} = \frac{8\pi^2\beta^2}{c^2} \left[\sum_{j=1}^{J} \sum_{k=1}^{K} \mathrm{SINR}_k \, \mathbf{J}_r^{(j)}(\phi_k) - \mathbf{W}_{Ms} \right], \tag{3.48}$$

with

$$\mathbf{W}_{Ms} = \frac{1}{\sum_{j=1}^{J}\sum_{k=1}^{K}\mathrm{SINR}_k^{(j)}} \begin{bmatrix} \sum_{j=1}^{J}\sum_{k=1}^{K}\mathrm{SINR}_k^{(j)}\cos(\phi_k^{(j)}) \\ \sum_{j=1}^{J}\sum_{k=1}^{K}\mathrm{SINR}_k^{(j)}\sin(\phi_k^{(j)}) \end{bmatrix} \begin{bmatrix} \sum_{j=1}^{J}\sum_{k=1}^{K}\mathrm{SINR}_k^{(j)}\cos(\phi_k^{(j)}) \\ \sum_{j=1}^{J}\sum_{k=1}^{K}\mathrm{SINR}_k^{(j)}\sin(\phi_k^{(j)}) \end{bmatrix}^T . \quad (3.49)$$

When looking at the result (3.47) and (3.48) we can see, that they basically have the same structure as the results (3.38) and (3.39) for a single anchor, when we think of the case where all VAs belong to this anchor. Note that when looking at the problem from this point of view, the above derivation was almost superfluous. The additional synchronized anchors just extend the set of used VAs. With the alternative definition of the parameter vector for the multipath components

$$\boldsymbol{\psi}'_{\mathrm{M}} = [\boldsymbol{\tau}'^T \; \boldsymbol{\alpha}_R'^T \; \boldsymbol{\alpha}_I'^T]^T,$$

with

$$\boldsymbol{\tau}' = [\boldsymbol{\tau}^{(1)T} \dots \boldsymbol{\tau}^{(J)T}]^T, \quad \boldsymbol{\alpha}'_R = [\boldsymbol{\alpha}_R^{(1)T} \dots \boldsymbol{\alpha}_R^{(J)T}]^T, \quad \boldsymbol{\alpha}'_I = [\boldsymbol{\alpha}_I^{(1)T} \dots \boldsymbol{\alpha}_I^{(J)T}]^T,$$

the similarity to the single-anchor based TDOA system becomes obvious, and we could directly specify the EFIM. This makes further discussions unnecessary.

3.5.3 Comparison of the Position Error Bound

Using multiple anchors has in any case (synchronized or not) obvious advantages compared to the scenario using a single anchor. Since the resulting EFIM is given as the sum of positive definite matrices[9], the CRLB and PEB are reduced, compared to the scenario with a single anchor. Even if one of the anchors would not be sufficient for localizing the agent on its own (i.e. its EFIM would be positive semidefinite), it in general still provides useful information for the overall localization problem. This has the obvious advantage that additional anchors not only reduces the PEB, but also prevents deterioration caused by PO, and enables better coverage in large indoor environments.

When directly comparing the scenarios considering multiple anchors with and without synchronization, it is difficult to state which one to prefer in terms of the CRLB. However, in the case with synchronized anchors we only have to estimate one clock offset ξ compared to the J clock offsets $\{\xi^{(j)}\}$. Therefore, the number of parameters to be estimated is smaller, which in general results in a decrease of the CRLB. Further statements can be made by looking at the sum of the eigenvalues of the EFIMs. Since the additive parts in (3.46) and (3.48) are equal, we will only look at the trace of the subtractive part. When neglecting PO we can derive the

[9] The EFIMs of the individual anchors are positive definite provided that the agent is locatable with a single anchor.

following inequality,

$$\begin{aligned}
\mathrm{Tr}\{\mathbf{W}_{Ms}\} &= \frac{1}{\sum_{j=1}^{J}\sum_{k=1}^{K}\mathrm{SINR}_k^{(j)}} \left\| \begin{bmatrix} \sum_{j=1}^{J}\sum_{k=1}^{K}\mathrm{SINR}_k^{(j)}\cos(\phi_k^{(j)}) \\ \sum_{j=1}^{J}\sum_{k=1}^{K}\mathrm{SINR}_k^{(j)}\sin(\phi_k^{(j)}) \end{bmatrix} \right\|^2 \\
&\leq \frac{1}{\sum_{j=1}^{J}\sum_{k=1}^{K}\mathrm{SINR}_k^{(j)}} \sum_{j=1}^{J} \left\| \begin{bmatrix} \sum_{k=1}^{K}\mathrm{SINR}_k^{(j)}\cos(\phi_k^{(j)}) \\ \sum_{k=1}^{K}\mathrm{SINR}_k^{(j)}\sin(\phi_k^{(j)}) \end{bmatrix} \right\|^2 \\
&= \sum_{j=1}^{J} \frac{1}{\sum_{j'=1}^{J}\sum_{k'=1}^{K}\mathrm{SINR}_{k'}^{(j')}} \left\| \begin{bmatrix} \sum_{k=1}^{K}\mathrm{SINR}_k^{(j)}\cos(\phi_k^{(j)}) \\ \sum_{k=1}^{K}\mathrm{SINR}_k^{(j)}\sin(\phi_k^{(j)}) \end{bmatrix} \right\|^2 \\
&\leq \sum_{j=1}^{J} \frac{1}{\sum_{k'=1}^{K}\mathrm{SINR}_{k'}^{(j)}} \left\| \begin{bmatrix} \sum_{k=1}^{K}\mathrm{SINR}_k^{(j)}\cos(\phi_k^{(j)}) \\ \sum_{k=1}^{K}\mathrm{SINR}_k^{(j)}\sin(\phi_k^{(j)}) \end{bmatrix} \right\|^2 \\
&= \mathrm{Tr}\{\mathbf{W}_M\}.
\end{aligned}$$

From this follows

$$\mathrm{Tr}\{\mathbf{J_p}\big|_{J \text{ synced anchors}}\} = \mathrm{Tr}\{\cdots\} - \mathrm{Tr}\{\mathbf{W}_{Ms}\} \geq \mathrm{Tr}\{\mathbf{J_p}\big|_{J \text{ anchors}}\} = \mathrm{Tr}\{\cdots\} - \mathrm{Tr}\{\mathbf{W}_M\}. \quad (3.50)$$

Remember that larger eigenvalues of the EFIM result in a reduced size of the error ellipse. Equation (3.50) indicates that in many cases the error ellipse is smaller when using multiple synchronized anchors compared to the case when not having synchronization. However, from the mathematical point of view this is not sufficient to state that the PEB is always lower for multiple synchronized anchors. In general, the smaller eigenvalue of the EFIM dominates the PEB as can be seen in the following,

$$\begin{aligned}
\mathrm{PEB} &= \sqrt{\mathrm{Tr}\{\mathbf{J_p}^{-1}\}} = \sqrt{\lambda_1(\mathbf{J_p}^{-1}) + \lambda_2(\mathbf{J_p}^{-1})} \\
&= \sqrt{\frac{1}{\lambda_1(\mathbf{J_p})} + \frac{1}{\lambda_2(\mathbf{J_p})}} \\
&\geq \sqrt{\frac{1}{\min(\lambda_1(\mathbf{J_p}), \lambda_2(\mathbf{J_p}))}}.
\end{aligned}$$

Although it might not be relevant in a practical scenario, we can always think of a case, where $\mathbf{W}_M$ affects the eigenvalues of the EFIM in a way, that the PEB is reduced compared to the case when considering synchronization, even if the inequality (3.50) is fulfilled. So, the PEB could also be smaller when using multiple anchors without synchronization. However, in Section 3.6.4 we will see, that in realistic scenarios the PEB is clearly reduced when using synchronized anchors.

3.6 Numerical Evaluation

The aim of this section is to gain a deeper understanding on how localization performance is affected by the presence of a clock offset. We will quantify the differences between TDOA and TOA, and verify the results from the previous sections. In addition, we also make statements about the robustness of the multipath-assisted indoor localization system by investigating on

the performance under conditions close to reality.

We perform the evaluation based on the theoretical foundations derived in the previous sections. These allow to compute the CRLB for an arbitrary position in the given indoor environment. For the visualization of the results we have the following possibilities:

- To get an overall feeling of the localization performance it is interesting to visualize the PEB across the floor plan. This approach is especially helpful to visualize its structure and provides helpful insight on the connections between the PEB and the room geometry. Examples for such illustrations are shown in Fig. 3.4. We always plot the logarithm of the PEB, and use the same coloring to make a comparison of the results possible.
- Beside these plots, we will also make use of cummulative distribution functions (CDFs), which enable a more quantitative comparison of the results. A CDF $F_{\mathrm{PEB}}(\mathrm{PEB})$ is then computed as

$$F_{\mathrm{PEB}}(\mathrm{PEB}) = \frac{1}{M} \sum_{m=1}^{M} \mathbf{1} \left(\mathrm{PEB}_m \leq \mathrm{PEB} \right),$$

  where M is the number of grid points across the floor plan, PEB_m is the PEB for the m-th grid point and $\mathbf{1}(\cdot)$ is the indicator function.
- Finally, we also use an illustration of the error ellipses across the floor plan to asses the 2D components of the CRLB.

Independent of the purpose of the evaluation, we will in most cases investigate the cases where we consider and where we neglect PO. As already stated, the former case leads to rather conservative results, whereas the later yields some more optimistic values for the PEB. When using a two column layout for the illustrations, we will from now on always show the result for the case when considering PO on the left hand side, whereas the results when neglecting PO are illustrated on the right hand side.

3.6.1 Simulation Issues

As already stated we will use the scenario described in Section 2.8 and the parameters defined in Tab. 2.1 for the evaluation. The CRLB is computed across the floor plan on a grid with 2 cm spacing in the x and y directions, i.e. this yields the CRLB for 160000 positions inside the room and allows to make meaningful statements about the performance bound.

When computing the CRLB some additional issues have to be taken into consideration. Especially, some of the assumptions under which the LHF is valid are violated. Not only that the RRC pulses are not perfectly orthogonal, but especially we inevitably have to deal with PO situations. When total PO occurs, the FIM is ill-conditioned and singular, yielding a PEB which approaches infinity. In the following evaluation theses situations have been prevented by simply adding a small offset of 3 mm in x and 7 mm in the y direction to all the grid points on which the CRLB is evaluated to avoid equal distances between the agent position and multiple anchors or VAs.

For the comparison with TOA we need to compute its CRLB. Therefore the result [6, Eq. (16)] was used, and Eq. (3.41) when neglecting PO.

3.6.2 Comparison of TOA and TDOA

As the title of the thesis suggests, we focus on the impact of the clock offset on localization performance. Assessing the impact requires to compare the localization performance with the case, where the clock offset is known. This leads us to the comparison of TDOA and TOA. We start with the single anchor scenario and will later treat the multiple-anchor case.

Fig. 3.4 shows the PEB for TDOA (a),(b) and TOA (c),(d) when considering (a),(c) or neglecting (b),(d) PO for the pulse duration $T_p = 1\,\text{ns}$. In any case the performance of the TDOA system is reduced in comparison to the TOA system. Although the overall structure is very similar, the results indicate at least at some areas an increase of the overall PEB. This is especially the case at positions where partial PO occurs, or where only a low number of VAs are visible as it can be seen in the lower right hand corner.

A more quantitative assessment is provided by evaluating the CDFs for the different cases. Fig. 3.5 shows a comparison of the CDFs for TDOA and TOA depending on the pulse duration, where (a) is for the case considering PO, and (b) when neglecting it. In both cases it confirms the inequality (3.42), which states that the performance of the TOA system must always be better or equal than for the TDOA system when considering the same scenario. It furthermore highlights that the differences between TDOA and TOA are reduced when decreasing the pulse duration. From this point of view, a TDOA system can easily achieve equal or even better localization performance as a TOA system when decreasing the pulse duration with respect to the TOA system.

Reducing the pulse duration not only leads to a better localization performance, but also decreases the influence of PO. This is shown in Fig. 3.6 which restricts itself to evaluating the influence of the pulse duration on the impact of PO.

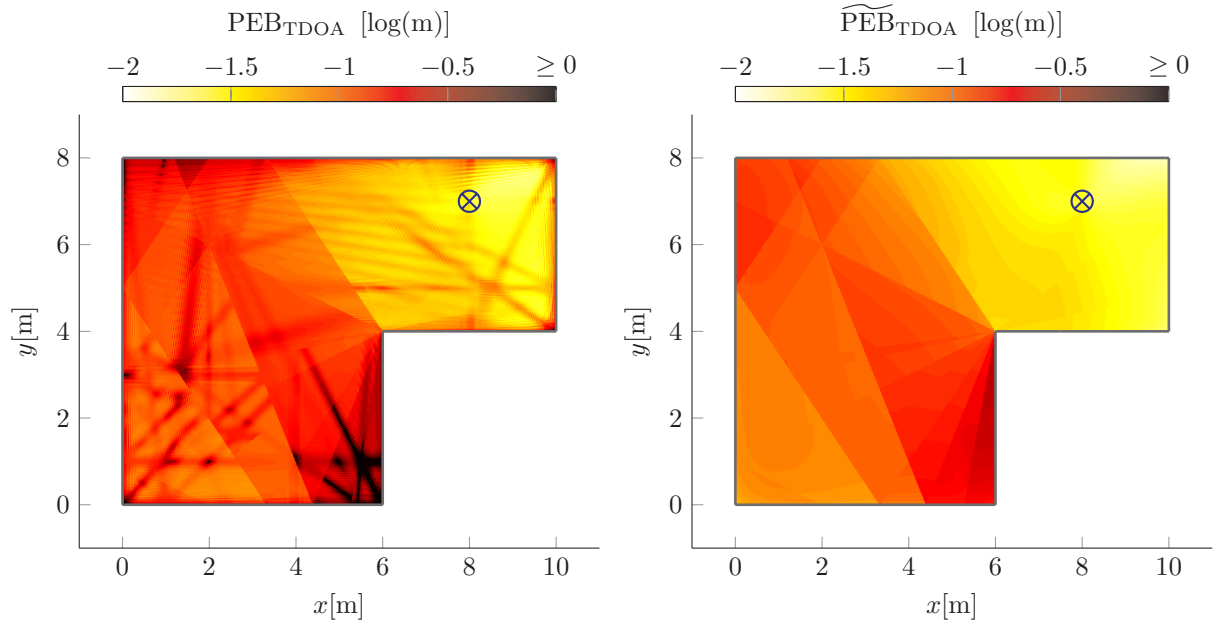

(a) TDOA, considering PO

(b) TDOA, neglecting PO

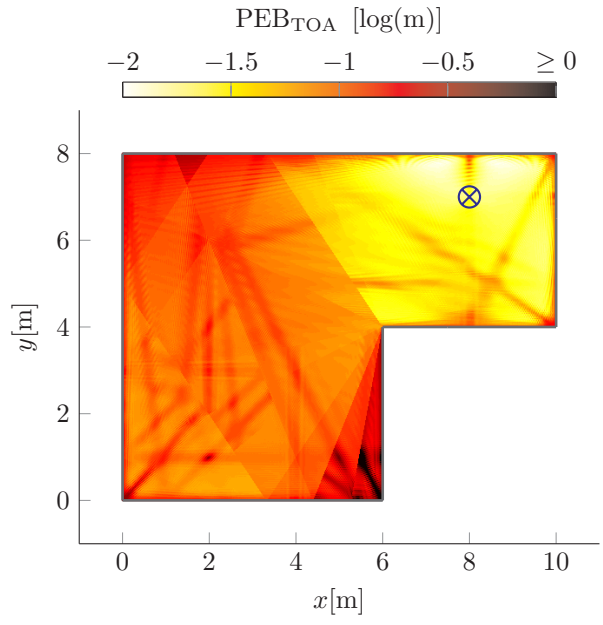

(c) TOA, considering PO

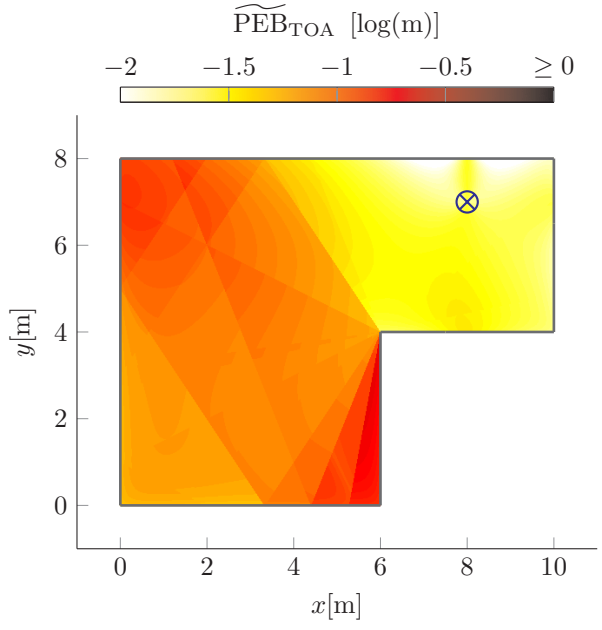

(d) TOA, neglecting PO

Figure 3.4: *Comparison of the PEB for TDOA and TOA across the floor plan. Each plot shows the logarithm of the PEB across the floor plan. The PEB was computed for the scenario described in Section 2.8 for a pulse duration of $T_p = 1$ ns. The PEB for TDOA (a,b) is clearly increased compared to the TOA case (c,d), especially in regions where PO occurs, or at positions where only few VAs are visible.*

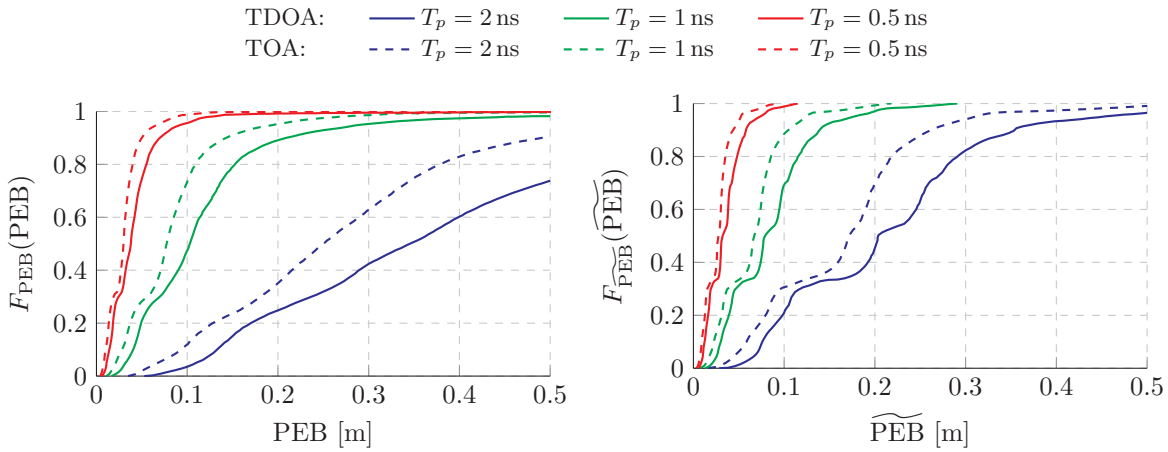

(a) TDOA vs. TOA, considering PO

(b) TDOA vs. TOA, neglecting PO

Figure 3.5: *CDF comparison of the PEBs for TDOA and TOA. TDOA (solid lines) is compared with TOA (dashed lines) for different pulse durations. A performance degradation of TDOA is clearly visible. However, when decreasing the pulse duration T_p the CDF for TDOA approaches the CDF for TOA. Furthermore the result suggests, that a TDOA system can achieve the performance of a TOA system by reducing the pulse duration.*

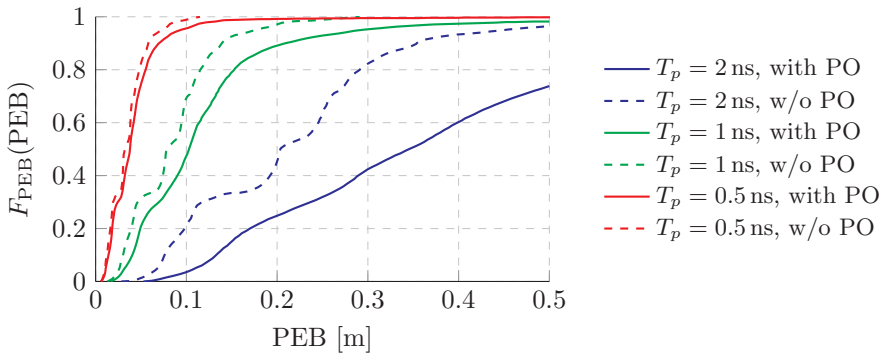

Figure 3.6: *CDF comparison for TDOA with and without PO. Decreasing the pulse duration T_p leads to a reduced influence of PO.*

A more convincing illustration of the structural changes is provided in Fig. 3.7, showing the actual differences between the PEB for TDOA and TOA, i.e. $\Delta\text{PEB} = \text{PEB}_{\text{TDOA}} - \text{PEB}_{\text{TOA}}$, again for the case with PO in (a) and when neglecting it in (b). As already mentioned, in (a) one can observe the increased influence of PO. In (b) it can be seen that, in general, regions with low VA visibilities are more affected by performance degradation. However, this is not true in general and we can clearly see some exceptions, e.g. in the lower right hand corner. We already saw in the theoretical analysis that the PEB depends on the number of visible VAs, the SINRs and also the influence of the geometry.

The previous observations lead to the comparison of the PEB degradation with the CEB, which is shown in Fig. 3.8. Now it is especially interesting to compare these results with Fig. 3.7. Note that the structure of the CEB is very similar to the structure of the difference of the PEB. Regions where the clock offset can be estimated well show little deterioration of the PEB, whereas bad clock offset estimation performance manifests itself with increased influence on the PEB. It clearly shows that the problems of clock offset estimation and position estimation are closely linked, and verifies the results which were found in the theoretical part in Section 3.4.5 and 3.4.6.

Motivated by these observations we now selectively determine the influence of the CEB on the PEB. Therefore, we only consider a limited area of the floor plan, where a certain CEB is achieved. Then the CDF of the PEB is computed for this area. The results can be seen in Fig. 3.9, and clearly show the importance of a low clock synchronization error. E.g. in order to achieve a reduction of the PEB of maximum 2 cm with respect to TOA with a coverage of more than 80% of the area, we need unbiased estimation of the clock offset with a standard deviation lower than $\sigma_{\hat{\xi}} \leq 0.1\,\text{ns}$. In contrast the area where we achieve $\sigma_{\hat{\xi}} > 0.1\,\text{ns}$ leads to a performance degradation in the range of almost 10 cm.

We complete the comparison by examining the influence on the error ellipses. Fig. 3.10, which shows some ellipses across the floor plan, makes the spreading and rotation of the ellipses clearly visible. It can be seen, that as already stated in Section 3.4.5, the error ellipses for TDOA are bounded by those of the TOA system, i.e. the performance of the TDOA system can never exceed the performance of the TOA system. From the result it can also be seen, that mainly the length of the minor axes of the ellipses are affected, resulting in a more even spread of the ellipses in the x and y directions. Also note that when comparing the ellipses for TOA and TDOA, the latter is only affected in one direction while it is not influenced in the orthogonal direction. This can be ascribed to the fact, that the matrix $\mathbf{W}$ in (3.39), which accounts for the influence of the clock offset, is of rank one with at maximum one nonzero eigenvalue.

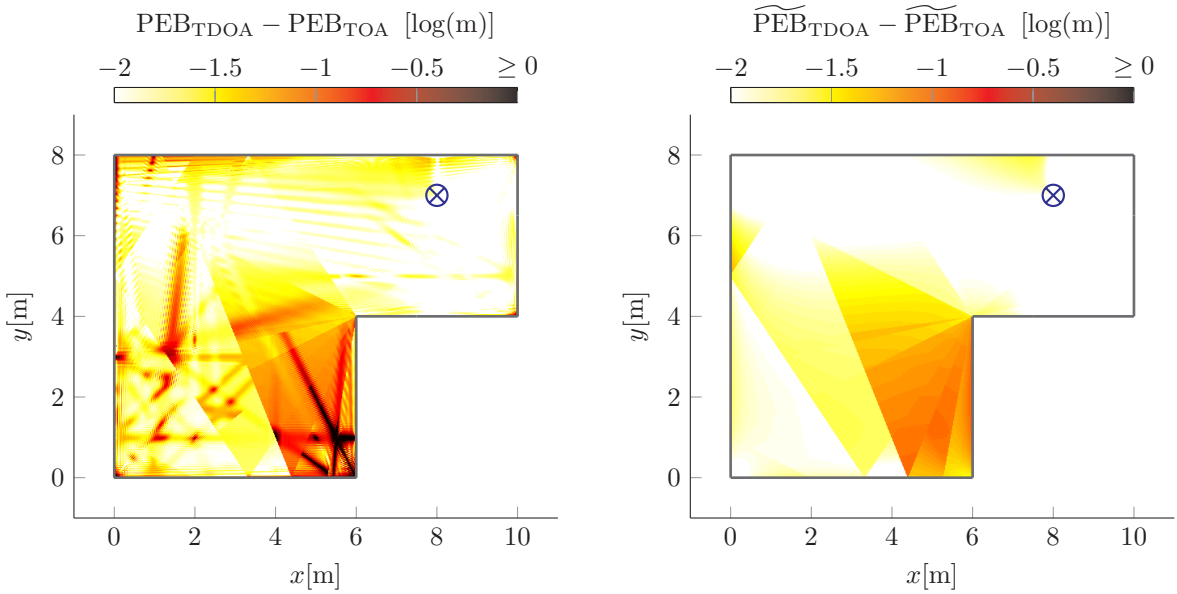

(a) Difference of the PEB between TDOA and TOA when considering PO

(b) Difference of the PEB between TDOA and TOA when neglecting PO

Figure 3.7: *Detailed difference of the PEBs between TDOA and TOA across the floor plan. This plot only shows the differences between the two cases, and shows an increase of the PEB for TDOA at positions affected by PO as well as in areas with low VA visibility (with exceptions).*

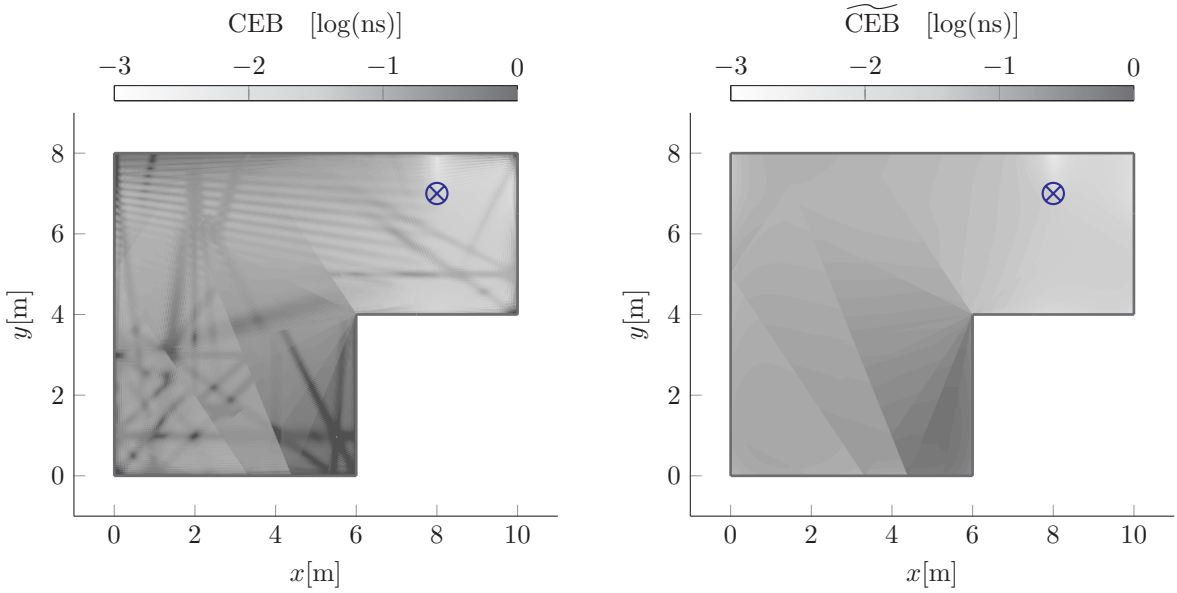

(a) CRLB for the clock offset estimation, considering PO

(b) CRLB for the clock offset estimation, neglecting PO

Figure 3.8: *CEB across the floor plan. It is especially interesting to see the connection between the CEB and the difference in the PEB in Fig. 3.7.*

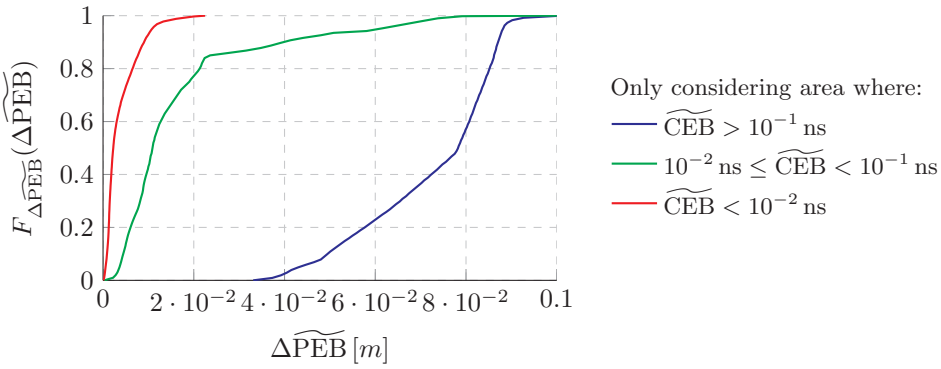

Figure 3.9: *Influence of the CEB on the PEB. CDFs for different areas of the floor plan are shown, which indicate the connection between importance of a low clock synchronization error.*

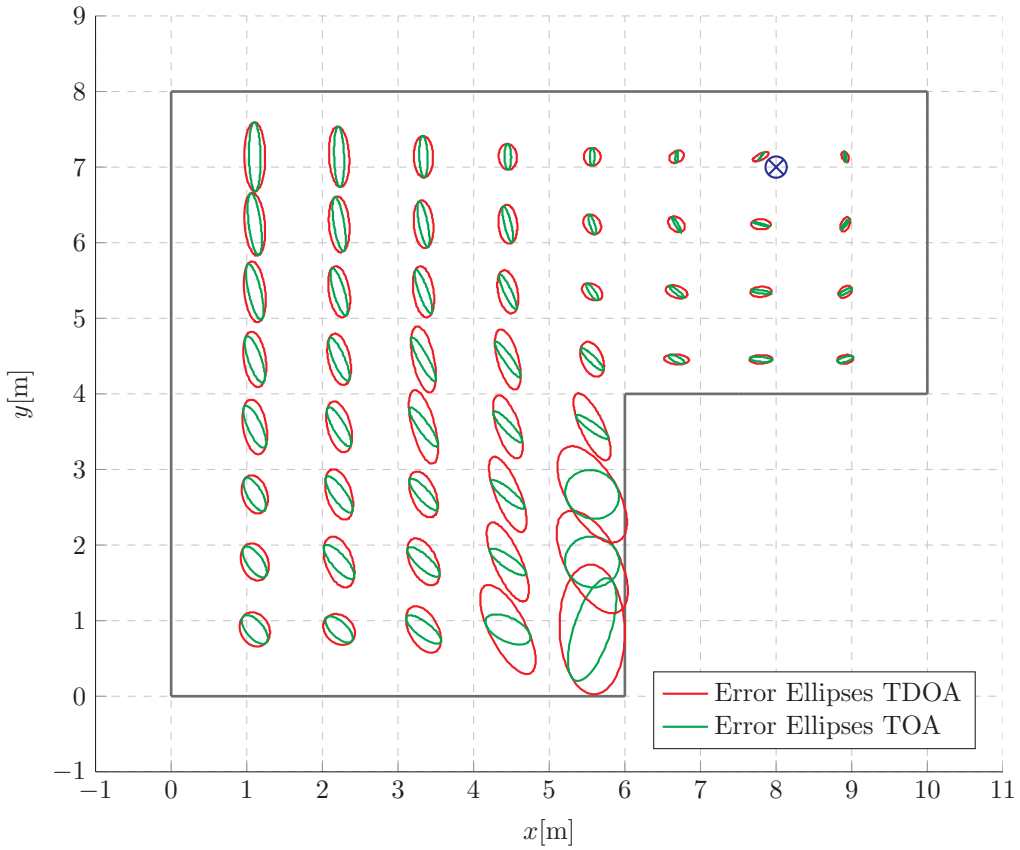

Figure 3.10: *Comparisons of the error ellipses for TDOA and TOA. The result is shown for the case when neglecting PO. Comparing the TDOA and TOA case shows a spreading and a rotation of the error ellipses. Clearly, the error ellipses for TOA are a lower bound for the error ellipses in the TDOA case.*

3.6.3 Limitations under Real-Life Conditions

The assumptions made in the previous section do not always meet the conditions in a real scenario. Sometimes the building materials provide only poor signal reflectivity, additional scatterers make the estimation of MPCs difficult and moving objects can block signal paths. All these factors deteriorate the localization performance. Although this is not the main focus of this work, we will briefly analyze the influence here.

We start by analyzing a scenario where an object blocks the LOS path, which means that we have to deal with an NLOS situation. In a realistic scenario it is rather unlikely that only the LOS is blocked, in most cases this would also affect the visibility of other VAs. But for simplicity we restrict the analysis solely to an NLOS situation. In the TOA scenario in [6], it was obvious, that the LOS component was a dominating contributor to a low PEB. The importance of this MPC is reduced in the TDOA case, but nevertheless it also provides valuable localization information. In Fig. 3.11 (a),(b) the influence on the PEB for TDOA is shown. When comparing it with Fig. 3.4 (a),(b) no big difference can be observed. The slight increase of the PEB is better noticeable when comparing the CDFs in Fig. 3.11 (c),(d). This illustration also shows that the TOA system is more affected by the NLOS situation than the TDOA system, but both seem to be quite robust to NLOS situations. Furthermore, the result for TDOA with $T_p = 0.5\,\text{ns}$ shows that reducing the pulse duration is clearly a way to reduce the performance loss and achieve even much better performance than the TOA system.

The situation changes when assuming high attenuation of signal reflections. We refer to this scenario as the low-reflectivity case. It is emulated by attenuating first-order reflections by 6 dB, and neglecting second-order reflections completely. Now the impact shown in Fig. 3.12 (a),(b) is much more drastic. In this case we encounter large areas where localization is not possible, e.g. in the lower right hand corner. Also the impact of PO is greatly increased, although the areas affected by PO are reduced due to less involved VAs. The CDFs in (c),(d) again show the drastic consequences of such a situation. In contrast to the NLOS scenario one can also notice, that now the TDOA system is more sensitive to the reduced set of VAs when comparing it with the TOA system. It is also important to mention, that even a reduction of the pulse duration to $T_p = 0.5\,\text{ns}$ is only partially a suitable measure to overcome the deterioration. Using this shorter pulse leads to a comparable performance as for TOA with twice the pulse duration.

The obtained results indicate that reducing the pulse duration helps to overcome some shortcomings of the TDOA system. However, depending on the requirements, this might be a quite expensive measure. As an alternative we will now examine the case when extending the topology by additional anchors.

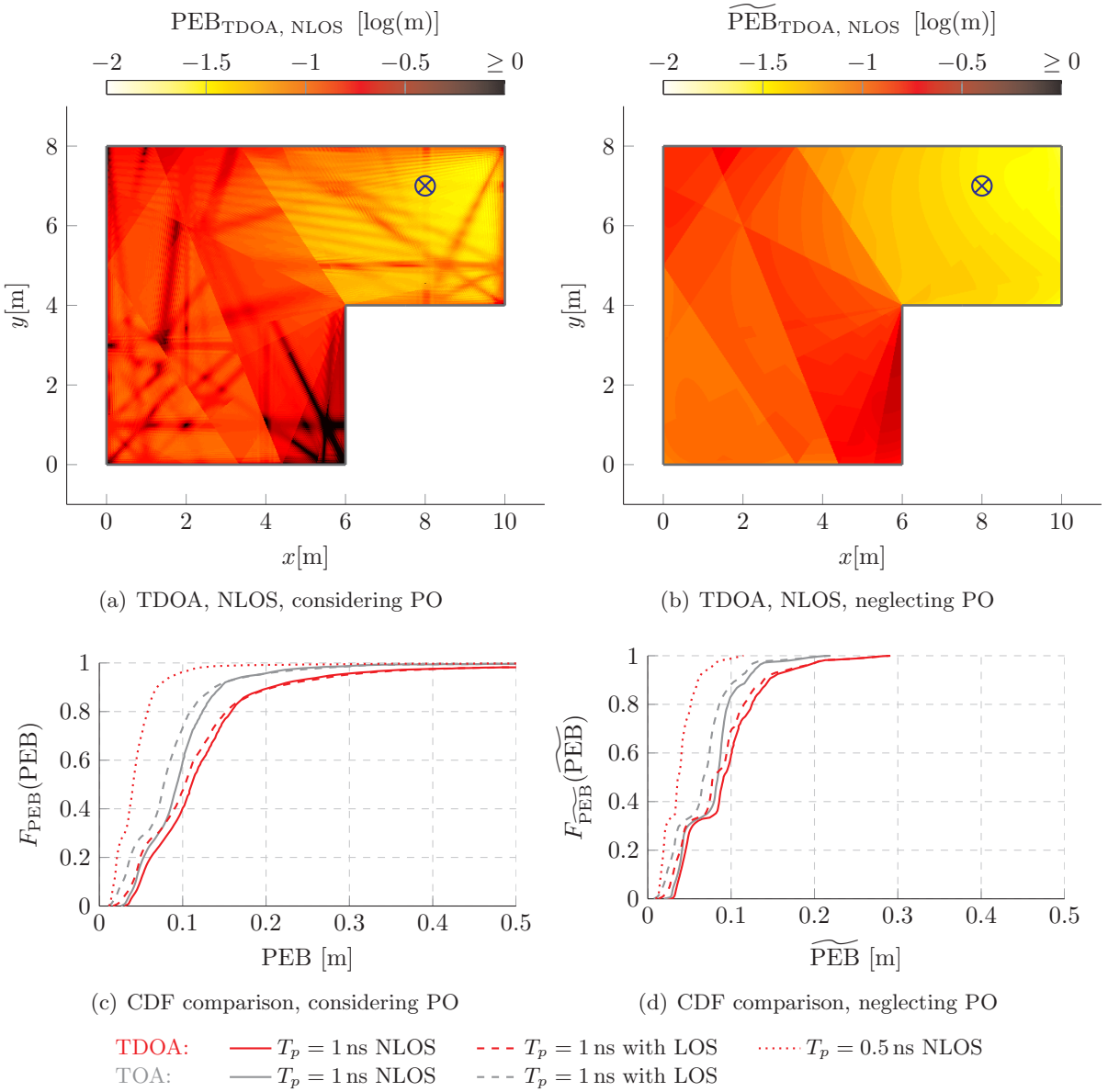

Figure 3.11: *Localization performance in a NLOS scenario. The PEB across the floor plan shows a similar result as in 3.4 (a,b) with an overall increase of the PEB.*

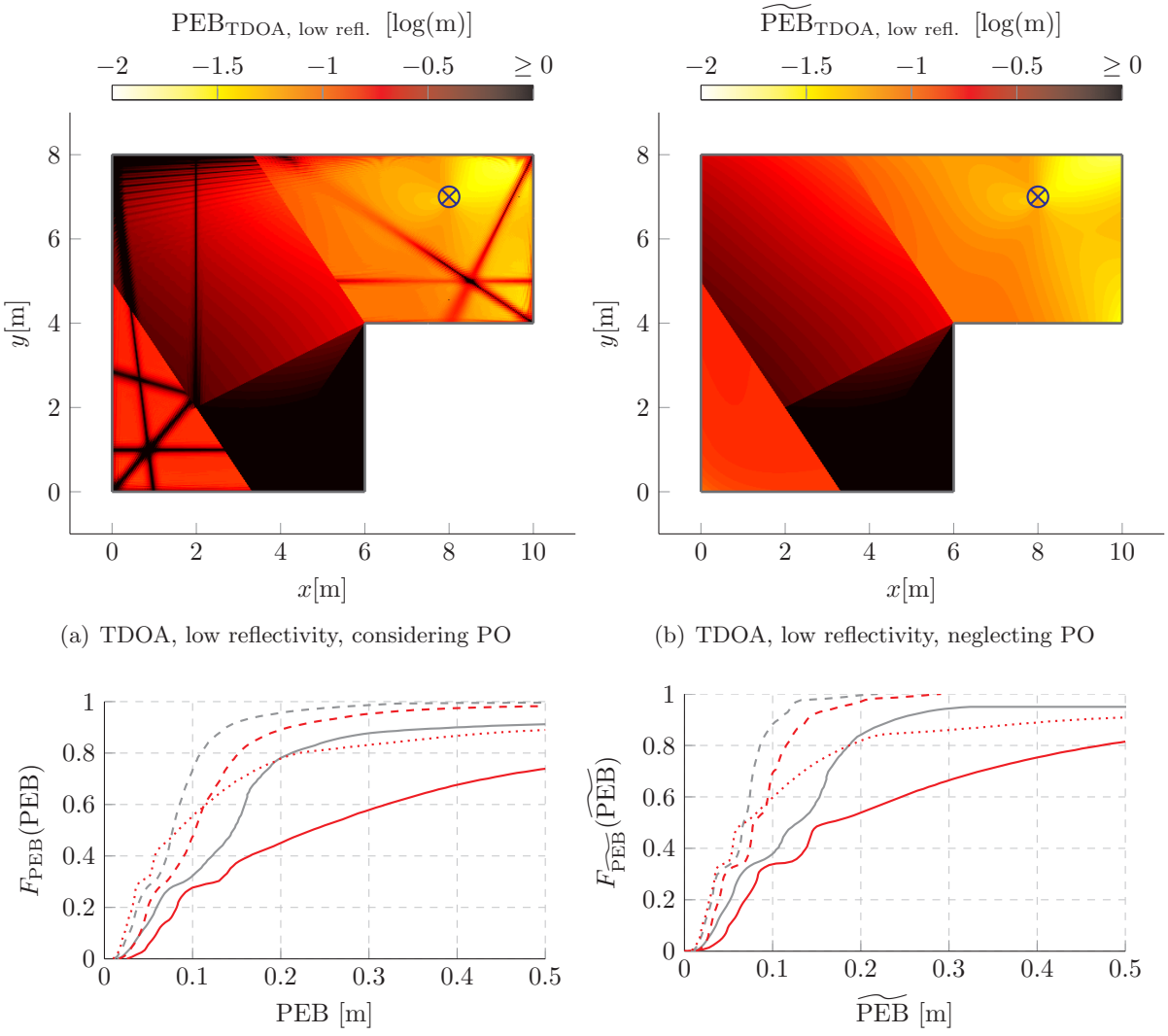

(a) TDOA, low reflectivity, considering PO

(b) TDOA, low reflectivity, neglecting PO

(c) CDF comparison, considering PO

(d) CDF comparison, neglecting PO

Figure 3.12: *PEB for a scenario with low wall reflectivity. Low reflectivity is emulated by considering only VAs up to order one, and an increased attenuation of 6 dB for a reflection. Obviously such a scenario is a major problem when considering TDOA localization. In some areas with low VA visibility the position estimation even becomes impossible.*

3.6.4 Remedy by using Multiple Transmitting Anchors

The theoretical analysis in Section 3.5 showed that the use of multiple anchors can significantly improve the performance of TDOA. Therefore, we investigate the suitability of a multi-anchor system to overcome the disadvantages when using a TDOA system instead of a TOA system.

We first look at the PEB across the floor plan when using two asynchronous anchors ($J = 2$). This is shown in Fig. 3.13 (a),(b). Comparing it with Fig. 3.4, where only one anchor was used, one can see that the PEB is distributed much more smoothly, and that the impact of PO is significantly reduced. The results for two synchronous anchors are not shown, since they are very similar to the presented results. However, the difference of the results is illustrated using the CDFs in Fig. 3.13 (c),(d). In terms of the CDFs, two synchronized anchors perform slightly better than two asynchronous anchors. This is basically what we expected from the theoretical comparison in Section 3.5.3. Another fact becomes obvious: The TDOA systems using two anchors are in any case superior to the single-anchor systems, no matter whether using TOA or TDOA.

Now it is interesting, how the two-anchor system performs under the real-life conditions defined in Section 3.6.3. Since we have already shown that there is only a slight difference between two synchronized / asynchronous anchors, we will restrict the following analysis to the case with two asynchronous anchors.

When analyzing the impact of an NLOS situation (Fig. 3.14) or a low-reflectivity scenario (Fig. 3.15), it is remarkable that the performance degradation with respect to the single-anchor case is drastically reduced. In both cases the PEB is much more smoothly distributed. Especially the NLOS situation in Fig. 3.14 does only slightly affect the localization problem. Only when looking at the PEB in the low-reflectivity scenario (Fig. 3.15) some problematic regions can be seen, while the overall performance is still very good. The CDFs in Fig. 3.14 (c),(d) do not provide much additional information, except that they show that a single-anchor TDOA system needs twice the bandwidth to achieve similar performance. On the other hand, the CDFs for the low-reflectivity scenario (Fig. 3.15 (c),(d)) highlight an important result: In such a scenario a multi-anchor system is clearly superior to a single-anchor system, even if the single anchor system operates with much more bandwidth. Note that by now increasing the bandwidth of the transmit pulse in a single anchor TDOA system has always been a possible remedy against performance degradation. This also might be true in the present case, but the demand on the signal bandwidth would be disproportionately high.

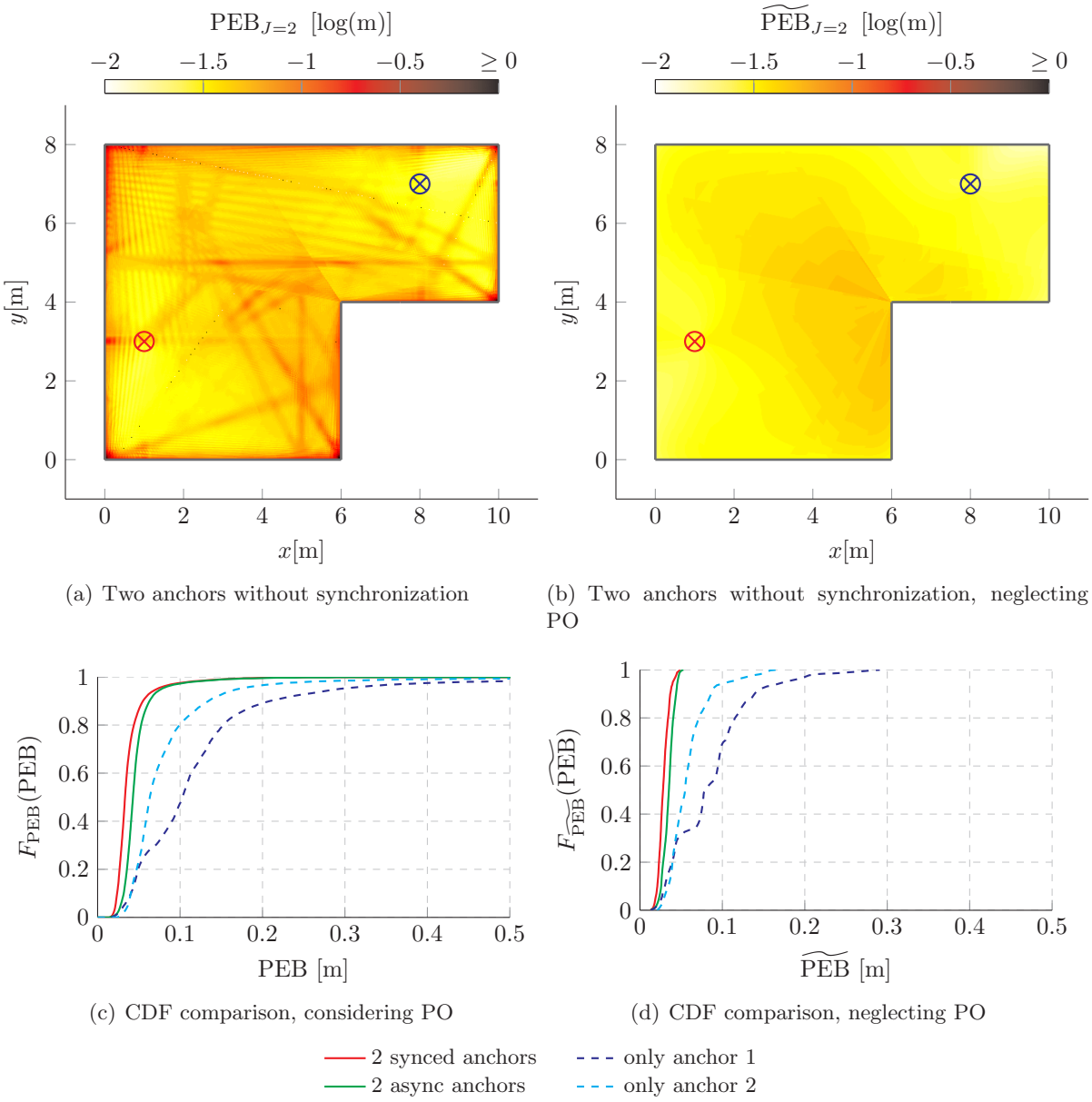

(a) Two anchors without synchronization

(b) Two anchors without synchronization, neglecting PO

(c) CDF comparison, considering PO

(d) CDF comparison, neglecting PO

Figure 3.13: *Performance when considering a TDOA system with two anchors. (a,b) show the smoothly distributed PEB for the case with asynchronous anchors. The result for synchronized anchors is not illustrated, since it differs only slightly. The CDFs comparison (c,d) clearly shows the performance gain compared to the single-anchor systems. It also shows the minor differences between multiple anchors with / without synchronization.*

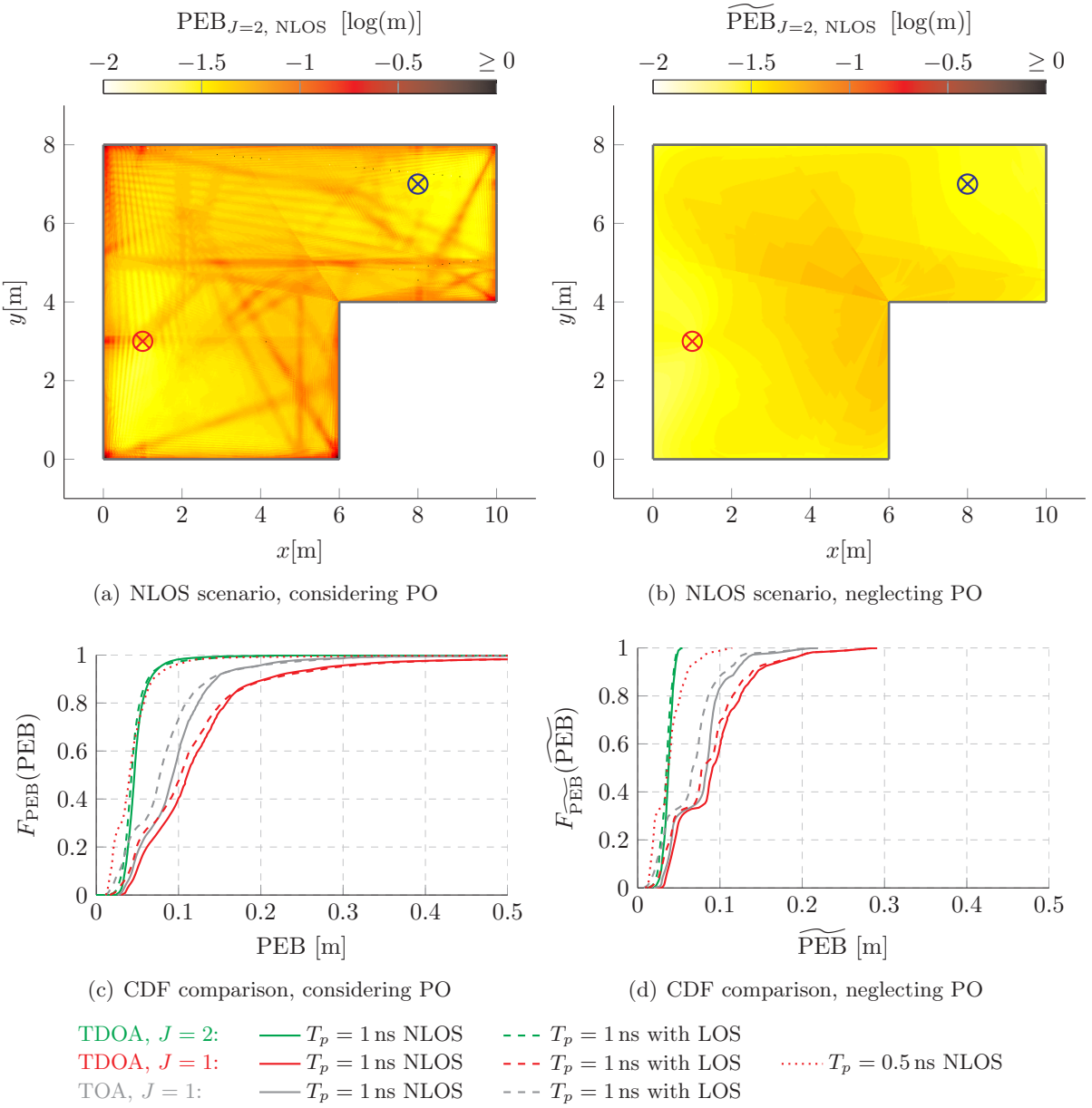

(a) NLOS scenario, considering PO

(b) NLOS scenario, neglecting PO

(c) CDF comparison, considering PO

(d) CDF comparison, neglecting PO

Figure 3.14: *Performance of the two-anchor system in a NLOS situation. Only the case for two anchors without synchronization is shown. Comparing the structure of the PEB across the room (a,b) with Fig. 3.13 shows some minor degradations, but the overall influence of a NLOS scenario is almost negligible. This is also visible when looking at the CDFs (c,d). Additionally, these indicate that a single-anchor TDOA system needs twice the bandwidth in order to achieve the same performance.*

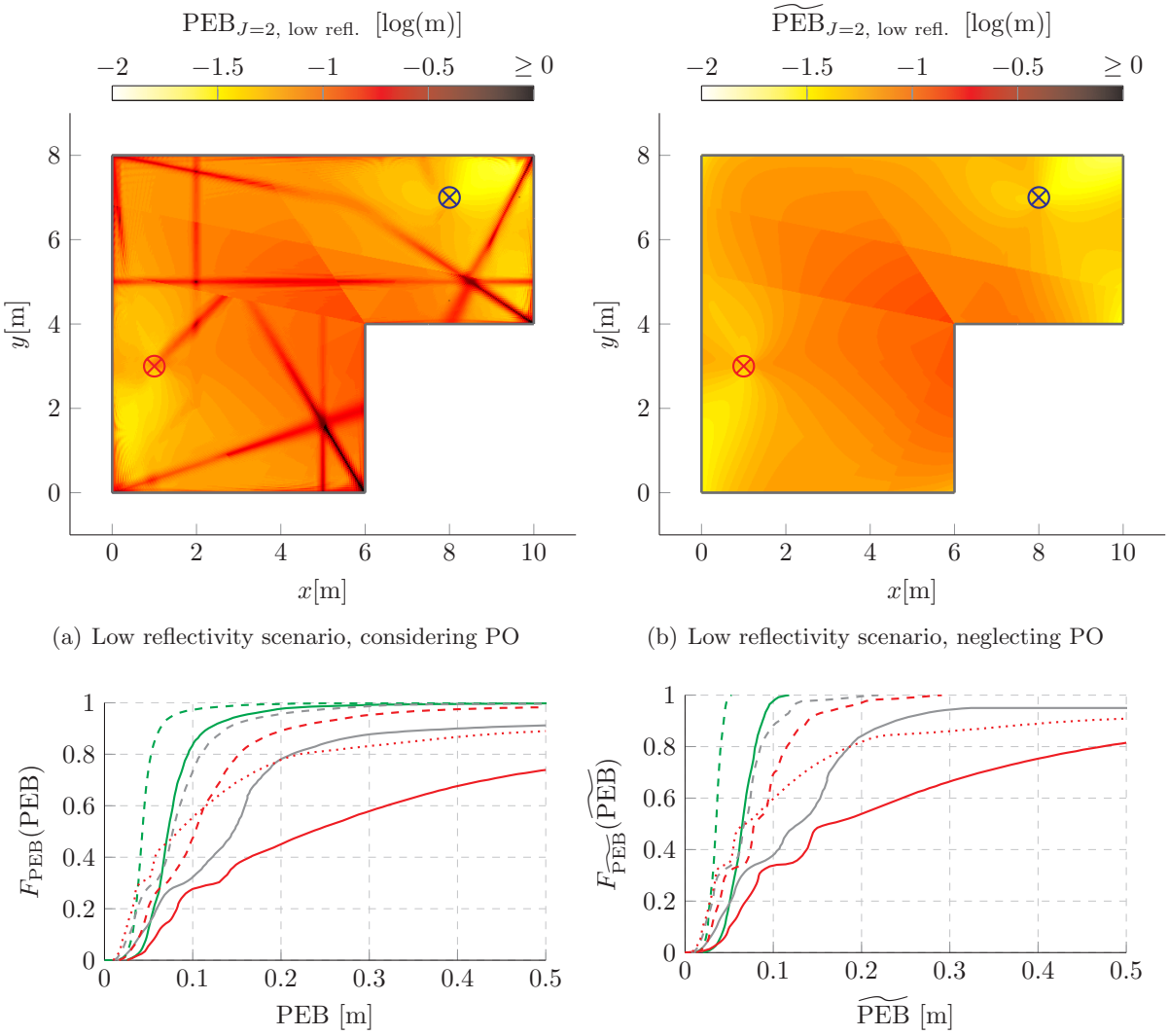

(a) Low reflectivity scenario, considering PO

(b) Low reflectivity scenario, neglecting PO

(c) CDF comparison, considering PO

(d) CDF comparison, neglecting PO

Figure 3.15: *Performance of the two-anchor system for a scenario with low wall reflectivity. Only the case for two anchors without synchronization is shown. When comparing the performance result with the single-anchor case in Fig. 3.12, one can clearly see the huge performance improvement. The CDFs (c,d) also indicate that in this case the TDOA system with two anchors is clearly superior to a system with only one anchor, even when halving its pulse duration.*

4 Maximum Likelihood Estimation

4.1 Introduction

So far we have derived the CRLB for the position estimates, which gave us helpful insight in the estimation problem. However, the CRLB yields the theoretical limits of position estimation, and is only valid in the close vicinity of the examined position. As already mentioned in Section 2.6 it is obvious, that e.g. room symmetries can lead to situations, where accurate position estimation is not possible. Such, and also other cases are not covered when examining the CRLB. Therefore, we will complete our analysis by studying the impact of the clock offset on a practical position estimator, namely an MLE.

The choice of the MLE was made because of its advantageous properties, which make the analysis meaningful while at the same time keeping the effort low. First of all, we can compare the performance of the MLE with the CRLB. It is known, that the MLE is asymptotically efficient [26], which means that it attains the CRLB if the set of data is large enough. Furthermore, as its name suggests, the MLE obtains estimates of the agent position by maximizing the LHF of its underlying parameters. This involves evaluation of the LHF, a function which yields the basis for other practical estimators such as the maximum a posteriori (MAP) estimator. The maximization of the LHF can be performed numerically, and a closed-form solution is not required. It is sufficient to perform a simple grid search, where we only have to compute the result of the LHF on a grid across the room, and we do not have to consider particular algorithms for the maximization such as e.g. gradient search algorithms.

On the downside, the MLE does not belong to the class of minimum variance unbiased estimators (MVUEs) [26], although for some cases it yields equal results. But given its approximate efficiency it is sufficient for our analysis. Furthermore, the implementation using a grid search is not very well suitable for practical position estimation. The computational expenses increase with the required spatial resolution and the number of parameters. A more practical approach for the implementation of an MLE would be to e.g. use a particle filter, as it is done in [9]. This helps to reduce the computational effort drastically and makes even real-time localization feasible. Finally, it is important to mention that the results of this chapter are not conclusive.

The evaluation of the LHF helps to gain insight, but of course relying on computer simulations is not sufficient to fully asses estimator performance.

We will approach the problem similarly as in Chapter 3, i.e. we will first look at the problem when using only a single anchor, and later extend it for the case where multiple anchors are used. In order to assess the reliability and performance of the MLE, we will analyze the shape of the LHF in detail and compare the MLE performance with the CRLB. The final evaluation of measurement data should be seen as a feasibility study to emphasize the proper functionality.

4.2 Maximum Likelihood Estimation with a Single Anchor

The aim is to perform ML estimation of the agent position considering the problem defined in Chapter 2. For simplicity we start with the case where only one anchor is used. In general the estimation procedure can mathematically be formulated as

$$\hat{\boldsymbol{\theta}} = \arg\max_{\boldsymbol{\theta}} f(\mathbf{r};\boldsymbol{\theta}), \tag{4.1}$$

i.e. the estimated parameter vector $\hat{\boldsymbol{\theta}}$, which also contains estimates $\hat{\mathbf{p}}$ of the agent position $\mathbf{p}$, is obtained by varying the parameters $\boldsymbol{\theta}$ (3.6), searching for the set of parameters which maximize the LHF $f(\mathbf{r};\boldsymbol{\theta})$ for $\boldsymbol{\theta}$, given the observation $\mathbf{r}$.

In a practical system it is not feasible to perform the ML estimation based on the continuous time waveform $r(t)$ as it is done in Chapter 3. Instead we have to consider a sampled data model, which describes a filtered and sampled version $\mathbf{r}$ of the received signal. Therefore, we cannot directly use the LHF defined in (3.11), but have to consider an adapted LHF.

The above considerations clarify the further approach: In order to perform the ML estimation, we need to derive the LHF. This requires to first study the statistical properties of the filtered and sampled received signal, which is done in the following section.

4.2.1 Sampling the Received Signal

In order to fulfill the Nyquist criterion, we need to process the received signal $r(t)$ with an anti-aliasing filter $h_{lp}(\tau)$. The band-limited signal $r_{lp}(t)$ is then given by

$$r_{lp}(t) = (r * h_{lp})(t) = \int_{-\infty}^{\infty} r(\tau) h_{lp}(t-\tau) d\tau.$$

We can think of different filters for that purpose, e.g. an ideal low-pass filter, or alternatively a matched filter. The former has its cutoff frequency f_c exactly at half the sampling rate $f_c = f_s/2$, while the latter matches the shape of the transmit pulse so that the condition

$$h_{lp}(t) = s(T_p - t), \qquad 0 \le t \le T_p$$

is fulfilled. The filtered waveform is then sampled with the sampling frequency $f_s = 1/T_s$, resulting in the discrete-time signal $r[n]$

$$r[n] = r_{lp}(nT_s), \qquad n = 0 \dots N-1,$$

or in the signal vector $\mathbf{r} \in \mathbb{C}^N$ when using vector notation,

$$\mathbf{r} = \begin{bmatrix} r[0] & r[1] & \cdots & r[N-1] \end{bmatrix}^T .$$

Since we assume a linear time-invariant (LTI) system, we can examine the filtering and sampling process also on the components of the received signal. For the following part we assume that the Nyquist criterion is satisfied, i.e. the sampling frequency f_s exceeds twice the maximum frequency of the transmit signal.

We start by looking at the deterministic signal components $\tilde{s}(t)$. These consist of a sum of K weighted baseband pulses. Clearly an ideal low-pass filter has no influence on the deterministic components. When using a matched filter on the other hand, the pulse shape is changed. Thus we can write the sampled version ot the deterministic components as

$$\tilde{s}[n] = \tilde{s}_{lp}(nT_s) = \sum_{k=1}^{K} \alpha_k s_{lp}(nT_s - \tau_k),$$

where $s_{lp}(t) = (s * h_{lp})(t)$ denotes the pulse shapes of the filtered received pulses. Using vector notation, we define a vector $\tilde{\mathbf{s}} \in \mathbb{R}^N$ containing the samples of the deterministic part,

$$\tilde{\mathbf{s}} = \begin{bmatrix} \tilde{s}[0] & \tilde{s}[1] & \cdots & \tilde{s}[N-1] \end{bmatrix}^T .$$

Note that this vector can easily be expressed as a multiplication of a signal-matrix $\mathbf{S}_\tau \in \mathbb{R}^{N \times K}$ with a vector $\boldsymbol{\alpha} \in \mathbb{C}^K$ containing the path-amplitudes. It is then defined by

$$\tilde{\mathbf{s}} = \mathbf{S}_\tau \boldsymbol{\alpha} \ , \tag{4.2}$$

with

$$\boldsymbol{\alpha} = \begin{bmatrix} \alpha_0 & \alpha_1 & \cdots & \alpha_K \end{bmatrix}^T , \quad \alpha_k \in \mathbb{C},$$

and the signal matrix consisting of K pulses shifted in time,

$$\mathbf{S}_{\boldsymbol{\tau}} = \begin{bmatrix} \mathbf{s}_{\tau_1} & \mathbf{s}_{\tau_2} & \cdots & \mathbf{s}_{\tau_K} \end{bmatrix},$$

where

$$\mathbf{s}_{\tau_k} = \begin{bmatrix} s_{lp}(0 \cdot T_s - \tau_k) & s_{lp}(1 \cdot T_s - \tau_k) & \cdots & s_{lp}((N-1) \cdot T_s - \tau_k) \end{bmatrix}^T .$$

When looking at the diffuse MPCs we have a similar situation as for the deterministic components. We can formulate the sampled diffuse multipath signal $n_c[n]$ as a convolution of the low-pass filtered transmit pulse $s_{lp}(t)$ and the CIR of the diffuse MPC $\nu(\tau)$ similar as in (2.4),

$$\begin{aligned} n_c[n] = n_{c,lp}(nT_s) = (n_c * h_{lp})(nT_s) = (s * \nu * h_{lp})(nT_s) = (s_{lp} * \nu)(nT_s) \\ = \int_{-\infty}^{\infty} s_{lp}(\lambda)\nu(nT_s - \xi - \lambda)\mathrm{d}\lambda. \end{aligned} \tag{4.3}$$

Using matrix notation again, we can express the colored noise component as

$$\mathbf{n}_c = \begin{bmatrix} n_c[0] & n_c[1] & \cdots & n_c[N-1] \end{bmatrix}^T , \quad \mathbf{n}_c \in \mathbb{C}^N. \tag{4.4}$$

The samples of the observation noise are given by

$$w[n] = w_{lp}(nT_s)$$

or

$$\mathbf{w} = \begin{bmatrix} w[0] & w[1] & \cdots & w[N-1] \end{bmatrix}^T, \quad \mathbf{w} \in \mathbb{C}^N,$$

where $w_{lp} = (w * h_{lp})(t)$ is again the filtered version of the observation noise $w(t)$.

With this we can formulate the signal vector $\mathbf{r}$, which forms the basis for the present estimation problem, as

$$\begin{aligned} \mathbf{r} &= \tilde{\mathbf{s}} + \mathbf{n}_c + \mathbf{w} \\ &= \mathbf{S}_{\boldsymbol{\tau}}\boldsymbol{\alpha} + \mathbf{n}_c + \mathbf{w}. \end{aligned} \tag{4.5}$$

4.2.2 Statistical Properties of the Signal Vector

We will now derive the statistical properties of the signal vector $\mathbf{r}$, which is necessary to formulate the LHF. Helpful is the following considerations: The received signal $r(t)$ (2.5) is modeled as a Gaussian RP. Applying a LTI filter operation does not change the nature of the RP, thus sampling yields a Gaussian random vector. Therefore, we can fully characterize the sampled signal $\mathbf{r}$ by computing its mean vector $\mathrm{E}\{\mathbf{r}\}$ and its covariance matrix $\mathbf{C}$.

The mean vector $\mathrm{E}\{\mathbf{r}\}$ is given by the sum of all contributions, i.e.

$$\mathrm{E}\{\mathbf{r}\} = \mathrm{E}\{\mathbf{S}_{\boldsymbol{\tau}}\boldsymbol{\alpha}\} + \mathrm{E}\{\mathbf{n}_c\} + \mathrm{E}\{\mathbf{w}\}.$$

The observation noise $w(t)$ as well as the part of the CIR for the diffuse multipath (modeled by $\nu(\tau)$) are zero-mean Gaussian RPs. A linear functional of a zero-mean Gaussian RP yields again a zero-mean Gaussian RP, resulting in $\mathrm{E}\{\mathbf{n}_c\} = \mathrm{E}\{\mathbf{w}\} = \mathbf{0}$. Therefore, the mean vector is exclusively determined by the deterministic part of the signal, i.e.

$$\mathrm{E}\{\mathbf{r}\} = \mathbf{S}_{\boldsymbol{\tau}}\boldsymbol{\alpha}. \tag{4.6}$$

The covariance matrix for a complex valued random vector (RV) $\mathbf{r}$ is defined as

$$\mathbf{C} = \mathrm{E}\Big\{ (\mathbf{r} - \mathrm{E}\{\mathbf{r}\}) (\mathbf{r} - \mathrm{E}\{\mathbf{r}\})^H \Big\}.$$

Inserting (4.6) and (4.5) in the equation above results in

$$\mathbf{C} = \mathrm{E}\big\{ \mathbf{n}_c \mathbf{n}_c^H \big\} + \mathrm{E}\big\{ \mathbf{w}\mathbf{w}^H \big\} + 2\mathrm{E}\big\{ \mathbf{n}_c \mathbf{w}^H \big\},$$

where the first two terms are the covariance matrices of the diffuse multipath and observation noise, respectively. The last term $2\mathrm{E}\big\{ \mathbf{n}_c \mathbf{w}^H \big\} = \mathbf{0}$ is zero, since the observation noise is assumed to be statistically independent from the diffuse components. Therefore, the covariance matrix $\mathbf{C}$ for $\mathbf{r}$ is given by the sum of the covariance matrices $\mathbf{C}_{\mathbf{n}_c}$ and $\mathbf{C}_{\mathbf{w}}$ for the diffuse multipath and observation noise,

$$\mathbf{C} = \mathbf{C}_{\mathbf{n}_c} + \mathbf{C}_{\mathbf{w}}.$$

We will first examine the covariance matrix of the diffuse multipath, which is due to its zero mean property given by

$$\mathbf{C}_{\mathbf{n}_c} = \mathrm{E}\{\mathbf{n}_c \mathbf{n}_c^H\}.$$

To simplify the result, we will look separately at the elements of $\mathbf{C}_{\mathbf{n}_c}$. With (4.3) and (4.4) follows that the element in its n-th row and u-th column is given by

$$[\mathbf{C}_{\mathbf{n}_c}]_{n,u} = \mathrm{E}\left\{ \int_{-\infty}^{\infty} s_{lp}(nT_s - \xi - \lambda)\nu(\lambda)\mathrm{d}\lambda \cdot \int_{-\infty}^{\infty} s_{lp}(uT_s - \xi - \eta)\nu^*(\eta)\mathrm{d}\eta \right\}.$$

With $\lambda' = \lambda + \xi$ and $\eta' = \eta + \xi$ follows

$$\begin{aligned}[\mathbf{C}_{\mathbf{n}_c}]_{n,u} &= \int_{-\infty}^{\infty}\int_{-\infty}^{\infty} s_{lp}(nT_s - \lambda')\mathrm{E}\{\nu(\lambda' - \xi)\nu^*(\eta' - \xi)\}\, s_{lp}(uT_s - \eta')\mathrm{d}\eta'\mathrm{d}\lambda' \\ &= \int_{-\infty}^{\infty}\int_{-\infty}^{\infty} s_{lp}(nT_s - \lambda')S_\nu(\lambda' - \xi)\delta(\lambda' - \eta')s_{lp}(uT_s - \eta')\mathrm{d}\eta'\mathrm{d}\lambda'.\end{aligned}$$

The inner integral can be eliminated using the sifting property of the Dirac delta function and leads to

$$[\mathbf{C}_{\mathbf{n}_c}]_{n,u} = \int_{-\infty}^{\infty} s_{lp}(nT_s - \lambda')S_\nu(\lambda' - \xi)s_{lp}(uT_s - \lambda')\mathrm{d}\lambda'.$$

This integral can be approximated by

$$\begin{aligned}[\mathbf{C}_{\mathbf{n}_c}]_{n,u} &\approx T_s \cdot \sum_{i=0}^{N-1} s_{lp}(nT_s - iT_s)S_\nu(iT_s - \xi)s_{lp}(uT_s - iT_s) \\ &= T_s \cdot \sum_{i=0}^{N-1} s_{lp}[n-i]S_\nu(iT_s - \xi)s_{lp}[u-i],\end{aligned}$$

which helps to formulate the covariance matrix directly in a compact form,

$$\mathbf{C}_{\mathbf{n}_c} = T_s\ \mathbf{\Phi}\ \mathbf{S}_\nu\ \mathbf{\Phi}^T. \tag{4.7}$$

Here $\mathbf{S}_\nu$ is a $N \times N$ diagonal matrix with the sampled PDP shifted by ξ on the diagonal, i.e.

$$\mathbf{S}_\nu = \mathrm{diag}\left(S_\nu(0 \cdot T_s - \xi), \ldots, S_\nu((N-1) \cdot T_s - \xi)\right),$$

and $\mathbf{\Phi}$ is a matrix consisting of N pulses shifted by multiple integers of the sampling period T_s,

$$\mathbf{\Phi} = \begin{bmatrix}\mathbf{s}_0 & \mathbf{s}_1 & \cdots & \mathbf{s}_{N-1}\end{bmatrix}, \quad \mathbf{s}_i = \left[s_{lp}\left((0-i)T_s\right), s_{lp}\left((1-i)T_s\right), \ldots, s_{lp}\left((N-i)T_s\right)\right]^T.$$

Note that for the special case when the pulses $s_{lp}(t - iT_s),\ i = 0, \ldots, N-1$ are orthogonal, and Nyquist sampling is used (i.e $T_s = T_p$), then the signal vectors in $\mathbf{\Phi}$ are linearly independent, meaning that $\mathbf{\Phi}$ is an orthogonal matrix. Therefore (4.7) becomes a diagonal matrix, meaning that the samples of the diffuse multipath are uncorrelated. This is e.g. the case when using an RRC transmit pulse in conjunction with a matched filter, and sampling with $T_s = T_p$.

The last step is to derive the covariance matrix of the observation noise. In contrast to the continuous time model used in Chapter 3, the observation noise is now band-limited by the

low-pass filter. The elements of its covariance matrix are given by samples of the ACF $\Phi_{w_{lp}}$ of the low-pass filtered observation noise w_{lp},

$$[\mathbf{C_w}]_{n,u} = \mathrm{E}\{w[n]w^*[u]\} = \mathrm{E}\big\{w_{lp}(nT_s)w^*_{lp}(uT_s)\big\} = \Phi_{w_{lp}}((n-u)T_s).$$

To derive the ACF of the filtered noise we utilize the Wiener Khinchin theorem, which states that the PSD of a wide sense stationary random process is connected with its ACF through the Fourier transformation,

$$S_{w_{lp}}(j\omega) = \mathcal{F}\big\{\Phi_{w_{lp}}(\tau)\big\}.$$

The PSD of the observation noise is on the other hand affected by the low-pass filter by multiplication with the squared magnitude of the low-pass frequency response,

$$S_{w_{lp}}(j\omega) = S_w(j\omega) \cdot |H_{lp}(j\omega)|^2.$$

Now the inverse Fourier transform is used to arrive at the ACF of the filtered observation noise,

$$\Phi_{w_{lp}}(\tau) = \mathcal{F}^{-1}\big\{S_{w_{lp}}(j\omega)\big\}.$$

Since the PSD of the continuous time process is given as $S_w(j\omega) = N_0$, the impulse response of the low-pass filter determines the shape of the ACF. Note that e.g. in the case when using an ideal anti-aliasing filter (i.e. a sinc filter) with cutoff frequency $f_c = f_s/2$, then the ACF is given by

$$\Phi_{w_{lp}}(\tau) = N_0 2 f_c \,\mathrm{sinc}(2f_c\tau) = N_0 f_s \,\mathrm{sinc}(f_s\tau),$$

where $\mathrm{sinc}(t)$ denotes the normalized sinc function. Sampling the ACF with $T_s = 1/f_s$ leads to uncorrelated samples with variance $\mathrm{var}\{w[n]\} = N_0 f_s$, i.e.

$$\mathbf{C}_w = N_0 f_s \mathbf{I}. \tag{4.8}$$

Clearly, increasing the sampling frequency also increases the noise bandwidth and thus also the variance of the samples. On the other hand, when using oversampling in conjunction with a filter other than the ideal anti-aliasing filter, then the samples are not uncorrelated anymore, i.e. $\mathbf{C}_w$ is not diagonal anymore. We will see in Section 4.4 when performing the numerical evaluation, that it is important to consider this case, since oversampling but at the same time limiting the noise bandwidth is necessary to obtain meaningful results from the MLE.

So far we have completely characterized the RV $\mathbf{r}$. Its mean value is given by (4.6), while its covariance matrix is given by the sum of (4.7) and (4.8), yielding

$$\mathbf{C} = \mathbf{C}_c + \mathbf{C}_w = N_0 f_s \mathbf{I} + T_s \; \mathbf{\Phi} \; \mathbf{S}_\nu \; \mathbf{\Phi}^T. \tag{4.9}$$

4.2.3 The Likelihood Function

In the previous section we saw, that the received signal vector $\mathbf{r}$ is given as a sample of a multivariate complex Gaussian distribution,

$$\mathbf{r} \sim \mathcal{CN}(\mathbf{S}_\tau \boldsymbol{\alpha},\ \mathbf{C}).$$

For such a random vector the LHF is well known,

$$f(\mathbf{r};\boldsymbol{\theta}) = \frac{1}{\pi^N \det(\mathbf{C})} \exp\left[-(\mathbf{r}-\mathbf{S}_\tau\boldsymbol{\alpha})^H \mathbf{C}^{-1}(\mathbf{r}-\mathbf{S}_\tau\boldsymbol{\alpha})\right]. \tag{4.10}$$

When considering the assumptions made in Section 3.4.2, the approximation of the LHF leads to a result very similar to (3.11). More precisely, when assuming orthogonal pulses and Nyquist sampling, then $\boldsymbol{\Phi}$ in (4.9) is an orthogonal matrix. This in turn allows to find a simple expression for the inverse of the covariance matrix $\mathbf{C}$, which only utilizes matrix transposition and inversion of a diagonal matrix. We finally arrive at the log-LHF

$$\ln\ f(\mathbf{r};\boldsymbol{\theta}) \propto 2\mathrm{Re}\left\{\mathbf{r}^H\mathbf{S}_\tau\mathbf{W}\boldsymbol{\alpha}\right\} - \boldsymbol{\alpha}^H\mathbf{S}_\tau^T\mathbf{S}_\tau\mathbf{W}\boldsymbol{\alpha}, \tag{4.11}$$

where we also assume the covariance matrix $\mathbf{C}$ to be known, thus the term $\mathbf{r}^H\mathbf{C}^{-1}\mathbf{r}$ is constant and vanishes. The matrix $\mathbf{W}$ is given by

$$\mathbf{W} = \mathrm{diag}\left(w_1^2, w_2^2, \ldots, w_K^2\right), \quad w_k^2 = \frac{N_0}{N_0 + T_s S_\nu(\tau_k)}.$$

The similarity between (4.11) and (3.11) can clearly be seen. The detailed derivation can be found in Appendix B.1.

4.2.4 Maximum Likelihood Estimation

With the LHF (4.10) derived in the previous section we are basically in the position, where we can numerically evaluate the LHF. But for the sake of reducing the computational complexity, we will briefly look at how we can simplify the MLE although this is not the main focus.

First of all, it is sufficient to perform the maximization of the logarithm of the LHF. Since the natural logarithm is strictly monotonic, maximization of the LHF equals the problem of maximization of the logarithm of the LHF,

$$\begin{aligned}\hat{\boldsymbol{\theta}} &= \arg\max_{\boldsymbol{\theta}} f(\mathbf{r};\boldsymbol{\theta}) = \arg\max_{\boldsymbol{\theta}} \ln\ f(\mathbf{r};\boldsymbol{\theta}) \\ &= \arg\max_{\boldsymbol{\theta}} \left(-\ln\left(\det(\mathbf{C})\right) - (\mathbf{r}-\mathbf{S}_\tau\boldsymbol{\alpha})^H\mathbf{C}^{-1}(\mathbf{r}-\mathbf{S}_\tau\boldsymbol{\alpha})\right).\end{aligned}$$

If the covariance matrix can be estimated in an independent step and is assumed to be known for the position estimation, then the term $\ln\left(\det(\mathbf{C})\right)$ does not depend on $\boldsymbol{\theta}$, and does not need to be considered for the maximization.

We can further simplify the estimation procedure by separating the amplitude estimation. This can be seen, when writing the optimization problem as follows,

$$\hat{\boldsymbol{\theta}} = \arg\max_{\mathbf{p},\xi} \max_{\boldsymbol{\alpha}} \ln\ f(\mathbf{r};\boldsymbol{\theta}).$$

The inner maximization yields amplitude estimates for a given position $\mathbf{p}$ and synchronization offset ξ,

$$\hat{\boldsymbol{\alpha}}(\mathbf{p},\xi) = \arg\max_{\boldsymbol{\alpha}} \ln\ f(\mathbf{r};\mathbf{p},\xi,\boldsymbol{\alpha}).$$

Since the covariance matrix $\mathbf{C}$ depends on the position and clock offset, it is here constant and

can be neglected for the maximization in any case, reducing the LHF to

$$\begin{aligned}\ln\ f(\mathbf{r};\mathbf{p},\xi,\boldsymbol{\alpha}) &\propto -(\mathbf{r}-\mathbf{S}_\tau\boldsymbol{\alpha})^H\mathbf{C}^{-1}(\mathbf{r}-\mathbf{S}_\tau\boldsymbol{\alpha})\\ &\propto 2\mathrm{Re}\{\mathbf{r}^H\mathbf{C}^{-1}\mathbf{S}_\tau\boldsymbol{\alpha}\}-\boldsymbol{\alpha}^H\mathbf{S}_\tau^T\mathbf{C}^{-1}\mathbf{S}_\tau\boldsymbol{\alpha}.\end{aligned}$$

The advantage of the seperation of the problem becomes now obvious, since we can find an analytical expression for the ML estimates of the path amplitudes. For the maximization we set the gradient of the log-LHF equal to zero,

$$\nabla_{\boldsymbol{\alpha}}\ \ln\ f(\mathbf{r};\mathbf{p},\xi,\boldsymbol{\alpha}) \stackrel{!}{=} 0\ .$$

The maximum likelihood estimator is given by [26]

$$\hat{\boldsymbol{\alpha}} = (\mathbf{S}_\tau^T\mathbf{C}^{-1}\mathbf{S}_\tau)^{-1}\mathbf{S}_\tau^T\mathbf{C}^{-1}\mathbf{r}. \tag{4.12}$$

The similarity with the solution of a weighted least squares estimator [26] becomes immediately obvious. The weights are given by the inverse of the covariance matrix. Even more important is the fact that the MLE solution equals the solution of the linear model [26], provided that we examine the LHF at the true agent position $\mathbf{p}$ and true clock offset ξ. Indeed, the problem can be formulated using a linear model,

$$\mathbf{r} = \mathbf{S}_\tau\boldsymbol{\alpha}+\mathbf{n},\quad \mathbf{n}\sim\mathcal{CN}(\mathbf{0},\ \mathbf{C})\ .$$

Since the solution for the linear model yields the MVUE, we can conclude that the amplitude estimation (4.12) also yields the MVUE when examining it at the true agent position $\mathbf{p}$ and clock offset ξ.

Further, we can simplify the amplitude estimation provided that the assumptions about orthogonality of the pulses as well as Nyquist sampling are fulfilled. Based on the approximation of the LHF (4.11) the path amplitudes can then be estimated using

$$\hat{\boldsymbol{\alpha}} \approx (\mathbf{S}_\tau^T\mathbf{S}_\tau\mathbf{W})^{-1}\mathbf{W}^T\mathbf{S}_\tau^T\mathbf{r}.$$

This follows from the result obtained in Appendix B.1.

4.3 Maximum Likelihood Estimation with Multiple Anchors

When using multiple anchors, where J is the total number of anchors, we can again distinguish the two scenarios with either multiple synchronized or asynchronous anchors, as already discussed in Section 3.5. In any case we can formulate a joint LHF $\ln\ f_{\mathrm{M}}(\mathbf{r}_{\mathrm{M}};\boldsymbol{\psi}_{\mathrm{M}})$ for the stacked observations and parameter vectors as in (3.44) by adding the individual log-LHFs . However, for the actual maximization it is easier to only consider the individual LHFs $\ln\ f^{(j)}(\mathbf{r}^{(j)};\boldsymbol{\theta}^{(j)}) = \ln\ f^{(j)}(\mathbf{r}^{(j)};\mathbf{p},\xi^{(j)},\boldsymbol{\alpha}^{(j)})$ as follows.

4.3.1 Multiple Synchronized Anchors

For a setup with J synchronized anchors, all of these anchors share a common synchronization offset, i.e. $\xi^{(1)} = \cdots = \xi^{(J)} = \xi$. This needs to be considered when performing the maximization,

and leads to

$$\hat{\mathbf{p}} = \arg\max_{\mathbf{p},\xi} \sum_{j=1}^{J} \max_{\boldsymbol{\alpha}^{(j)}} \ln\ f^{(j)}(\mathbf{r}^{(j)}; \mathbf{p}, \xi, \boldsymbol{\alpha}^{(j)}).$$

4.3.2 Multiple Anchors without Synchronization

For multiple asynchronous anchors the estimation procedure does not vary a lot. Here, we have to find the position $\mathbf{p}$, which maximizes the overall LHF, while the LHFs corresponding to the individual anchors are parameterized by their own path-amplitudes $\boldsymbol{\alpha}^{(j)}$ and clock offset $\xi^{(j)}$. This leads to

$$\hat{\mathbf{p}} = \arg\max_{\mathbf{p}} \sum_{j=1}^{J} \max_{\boldsymbol{\alpha}^{(j)},\xi^{(j)}} \ln\ f^{(j)}(\mathbf{r}^{(j)}; \mathbf{p}, \xi^{(j)}, \boldsymbol{\alpha}^{(j)}).$$

4.4 Numerical Evaluation

Now we have completely defined the MLE, and are ready for its evaluation. The aim is, to validate the ability of localization in presence of a clock offset in principle, and furthermore verify the results of Chapter 3. During this evaluation we will gain additional insight about problems and limitations of the MLE, which were not covered by the analysis of the CRLB, and therefore perfectly complement the results from Chapter 3.

For a meaningful analysis, we again reduce the complexity of a real indoor environment by restricting to the example scenario defined in Section 2.8. However, we will also analyze the ML estimation using measurement data later on.

In order to assess the MLE performance, we will use two different approaches: We start by looking at the LHF across the floor plan, i.e. we view it as a function of the position[10] $\mathbf{p}'$,

$$\mathcal{L}(\mathbf{r}; \mathbf{p}') \propto \max_{\xi,\boldsymbol{\alpha}} \ln\ f(\mathbf{r}; \mathbf{p}', \xi, \boldsymbol{\alpha}). \tag{4.13}$$

This allows to make statements about the shape of the likelihood, and about locatability on a large-scale. On the other hand, we will also take a detailed look at the LHF in the vicinity of the agent position. We therefore compute multiple realizations of the received signal, and perform the ML estimation. The results are then used to compare them with the theoretical results of the CRLB. During the whole evaluation we have to keep in mind that the results of this section are not conclusive, since we use a statistical signal model for the received signal, but we only analyze a few realizations of $\mathbf{r}$.

4.4.1 Simulation Issues

For the numerical evaluation we assume the usage of a matched filter. With the transmit pulse being an RRC pulse, the pulses $s_{lp}(t)$ have a raised-cosine (RC) shape. All other signal parameters are specified in Section 2.8.

[10] We write $\mathbf{p}'$ for an arbitrary position on the floor plan, to distinguish from the agent position $\mathbf{p}$.

For the choice of an appropriate sampling frequency, we must address the following issue: In order to fulfill the sampling theorem, it would be sufficient to take the bandwidth extension of the RC pulse into account. However, using the minimum allowed sampling frequency leads to rather bad results when evaluation the LHF. The reason can already be found, when looking at the scalar product of two sampled pulses: $\sum_{n=0}^{N-1} s_{lp}(t_0 + nT_s - \tau_1) \cdot s_{lp}(t_0 + nT_s - \tau_2)$. If the pulse duration is in the order of the sampling period, i.e. $T_p \approx T_s$, then the outcome varies drastically, depending on the initial offset t_0 of the sampling process. Proceeding with an oversampling-factor of $M = 4$, i.e. the sampling frequency is given by $f_s = M/T_p$, avoids this problem.

The covariance matrix is assumed to be known. In reality, it is also necessary to estimate the covariance matrix. This estimation could be based on multiple measurements in the vicinity of the agent, or it could rely on a appropriate model for the diffuse multipath. In our case we assume perfect knowledge of the covariance matrix. Using this knowledge yields some sort of a gold standard estimator, since it neglects the uncertainty which arises when estimating this matrix. Furthermore, we neglect correlations of the diffuse multipath in order to reduce the computational complexity. This means that only the main diagonal of the covariance matrix $\mathbf{C}$ is considered. This does of course affect the estimation problem, since we hereby omit the whitening operation. However, it does not change the shape of the LHF very drastically, meaning that it is still sufficient for our purposes.

As already mentioned in the introduction, we stick to the computation of the ML estimates using a simple grid search. This means that $\mathcal{L}(\mathbf{r}; \mathbf{p}')$ (4.13) is computed for all positions on a grid, with a spacing of 2 cm. Prior attempts clearly showed, that for our purpose this resolution is sufficient. For a better visualization of the results, the illustrations of the LHF use shaded interpolation.

When evaluating $\mathcal{L}(\mathbf{r}; \mathbf{p}')$, we inherently encounter PO situations. If total PO occurs, i.e. if the arrival times of two MPCs are equal, then even the amplitude estimation (4.12) becomes an ill-posed problem, meaning that we cannot estimate the path amplitudes under these conditions. To prevent such situations, we make use of the prior floor plan information, and exclude overlapping MPCs from the estimation procedure. As threshold for the minimum time difference of two consecutive MPCs we choose $|\tau_i - \tau_j| \geq T_{\text{min. diff}} = T_p/20$, which ensures avoidance of numerical problems.

Finally, we also have to discuss a modification of the MLE, which is necessary to roughly compare its performance with the CRLB. We have mentioned several times, that the CRLB only makes statements about the estimation performance in the close vicinity of the agent position. However, as we will see soon, the MLE fails in many cases to find even the approximate agent position. To still compare the performance with the CRLB, we need to restrict the evaluation of $\mathcal{L}(\mathbf{r}; \mathbf{p}')$ to the area around the agent position. When limiting the considered area, we basically perform a MAP estimation when assuming uniform distribution of the agent position across the restricted area. Therefore, we will refer to this approach as MAP estimation. The MAP estimator will only consider positions with a maximum distance to the true agent position $||\mathbf{p} - \mathbf{p}'|| \leq r_{\text{map}}$, where we choose $r_{\text{map}} = 25\,\text{cm}$. In this area it computes $\mathcal{L}(\mathbf{r}; \mathbf{p}')$ with a grid spacing of 2 cm. For the comparison with the CRLB it makes sense to obtain even higher estimator resolution. This is achieved, by adding an additional estimation step where we perform a high resolution grid search within a radius of $r_{\text{map hr}} = 0.05\,\text{m}$ with a grid spacing of 2 mm around the previously found estimate. The used simulation parameters are finally summarized in Tab. 4.1.

	Parameter	Value	Description
Receiver		matched filter	receive filter
	T_s	0.25 ns	sampling interval
MLE	T_{obs}	200 ns	observation time
		0 ns . . . 50 ns	range of considered clock offset
		0.1 ns	resolution of the clock offset
		0.02 m	grid resolution
		$T_p/20$	min. difference of arrival times
MAP estimator	r_{map}	0.25 m	evaluation radius
		0.02 m	grid resolution
	$r_{\text{map hr}}$	0.05 m	high resolution evaluation radius
		0.002 m	grid high resolution

Table 4.1: *MLE and MAP simulation parameters*

4.4.2 A brief Comparison of TDOA and TOA

We start by comparing the log-LHF for TDOA and TOA. We will use the same parameters as in Chapter 3, i.e. the parameters specified in Tab. 2.1, for which the CRLB suggested good localization performance. The results are shown in Fig 4.1. In (a) the LHF for TOA is shown. It has its global maximum approximately at the true agent position. One can see some other local maxima, especially in the vicinity of the anchor, which could potentially cause the localization to fail. On the other hand, when looking at the TDOA case in (b), the big influence of the unknown clock offset becomes visible. The global maximum is at a completely wrong position, and in this case localization would clearly fail, although the CRLB suggests a low PEB. It is apparent, that we cannot apply the MLE directly. The question about the feasibility of a multipath assisted TDOA localization system arises, and requires us to study the problems in more detail.

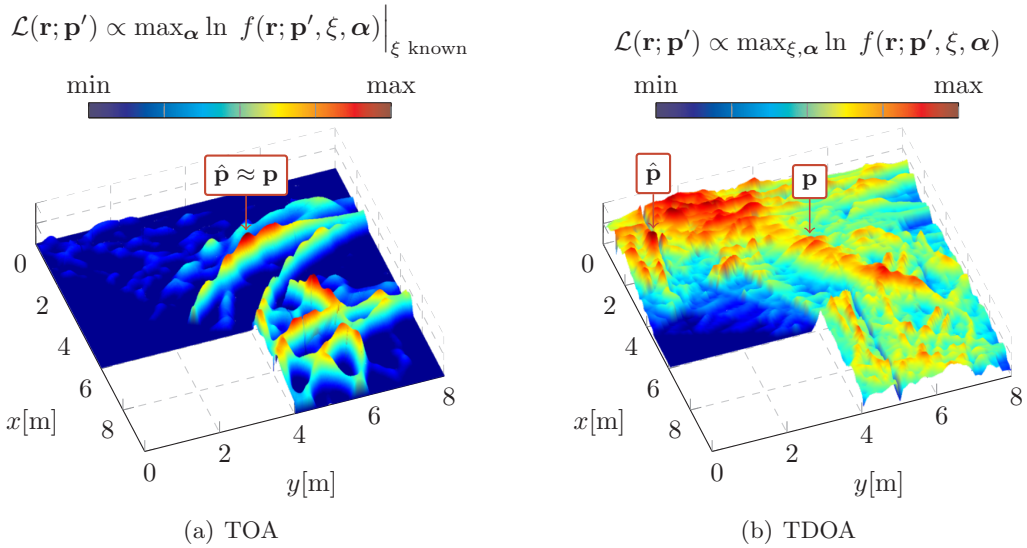

(a) TOA (b) TDOA

Figure 4.1: *Comparison of TOA and TDOA. The log-LHF for TOA (a) allows localization, while TDOA (b) fails although using the same parameters.*

4.4.3 Composition of the Log-Likelihood Function

We will now look at the composition of the log-LHF by gradually increasing the complexity of the estimation problem. Therefore we reduce the set of considered VAs, i.e. we will only consider the anchor and one, two or all VAs up to order two. The corresponding scenarios are shown in Fig. 4.2, with the agent at $\mathbf{p} = [2.5; 2.5]$, the anchor at $\mathbf{p}_1 = [8; 7]$, and the two additional VAs at $\mathbf{p}_2 = [-8; 7]$ and $\mathbf{p}_3 = [8; 9]$. The full set of VAs was shown in Fig. 2.7(b).

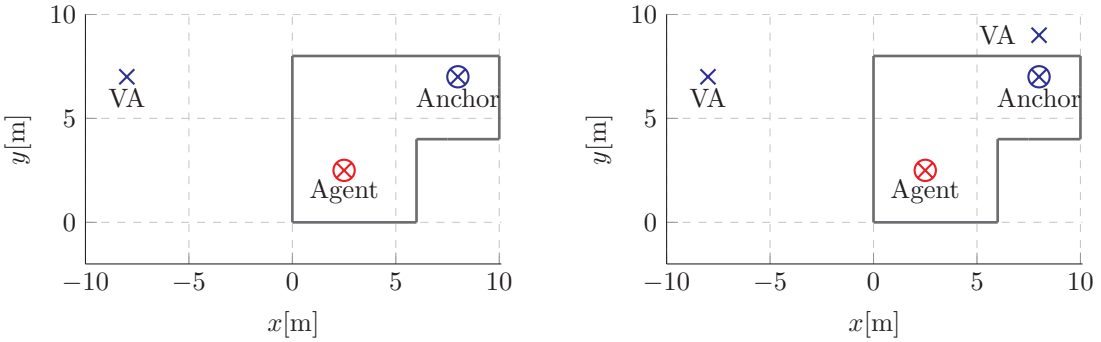

(a) Considering only the anchor and one additional VA

(b) Considering the anchor and two additional VAs

Figure 4.2: *Reduced VA sets for analyzing the composition of the LHF. We first look at the LHF for a scenario with only one anchor and one VA (a), and then add a 2^{nd} VA (b).*

In addition to reducing the set of VAs, we also choose the density of the observation noise and the power of diffuse multipath negligibly small. The log-LHF is shown in Fig. 4.3. As expected, the case where only one additional VA is considered leads to one visible hyperbola (a). Note that there exists a second one, but outside the room. Adding an additional VA in (b) results in already five overlapping hyperbolas. Furthermore, it is noticeable, how the hyperbola defined by the anchor and the VA at $\mathbf{p}_3 = [8; 9]$ broadens towards the agent position, since the anchor and the second VA are close to each other, but far away from the agent. Note that this hyperbola is a very important contribution for the localization, and its broadening can cause trouble when also considering noise. The position of the agent is clearly visible at the peak of the LHF. Considering all VAs up to order two leads to (c). The global maximum is at the true agent position. But we can already see that the LHF is highly multimodal, which can cause serious problems at different agent positions, especially if noise is involved.

The impact of diffuse multipath and observation noise is shown in Fig. 4.4. The noise components lead to additional hyperbolas, making the estimation problem even more difficult to handle. Using the whole set of second-order VAs clearly makes the position estimation infeasible.

The results above indicate a big problem when performing ML estimation: Even if no noise and diffuse MPCs are present, the LHF is highly multimodal. Without taking further measures we cannot ensure proper functionality of the TDOA localization.

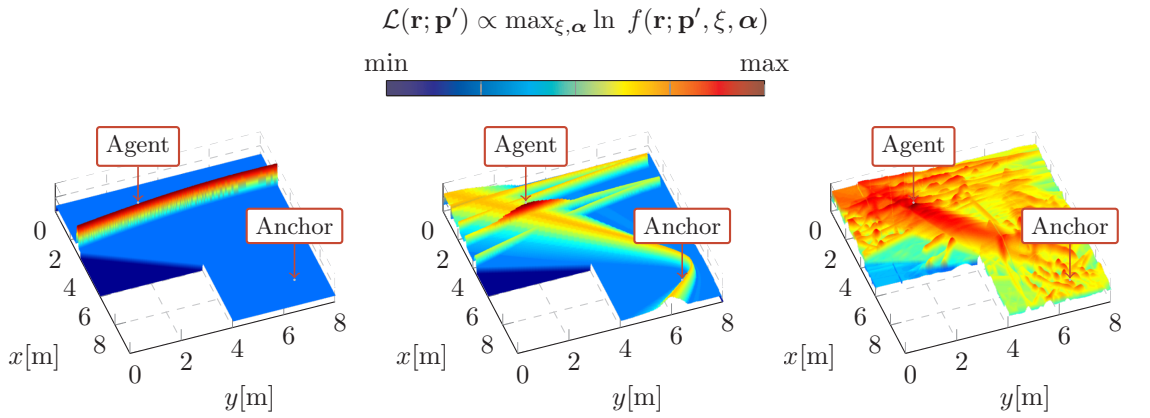

(a) Anchor and one VA (b) Anchor and two VAs (c) Anchor and all 2nd order VAs

Figure 4.3: *The LHF without the influence of noise. Both, the observation noise as well as diffuse multipath were choosen negliblly small. Furthermore only a reduced set of VAs is considered.*

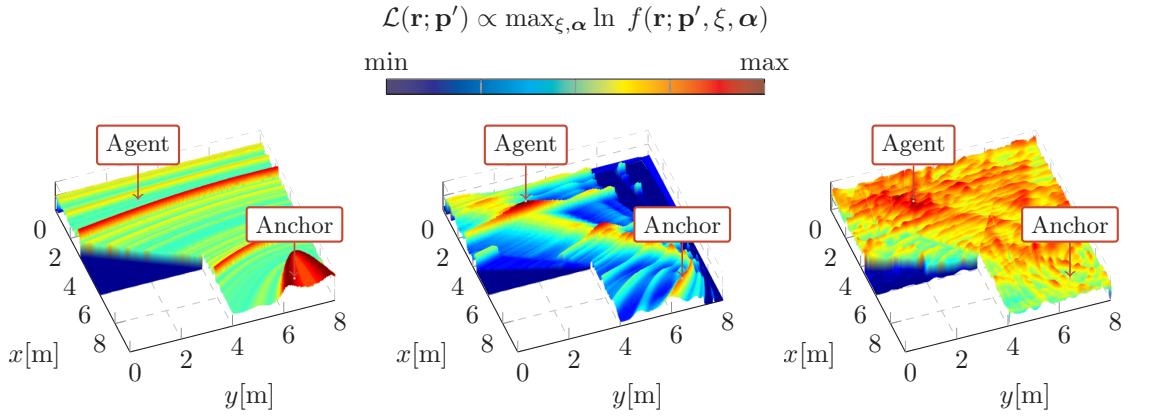

(a) Anchor and one VA (b) Anchor and two VAs (c) Anchor and all 2nd order VAs

Figure 4.4: *Influence of noise and diffuse multipath. In contrast to Fig. 4.3, now also the noise components are considered.*

4.4.4 Measures to Improve the Estimation Performance

We have identified some issues which arise when implementing an MLE. The next step is to find a way to circumvent these problems. We have already discussed some options to reduce the PEB in Chapter 3: e.g. increasing the signal bandwidth, using multiple anchors etc. Now we will apply these and also other measures to the MLE, with the focus on how they affect the shape of the LHF.

We saw in the previous section that noise, and therefore the SINRs of the deterministic MPCs are important factors. Therefore the following evaluation is performed for a low-SINR and a high-SINR scenario. The former uses the parameters as defined in Tab. 2.1 ($N_0 = 10^{-8}, \Omega_1 = 1.16 \cdot 10^{-6}$). This results in a constant SNR for the diffuse multipath across the floorplan, with $\mathrm{SNR}_{\mathrm{diff}} = 20.6\,\mathrm{dB}$. At the agent position $\mathbf{p} = [3.5; 4.5]^T$ the LOS component has the $\mathrm{SINR}_{\mathrm{LOS}} = 15.8\,\mathrm{dB}$, and the SINR of all reflected MPCs is at $\mathrm{SINR}_{\mathrm{total}} = 9.8\,\mathrm{dB}$. The high-

SINR scenario uses $N_0 = 10^{-10}$ and $\Omega_1 = 1.16 \cdot 10^{-7}$, which results in $\mathrm{SNR}_{\mathrm{diff}} = 30.7\,\mathrm{dB}$, $\mathrm{SINR}_{\mathrm{LOS}} = 32.5\,\mathrm{dB}$ and $\mathrm{SINR}_{\mathrm{total}} = 21.3\,\mathrm{dB}$.

In Fig. 4.5 the likelihood is shown for the low-SINR scenario in (a) and for the high SINRs scenario in (b). In the latter case the reduction of noise leads to a distinctive peak at the agent position, and the general assumption about the beneficial effect of high SINR is comprehensible. The SINRs also played a crucial role for the CRLB, and one should in any case try to reduce it. However, while measures can be taken to reduce the observation noise, the power of the diffuse multipath is rather difficult to influence, since it depends on the transmit power as well as the physical properties of the indoor environment.

That high SINRs are still no guarantee for failsafe localization is clearly shown in Fig. 4.6. The agent is now located at $\mathbf{p} = [5; 0.5]^T$, which means that we have to deal with an NLOS situation. No matter if we examine the low or high-SINR scenario, the position estimation fails. However, for the high-SINR case in (b) at least a local maximum can be observed. Under certain circumstances one can make use of this peak.

The positive effect of a reduced pulse duration ($T_p = 0.5\,\mathrm{ns}$) is shown in Fig. 4.7. When comparing it with the results for $T_p = 1\,\mathrm{ns}$ (Fig. 4.5), we notice the much more distinct peaks of the likelihood, which suggests that the position estimation can be performed more accurately. This also matches the observations when examining the CRLB, where we saw that the signal bandwidth directly scaled the EFIM and the PEB. But it is only an effective measure, when considering a high-SINR scenario as shown in (b), otherwise we still cannot ensure proper functionality (a). So a reduction of the pulse duration is only effective when combining it with some other countermeasures, and comes at the cost of enhanced bandwidth requirements.

A much cheaper countermeasure could be to restrict to first-order VAs. This is somehow counterintuitive, since each additional VA adds information for the position estimation. But on the other hand, the results when using only first-order VAs (Fig. 4.8) indicate, that this affects the shape of the log-LHF in a way, so that the large number of distinct local maxima is clearly reduced. And again to address the increase of the PEB: This measure can be used in a two-step approach, i.e. first performing coarse localization with the reduced VA set, and afterwards performing high resolution localization with the full VA set, but restricting to the vicinity of the previously found estimate. However, in Section 4.5 we apply this measure to measurement data without success. In a realistic scenario it seems to be better not to restrict to first-order VAs, but to a rather small set of significant VAs with high SINRs.

When assuming prior knowledge of the clock offset, which could be available due to coarse synchronization, the results for TDOA in Fig. 4.9 resemble the ones for TOA in Fig. 4.1 (a). Here we assumed the clock offset to be uniformly distributed in an interval $[-1\,\mathrm{ns}, 1\,\mathrm{ns}]$, i.e. $\xi \sim \mathcal{U}(-1\,\mathrm{ns}, 1\,\mathrm{ns})$. It can be seen that even a clock synchronization in the range of nanoseconds would greatly improve the reliability of the estimator.

Finally, the relatively simple yet effective approach with two asynchronous anchors is examined. The analysis in Section 3.5 emphasized the beneficial influence of multiple anchors on the PEB. This is not only true when examining the CRLB, but also when looking at the LHF in Fig. 4.10. Especially in the high-SINR case (b) the global maximum is now well above the other local maxima when comparing it with the single-anchor case Fig. 4.5 (b). When using two synchronized anchors, the resulting LHF does not differ very much, therefore it is not shown.

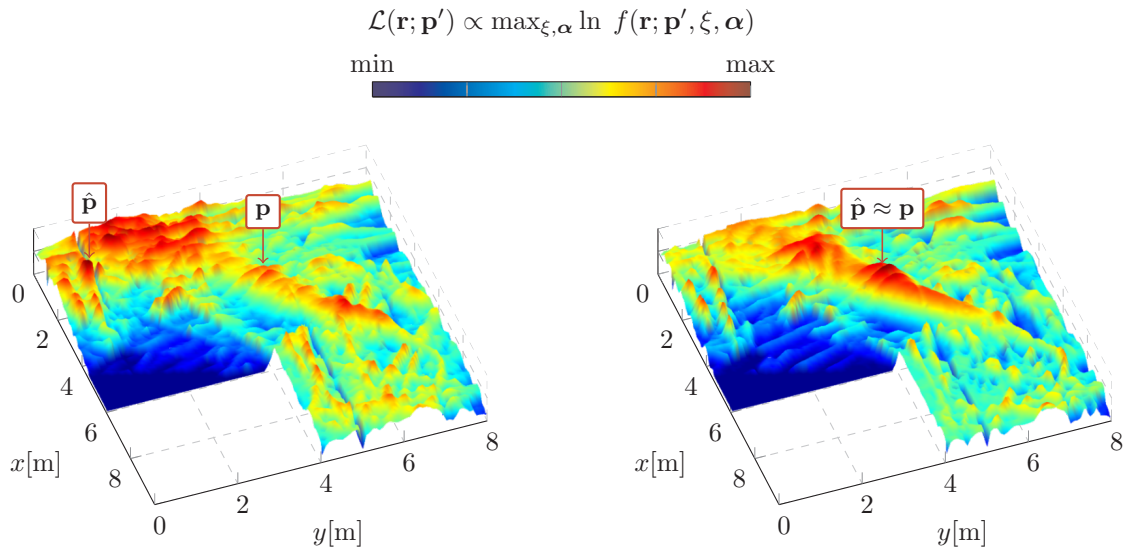

(a) Low SINR, $\mathbf{p} = (3.5; 4.5)^T$, $\hat{\mathbf{p}} = (1.72; 0.84)^T$ (b) High SINR, $\mathbf{p} = (3.5; 4.5)^T$, $\hat{\mathbf{p}} = (3.56; 4.36)^T$

Figure 4.5: *Multimodality of the log-LHF.* $T_p = 1\ ns$, $\mathbf{p} = [3.5; 4.5]^T$.

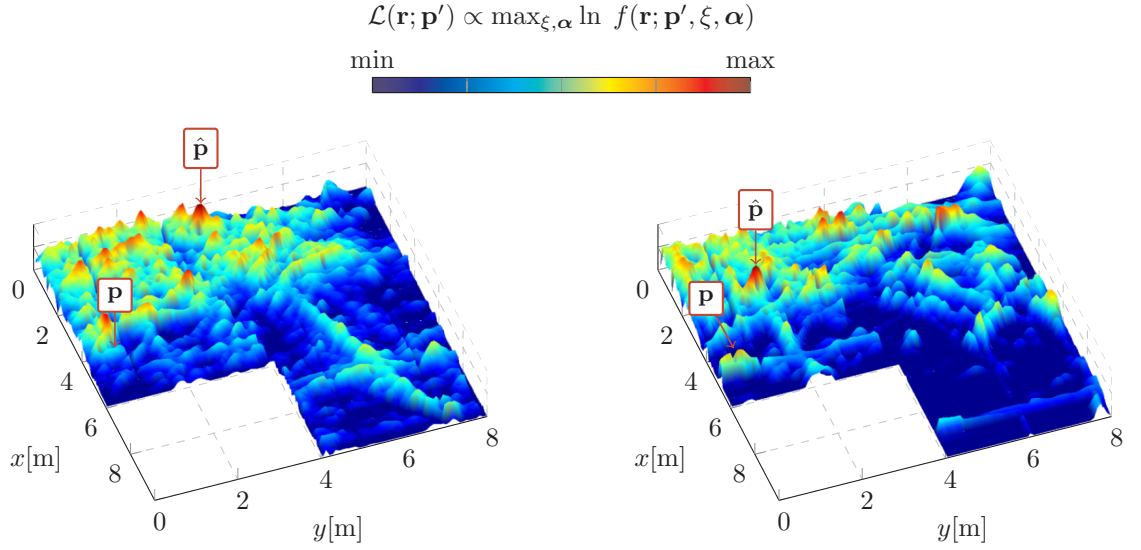

(a) Low SINR, $\mathbf{p} = (5; 0.5)^T$, $\hat{\mathbf{p}} = (0.76; 3.8)^T$ (b) High SINR, $\mathbf{p} = (5; 0.5)^T$, $\hat{\mathbf{p}} = (2.44; 1.64)^T$

Figure 4.6: *The log-LHF in case of a NLOS scenario.* $T_p = 1\ ns$, $\mathbf{p} = [5; 0.5]^T$.

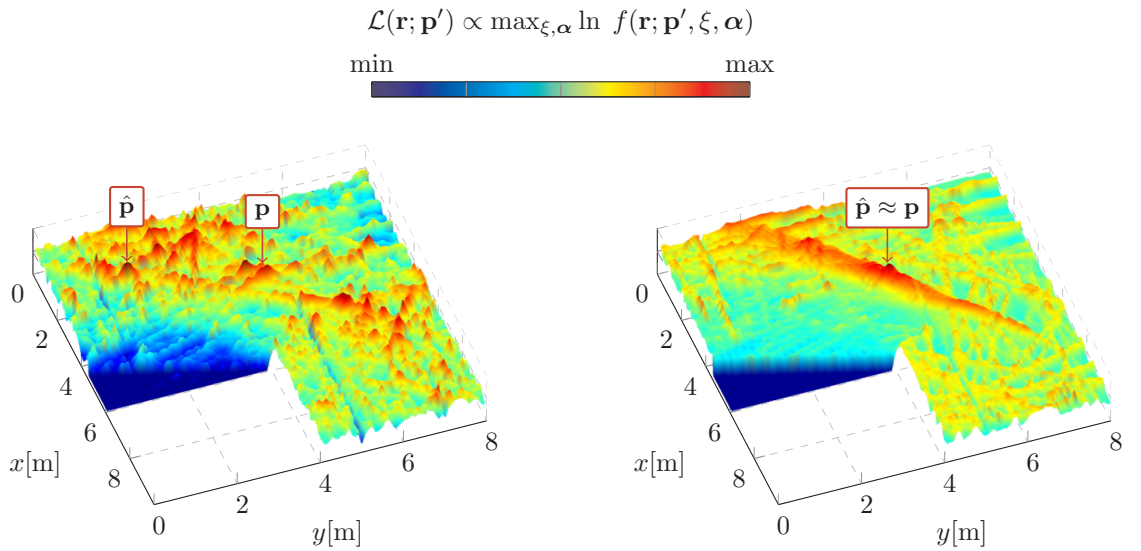

(a) Low SINR, $\mathbf{p} = (3.5; 4.5)^T$, $\hat{\mathbf{p}} = (2.12; 1.64)^T$

(b) High SINR, $\mathbf{p} = (3.5; 4.5)^T$, $\hat{\mathbf{p}} = (3.48; 4.52)^T$

Figure 4.7: *Influence of a reduced pulse duration.* $T_p = 0.5\,ns$, $\mathbf{p} = [3.5; 4.5]^T$.

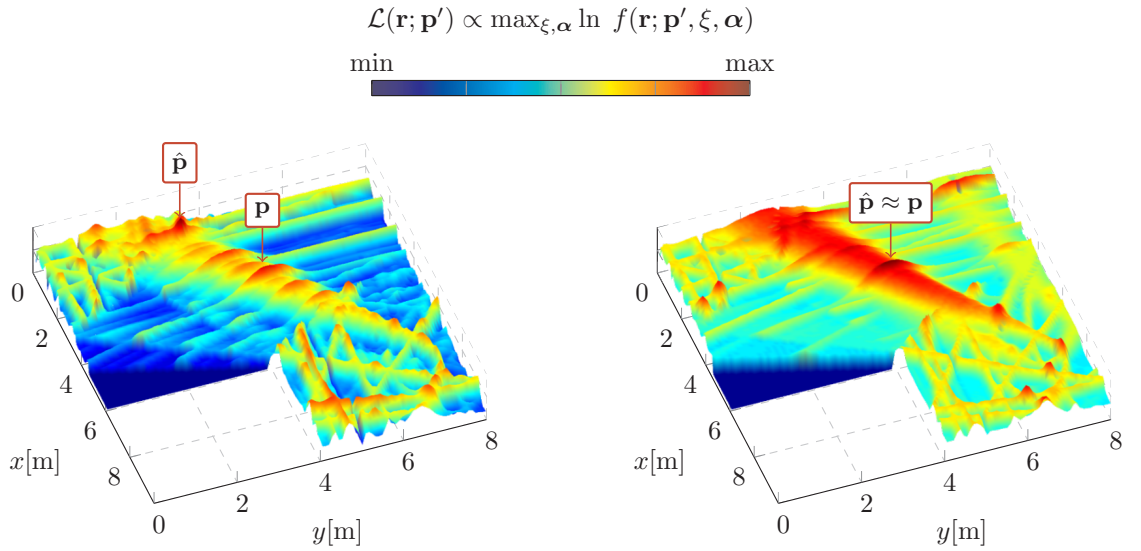

(a) Low SINR, $\mathbf{p} = (3.5; 4.5)^T$, $\hat{\mathbf{p}} = (1; 3.24)^T$

(b) High SINR, $\mathbf{p} = (3.5; 4.5)^T$, $\hat{\mathbf{p}} = (3.48; 4.60)^T$

Figure 4.8: *Using only first-order VAs for the ML estimation.* $T_p = 1\,ns$, $\mathbf{p} = [3.5; 4.5]^T$.

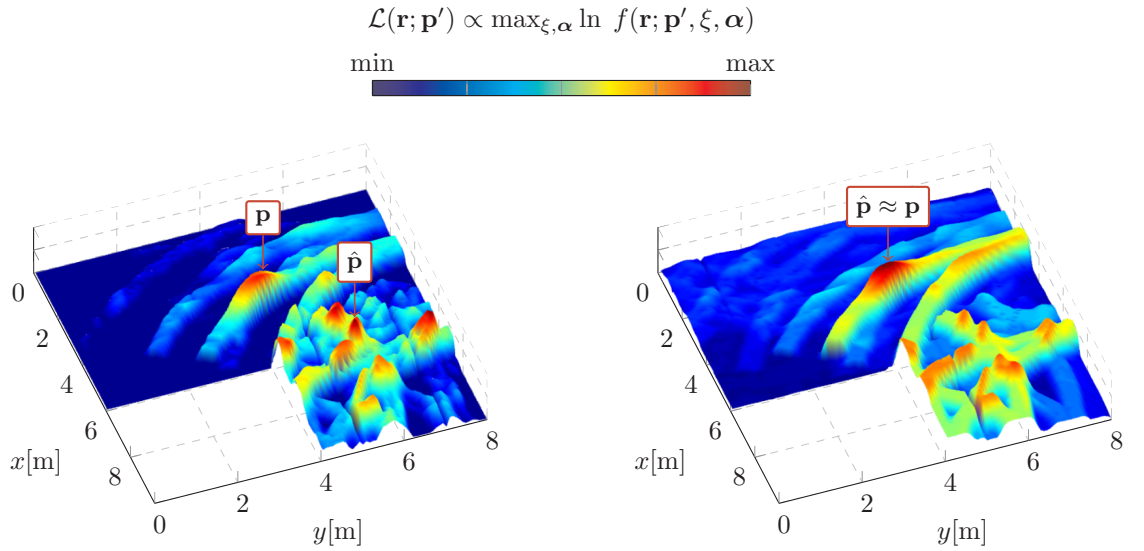

(a) Low SINR, $\mathbf{p} = (3.5; 4.5)^T$, $\hat{\mathbf{p}} = (6.6; 5.8)^T$

(b) High SINR, $\mathbf{p} = (3.5; 4.5)^T$, $\hat{\mathbf{p}} = (3.48; 4.52)^T$

Figure 4.9: *The log-LHF when having prior knowledge about the clock offset.* $T_p = 1\,ns$, $\mathbf{p} = [3.5; 4.5]^T$, $\xi \sim \mathcal{U}(-1\,ns, 1\,ns)$.

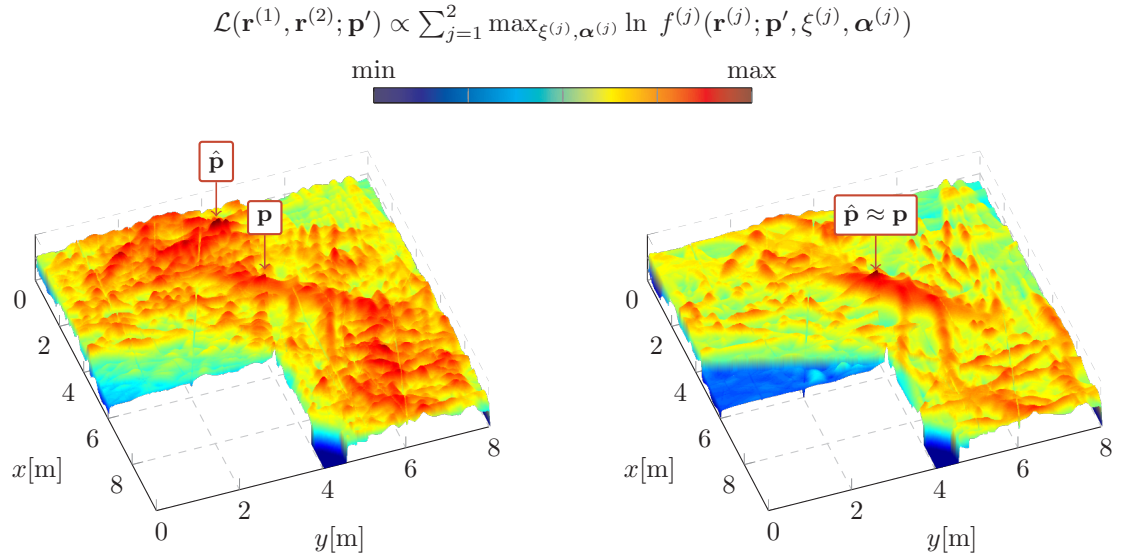

(a) Low SINR, $\mathbf{p} = (3.5; 4.5)^T$, $\hat{\mathbf{p}} = (1.11; 4.03)^T$

(b) High SINR, $\mathbf{p} = (3.5; 4.5)^T$, $\hat{\mathbf{p}} = (3.51; 4.47)^T$

Figure 4.10: *Log-LHF when using two asynchronous anchors.* $T_p = 1\,ns$, $\mathbf{p} = [3.5; 4.5]^T$.

Still, none of the measures above was able to deal with the *low-SINR* scenarios. However, in all these scenarios in Fig. 4.5-4.10 (a) one can recognize a local maximum at the true agent position, which can be helpful when assuming prior knowledge about the agent position, e.g. from a agent tracking algorithm.

From these results we can conclude, that multipath-assisted TDOA localization can be enabled in principal, provided that the SINRs are sufficiently high. Reliability can be enhanced by a useful combination of the measures above. To also obtain some degree of robustness, the additional use of tracking algorithms is most likely mandatory.

4.4.5 Comparison with the Cramer Rao Lower Bound

We now assess the small-scale estimator performance, and attempt to compare the achievable localization performance with the CRLB. Note that it is not appropriate, to compare the MLE directly with the CRLB, since we already saw that we permanently have to deal with outliers. To still get an appropriate comparison, we need to restrict to the local maximum of the LHF closest to the true agent position.

A possible way to solve this problem is to use the modified MLE, i.e. the MAP estimator defined in Section 4.4.1. This means that we still perform ML estimation, but only consider the area around the agent position. Performing the position estimation for 1000 realizations of the received signal (also with different realizations of the diffuse multipath) allows to compute a sufficiently accurate covariance matrix $\mathbf{C}_{\hat{\mathbf{p}}}$ of the estimates $\hat{\mathbf{p}}$. We can then compare the concentration ellipses defined by $\mathbf{C}_{\hat{\mathbf{p}}}$ with the error ellipses defined by the CRLB.

A scatter plot showing the estimates $\hat{\mathbf{p}}$ is shown in Fig. 4.11 (a). It was performed using a single anchor with $T_p = 1\,\text{ns}$, assuming a medium-SINR scenario with $N_0 = 10^{-9}$ and $\Omega_1 = 0.55 \cdot 10^{-6}$ ($\text{SNR}_{\text{diff}} = 27.6\,\text{dB}$, $\text{SINR}_{\text{LOS}} = 24.1\,\text{dB}$, $\text{SINR}_{\text{total}} = 14.1\,\text{dB}$). In (b) and (c) are the scatter plots for the low and high-SINR scenarios as defined in Section 4.4.4 shown. In all three cases the mass of the estimates is clearly around the true agent position $\mathbf{p} = [3.5; 4.5]^T$, indicating that the estimates are unbiased. The concentration ellipse (colored black) shows similar orientation as the error ellipse (green), and also its sizes match well, especially for the high-SINR case. For medium SINR the concentration ellipse is slightly spread. In the low-SINR case the evaluation radius is too small to assess the concentration ellipse. The histograms on the outside of (a) give us a hint about the distribution function of the estimates. Resembling the distribution of a Gaussian random variable, this confirms the validity and significance of the concentration ellipse as performance measure for the estimator.

The empirical CDFs for the localization error are shown in Fig. 4.12. Also shown are the CDFs as expected from the CRLB, which again allows for a comparison of the MLE performance with the CRLB. For high SINRs, the results of the MLE match the CDFs of the CRLB very well. When examining the medium-SINR case, the connection between the CRLB and the MLE performance is still evident, but not as well as for the high-SINR scenario. In the low-SINR case it can be seen that the comparison is not proper, since the restriction of the examined area due to the MAP estimator falsifies the statistics.

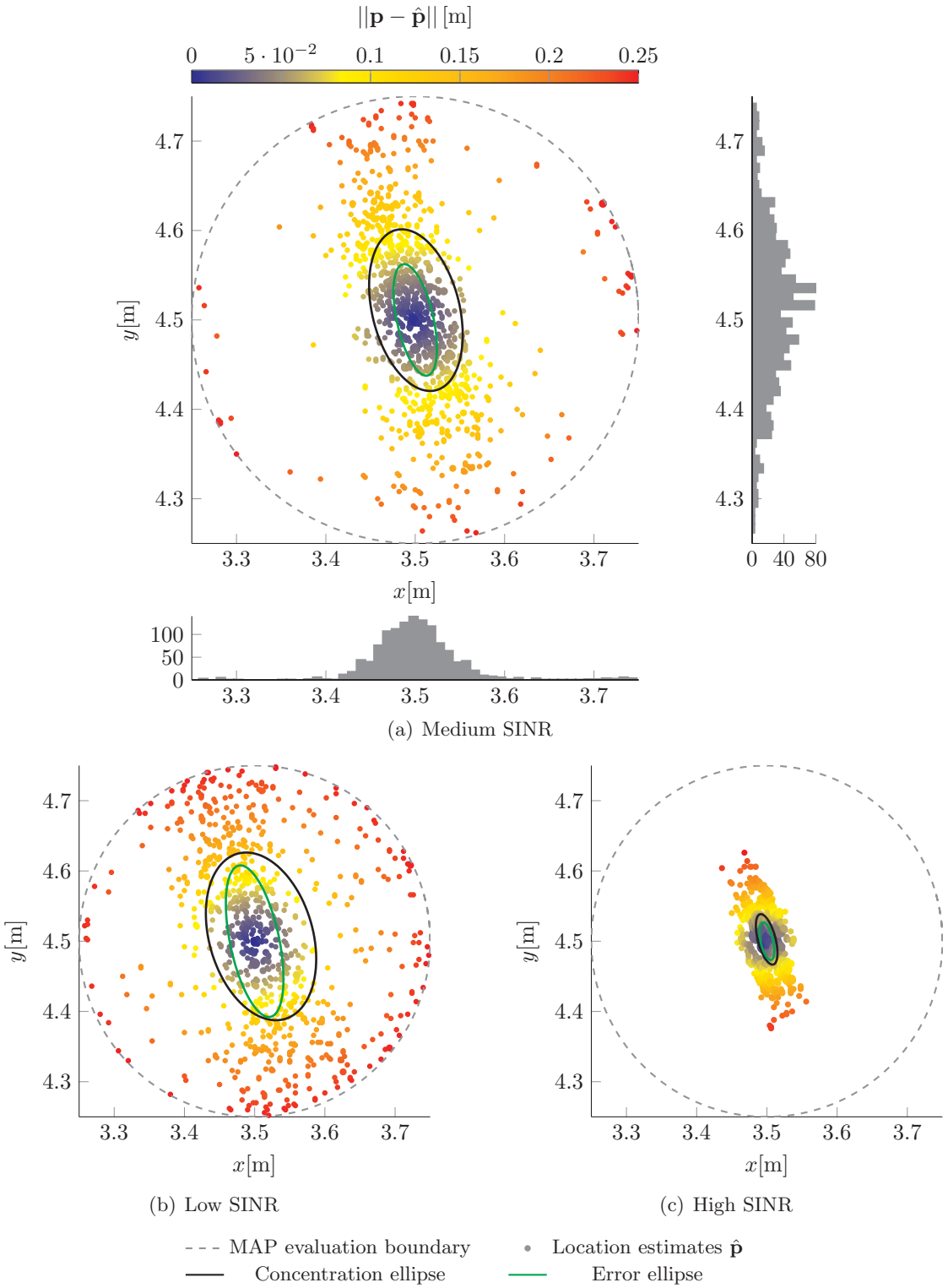

Figure 4.11: *Comparison of the MAP estimator performance with the CRLB. The influence of different SINRs is shown. Fig. (a) shows a medium-SINR scenario, whereas (b) and (c) show the results for the low- and high-SINR cases, respectively.* $T_p = 1\,ns$, $\mathbf{p} = [3.5; 4.5]^T$.

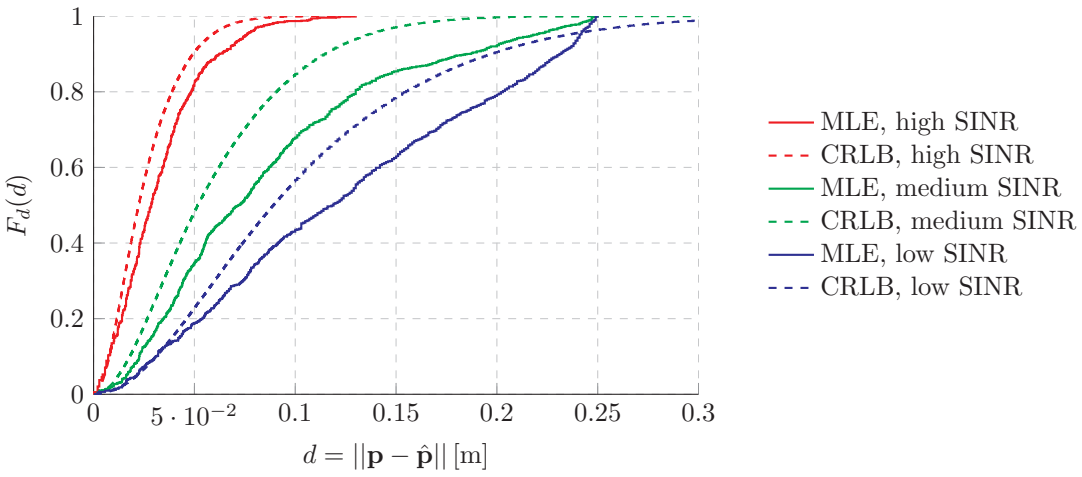

Figure 4.12: *CDF comparison of the MAP estimator performance. The empirical CDFs of the estimates are shown for the low-, medium- and high-SINR scenarios. Additionally, the CDFs as expected from the CRLB are illustrated.*

4.5 Evaluation based on Measurement Data

We complete the chapter by applying the ML estimation on measurement data collected in a real indoor environment. The purpose is to demonstrate the applicability and principal functionality of multipath-assisted TDOA localization on measurement data.

4.5.1 Scenario Description and Signal Parameters

The used measurement data originate from a measurement campaign [27], performed in an indoor environment with the floor plan shown in Fig. 4.13. The localization infrastructure consisted of two anchors, located at $\mathbf{p}_1^{(1)} = [0.5; 7]^T$ and $\mathbf{p}_1^{(2)} = [5.2; 3.2]^T$.

The agent was moved along the red colored trajectory in 5 cm steps, which results in $L = 220$ agent positions. For each of these the CIR was recorded. In addition, measurements were taken on a 5×5 grid around each agent position, with one centimeter spacing (this is also illustrated in Fig. 4.13). These additional measurements are used for the estimation of the covariance matrix of the diffuse multipath, which is described in the next section.

Postprocessing of the CIR data results in the complex-valued baseband signals for both anchors and all L trajectory positions. The postprocessing is performed for an RC pulse, with pulse duration $T_p = 0.5\,\text{ns}$ and roll-off factor $\beta = 0.5$. The sampling frequency is $f_s = 1/0.144\,\text{ns} \approx 6.95\,\text{GHz}$.

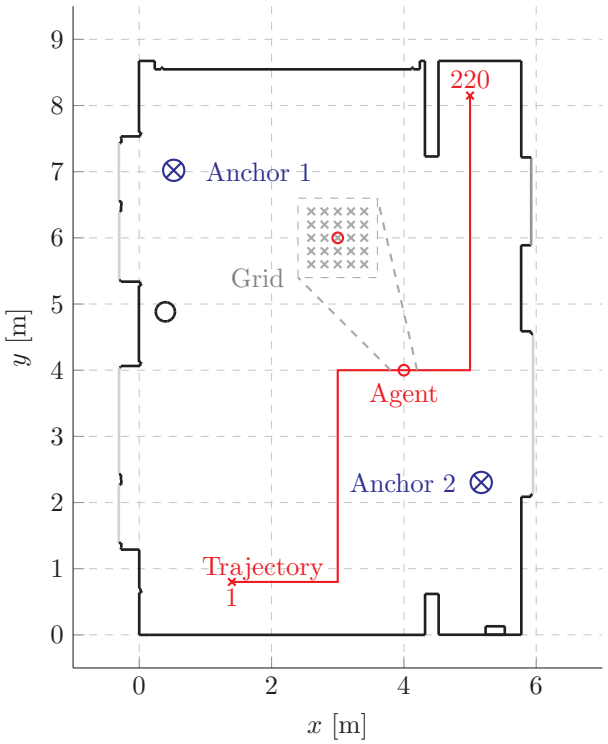

Figure 4.13: *Floor plan of the indoor environment. Windows and doors are drawn light and dark gray, respectively. Also illustrated are the two anchors (blue), the agent trajectory (red) and the* 5×5 *measurement grid.*

4.5.2 Estimation Procedure

Before we can apply the MLE as defined in Section 4.2.4, we need to perform the additional steps of VA relocation and covariance estimation as follows:

The VA relocation is solely done to eliminate uncertainties of the floor plan information, and yields an updated set of VAs. For this purpose the relocation process makes use of the measurement data as well as the known agent position along the trajectory to estimate the VA locations. More details about the algorithm can be found in [28]. We use the resulting updated set of VAs throughout the remaining computations.

In order to achieve the maximum possible estimator performance, a sufficiently accurate estimation of the covariance matrix is needed. This is a challenging task on its own, and out of scope of this work. Instead we will simply use the $M = 25$ measurements $\mathbf{r}_m, m = 1, \ldots, M$, on the grid around a specific agent position, and estimate the covariance matrix $\hat{\mathbf{C}}$ as follows,

$$\hat{\mathbf{C}} = \frac{1}{M} \sum_{m=1}^{M} (\mathbf{r}_m - \tilde{\mathbf{s}}) (\mathbf{r}_m - \tilde{\mathbf{s}})^{\mathrm{H}} .$$

Here $\tilde{\mathbf{s}}$ denote again the deterministic signal components (4.2), which are computed using the knowledge of the agent position $\mathbf{p}$ and the relocated VAs. This approach yields for our purpose sufficiently accurate estimates of the covariance matrix.

Thus all prerequisites are fulfilled, and the localization can be performed as described in

Sections 4.2.4 and 4.3. Note that we again only use the main diagonal of the covariance matrix for computational reasons.

4.5.3 Performance Results

Performing the localization with a single anchor and assuming prior knowledge on the distribution of the clock offset $\xi \sim \mathcal{U}(-10\,\text{ns}, 10\,\text{ns})$ leads as expected to a rather large number of outliers and hence a poor performance. The results are shown in Fig. 4.14 (a). Here all the estimates of the agent positions are drawn on the floor plan, which gives us an idea of the functionality of the MLE for the present problem. No matter whether using VA order one or two (blue and green colored crosses, respectively), the number of outliers is unacceptably high. The estimation based on only first-order VAs shows slightly better results. Much better are the results for $\xi \sim \mathcal{U}(-1\,\text{ns}, 1\,\text{ns})$ (b). In contrast to (a), now the number of outliers is reduced when using VAs up to order of two.

Localization results using two anchors are shown in Fig. 4.14 (c) and (d). Again, in (c) prior knowledge of $\xi \sim \mathcal{U}(-10\,\text{ns}, 10\,\text{ns})$ is assumed, while (d) is for $\xi \sim \mathcal{U}(-1\,\text{ns}, 1\,\text{ns})$. Interestingly, comparing (c) with (b) reveals that the two-anchor system with $\xi \sim \mathcal{U}(-10\,\text{ns}, 10\,\text{ns})$ is more vulnerable to localization errors due to outliers than the single-anchor system with $\xi \sim \mathcal{U}(-1\,\text{ns}, 1\,\text{ns})$, highlighting the importance of clock synchronization. Best performance is achieved with the two-anchor system assuming $\xi \sim \mathcal{U}(-1\,\text{ns}, 1\,\text{ns})$, as can be seen in (d). Note that in neither case it was possible to localize the agent in the upper part of the trajectory. The results in this part of the trajectory are not illustrated for better clarity.

Figure 4.15 shows the obtained results in terms of the localization error $||\mathbf{p} - \hat{\mathbf{p}}||$ along the trajectory (the results for a single anchor with poor prior knowledge are not illustrated, due to the high number of outliers). Here (a) was obtained assuming the single anchor system with $\xi \sim \mathcal{U}(-1\,\text{ns}, 1\,\text{ns})$, while (b) and (c) are for two anchors with $\xi \sim \mathcal{U}(-10\,\text{ns}, 10\,\text{ns})$ and $\xi \sim \mathcal{U}(-1\,\text{ns}, 1\,\text{ns})$, respectively. Together with the CDF comparison in Fig. 4.16, these results confirm the observations made before. They also show that, with minor exceptions, the use of VAs up to order two results in a smaller localization error.

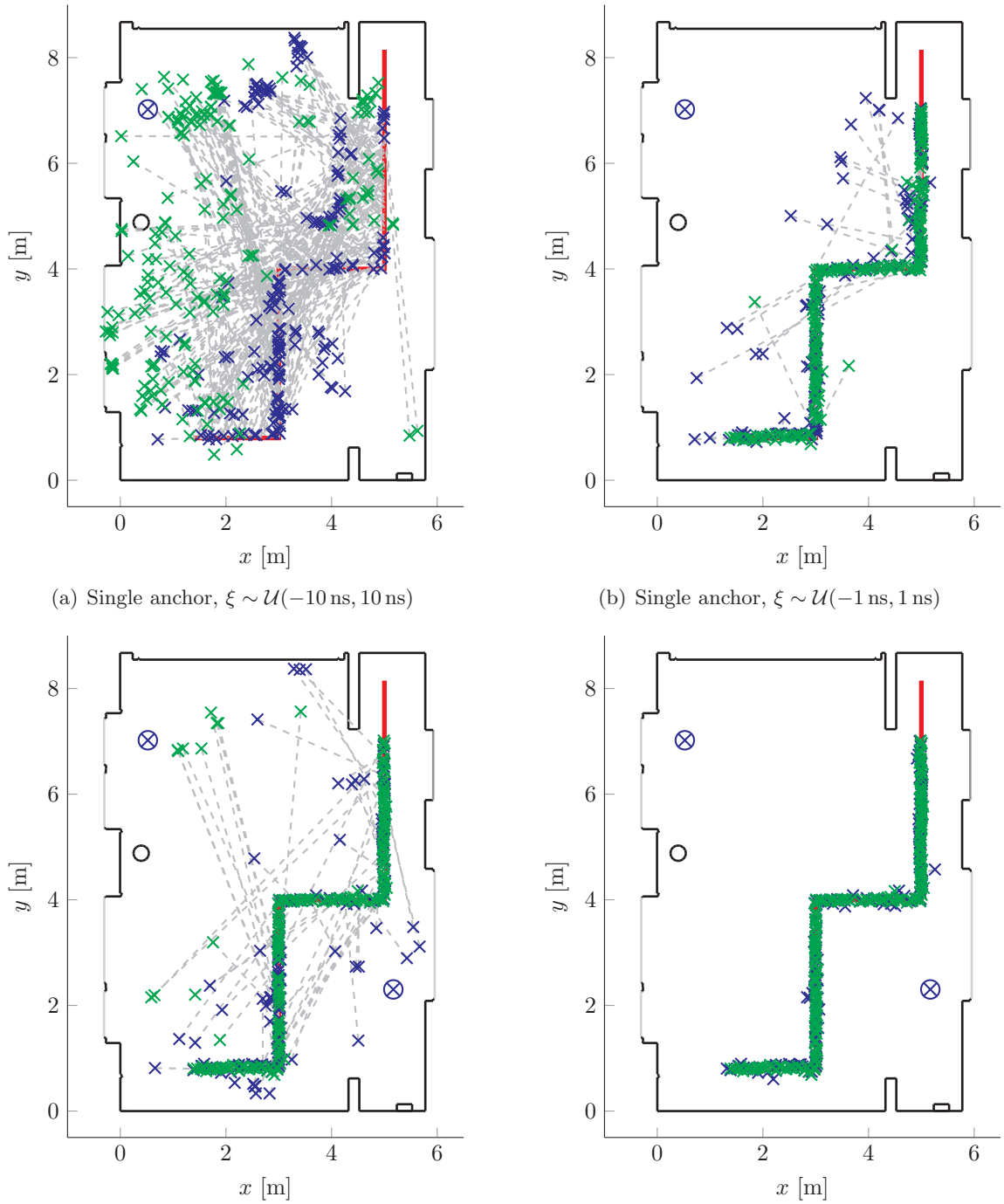

(a) Single anchor, $\xi \sim \mathcal{U}(-10\,\text{ns}, 10\,\text{ns})$

(b) Single anchor, $\xi \sim \mathcal{U}(-1\,\text{ns}, 1\,\text{ns})$

(c) Two asynchronous anchors, $\xi \sim \mathcal{U}(-10\,\text{ns}, 10\,\text{ns})$

(d) Two asynchronous anchors, $\xi \sim \mathcal{U}(-1\,\text{ns}, 1\,\text{ns})$

$\times\,\hat{\mathbf{p}}$, using VA order 1 $\times\,\hat{\mathbf{p}}$, using VA order 2

Figure 4.14: *Performing multipath-assisted TDOA localization along a trajectory in a real indoor environment. The illustrations show the estimated positions for a single-anchor in (a) and (b), and for two-anchors in (c) and (d). In (b) and (d) we assume prior knowledge on the clock offset:* $\xi \sim \mathcal{U}(-1\,ns, 1\,ns)$*. The green crosses denote estimates based on the ML estimation using VA order one, while the blue crosses are for the case when using VA order two.*

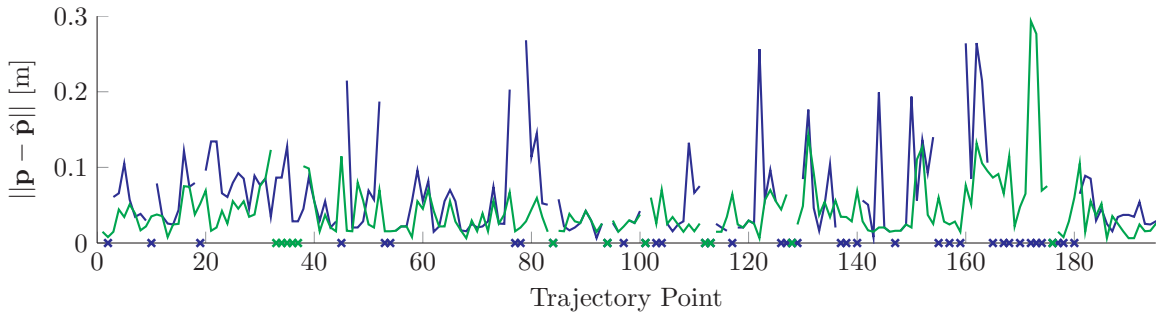

(a) Single anchor, prior knowledge $\xi \sim \mathcal{U}(-1\,\text{ns}, 1\,\text{ns})$

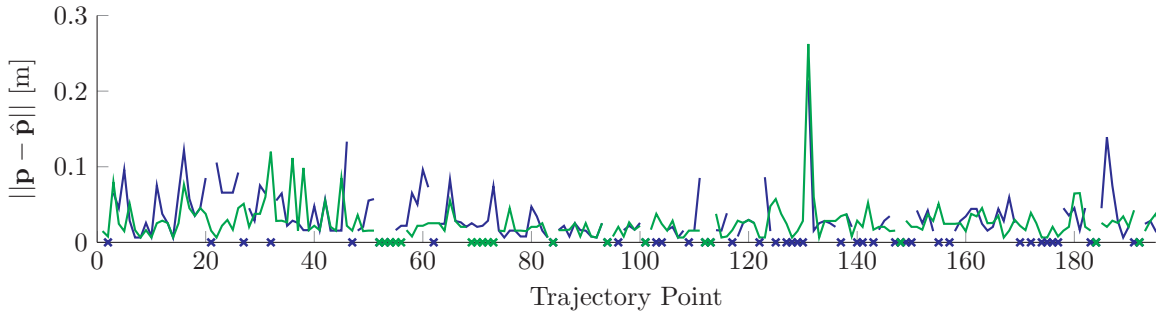

(b) Two asynchronous anchors, prior knowledge $\xi \sim \mathcal{U}(-10\,\text{ns}, 10\,\text{ns})$

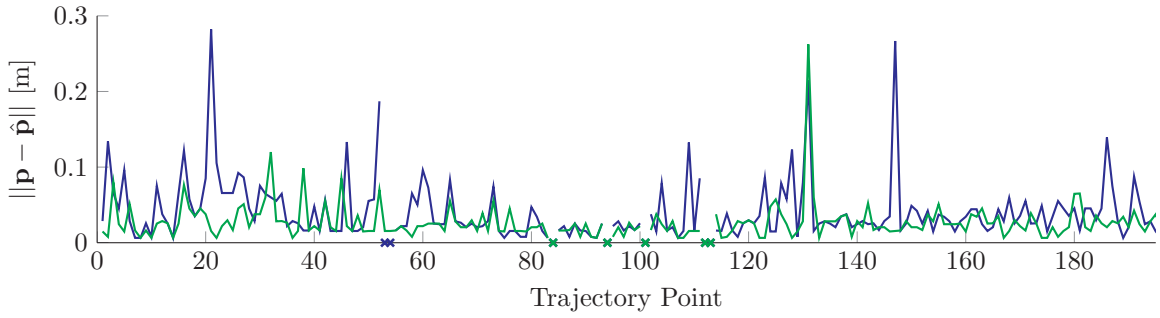

(c) Two asynchronous anchors, prior knowledge $\xi \sim \mathcal{U}(-1\,\text{ns}, 1\,\text{ns})$

Figure 4.15: *Localization error along the trajectory when using two asynchronous anchors. The localization error $||\mathbf{p} - \hat{\mathbf{p}}||$ is shown for every trajectory position. (a) shows the results when using a single anchor with $\xi \sim \mathcal{U}(-1\,ns, 1\,ns)$, while (b) and (c) are for the cases with two asynchronous anchors and $\xi \sim \mathcal{U}(-10\,ns, 10\,ns)$ and $\xi \sim \mathcal{U}(-1\,ns, 1\,ns)$, respectively. The results are shown for VA order one and two.*

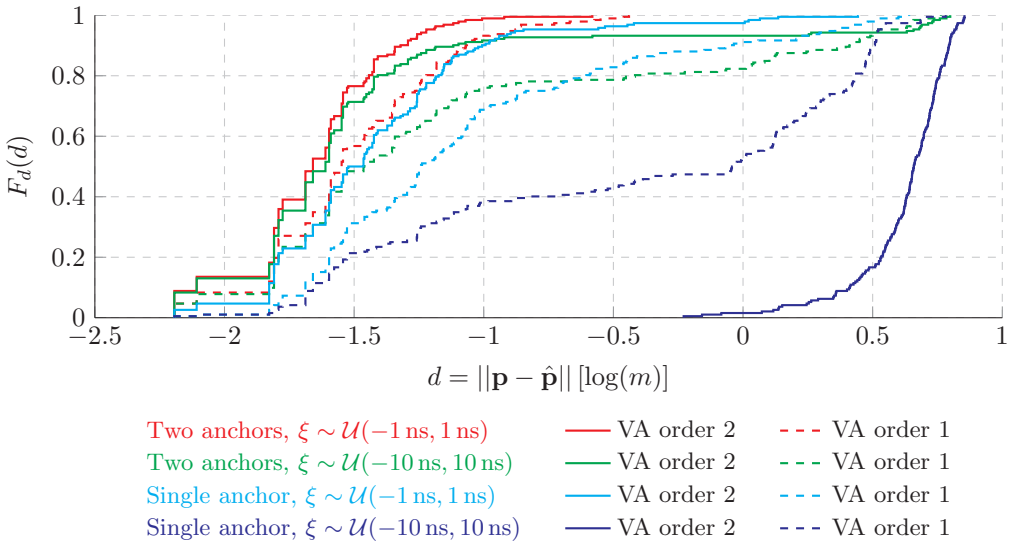

Figure 4.16: *CDF comparison of the localization error along the trajectory. Best performance is obtained when using two anchors with prior knowledge* $\xi \sim \mathcal{U}(-1\,ns, 1\,ns)$. *When having* $\xi \sim \mathcal{U}(-10\,ns, 10\,ns)$ *the additional outliers can be seen. Also good performance is achieved when using a single anchor with* $\xi \sim \mathcal{U}(-1\,ns, 1\,ns)$. *In general, the use of VAs up to order two provides better localization performance than restricting to first-order VAs.*

5 Conclusion and Outlook

This thesis provides an in-depth analysis of multipath-assisted indoor localization in presence of a clock offset. We examined the theoretical limits of localization performance, and compared the results with the performance of an actual estimator implementation.

5.1 Conclusion

The derivation and analysis of the CRLB gives us helpful insight into the estimation problem. Similar as for TOA, it highlights that when considering areas not affected by path overlap, *each deterministic signal component (i.e. each VA) contributes information to the estimation problem*, which increases the localization accuracy. The amount of information depends on the effective signal bandwidth and on the SINRs of the deterministic signal components. The former is a design parameter and is only limited by technological feasibility and legal regulations, while the latter depends on multiple factors such as the transmit power, attenuation of signal reflections (and hereby material properties of the indoor environment), observation noise and diffuse multipath.

As expected, *the comparison with TOA shows a performance degradation* caused by the unknown clock offset. The differences mainly depend on the geometrical conditions, and hereby on the indoor environment. Still the results suggest that *good localization performance is achievable*. If the performance is not sufficient, effective *countermeasures* are presented in order to circumvent the performance loss:

- *Increasing the signal bandwidth* has the positive effect of scaling the EFIM, thus reducing the CRLB. The shorter pulse duration also decreases the areas which are affected by path overlap. All this comes at the high cost of additional bandwidth.
- *Extending the localization infrastructure* by additional anchors not only leads to a reduced CRLB, but also reduces vulnerability against path overlap situations, enhances room coverage, and improves localization under NLOS conditions or in case of reduced signal reflectivity.

The analysis of the MLE covers open issues which are ignored when examining the CRLB. The results point out that the performance suggested by the *CRLB is attainable only with the use of additional measures*. Thereby *multimodality of the LHF* turns out to be a major issue, which causes the estimation procedure to fail in many cases. The evaluation of counter-measures yields the following possibilities:

- Keeping the *SINR as high as possible* leads to a smoother shape of the LHF, which helps to identify the correct agent position. Hence, an increase of the transmit power as well as choosing a high signal bandwidth have a positive effect.
- Increasing the *signal bandwidth* not only leads to better performance in terms of the CRLB and higher SINRs, but also to more distinct peaks in the LHF, which makes the recognition of the maximum easier.
- Choosing a rather *small VA-order for a coarse localization* can make the estimation of the agent position easier, due to the reduced number of distinct modes of the LHF, but in general the use of a higher VA-order is preferable.
- The positive properties when using *multiple anchors* are not only evident when examining the CRLB, but also when looking at the resulting LHF, as it has a much more distinct local maximum.
- If *prior information on the clock offset* is available, e.g. from a coarse synchronization, this greatly reduces the multimodality of the LHF.
- Finally *prior information on the agent position*, e.g. provided by a tracking algorithm, restricts the search area and hereby makes position estimation not only more robust, but also reduces the computational expenses.

In order to obtain the best possible estimator performance, a carefully selected combination of these countermeasures seems to be most efficient. If we can assure that the global maximum of the LHF is on average at the agent position, then *the performance suggested by the CRLB is roughly achieved*, especially in high SINR scenarios.

Applying the MLE to measurement data finally verified the principle feasibility of the presented approach and suggests good performance when either using a tracking algorithm or multiple transmitting anchors.

5.2 Outlook

The presented approach yields a promising technology for indoor localization. For TOA the feasibility of a real-time indoor localization system was already shown [8]. In order to realize a functional and robust TDOA system, several issues need to be addressed in future work:

- A substantial hurdle when implementing a TDOA system will be to deal with the *high computational complexity*. For the reduction of the computational expense different approaches are conceivable: A coarse clock synchronization would be beneficial, since it reduces the range of clock offset. Efficient optimization algorithms, such as the particle swarm filter in [9] could be used. On the other hand, relying on carefully selected signal

metrics could reduce the computational complexity greatly, without reducing the localization performance excessively. In this case an approach as for the TOA system [29] is thinkable, where an iterative search-and-subtract implementation of an MLE is used for estimating the arrival times.

- Being able to achieve the maximum possible localization performance requires the *knowledge of the covariance matrix* of the diffuse multipath and observation noise. In the present work we assumed its perfect knowledge, which is not appropriate in reality. Thus the task of determining the covariance matrix must be considered besides the actual localization problem. Possible approaches include the computation of the covariance matrix based on a sufficiently accurate environment model or by realizing online joint position and covariance matrix estimation based on multiple consecutive observations.
- To achieve a certain degree of *robustness*, the use of tracking algorithms is inevitable. E.g. using a Kalman filter for tracking the agent position has shown to greatly improve the TOA estimator performance in [29], and should also be applicable in a TDOA system.

A

Appendix to Chapter 3

A.1 Direct Derivation of the 2 x 2 EFIM when neglecting path-overlap

In this section we will examine (3.35) directly, without computing the 3×3 EFIM first. Therefore we first evaluate all the terms of (3.35) separately, using the definitions of $\mathbf{H}, \mathbf{K}$ and $\mathbf{L}$ in Eq. (3.20), (3.21) and (3.22).

$$
\begin{aligned}
&\mathbf{H}^T\tilde{\mathbf{\Lambda}}_A\mathbf{H} = \\
&= \begin{bmatrix} \frac{1}{c}\cos(\phi_1) & \cdots & \frac{1}{c}\cos(\phi_K) \\ \frac{1}{c}\sin(\phi_1) & \cdots & \frac{1}{c}\sin(\phi_K) \end{bmatrix} \begin{bmatrix} [\mathbf{\Lambda}_A]_{1,1} & & \\ & \ddots & \\ & & [\mathbf{\Lambda}_A]_{K,K} \end{bmatrix} \begin{bmatrix} \frac{1}{c}\cos(\phi_1) & \frac{1}{c}\sin(\phi_1) \\ \vdots & \vdots \\ \frac{1}{c}\cos(\phi_K) & \frac{1}{c}\sin(\phi_K) \end{bmatrix} \\
&= \frac{1}{c^2}\sum_{k=1}^{K}[\mathbf{\Lambda}_A]_{k,k} \begin{bmatrix} \cos^2(\phi_k) & \cos(\phi_k)\sin(\phi_k) \\ \cos(\phi_k)\sin(\phi_k) & \sin^2(\phi_k) \end{bmatrix}, \qquad \text{(A.1)}
\end{aligned}
$$

$$
\begin{aligned}
\mathbf{H}^T\tilde{\mathbf{\Lambda}}_A\mathbf{K} &= \begin{bmatrix} \frac{1}{c}\cos(\phi_1) & \cdots & \frac{1}{c}\cos(\phi_K) \\ \frac{1}{c}\sin(\phi_1) & \cdots & \frac{1}{c}\sin(\phi_K) \end{bmatrix} \begin{bmatrix} [\mathbf{\Lambda}_A]_{1,1} & & \\ & \ddots & \\ & & [\mathbf{\Lambda}_A]_{K,K} \end{bmatrix} \begin{bmatrix} 1 & \\ \vdots & \mathbf{0}_{K\times 2K} \\ 1 & \end{bmatrix} \\
&= \begin{bmatrix} \sum_{k=1}^{K}[\mathbf{\Lambda}_A]_{k,k}\frac{1}{c}\cos(\phi_k) & 0 & \cdots & 0 \\ \sum_{k=1}^{K}[\mathbf{\Lambda}_A]_{k,k}\frac{1}{c}\sin(\phi_k) & 0 & \cdots & 0 \end{bmatrix},
\end{aligned}
$$

$$\mathbf{K}^T\tilde{\mathbf{\Lambda}}_A\mathbf{K} = \begin{bmatrix} 1 & \cdots & 1 \\ & \mathbf{0}_{2K\times K} & \end{bmatrix} \begin{bmatrix} [\mathbf{\Lambda}_A]_{1,1} & & \\ & \ddots & \\ & & [\mathbf{\Lambda}_A]_{K,K} \end{bmatrix} \begin{bmatrix} 1 & \\ \vdots & \mathbf{0}_{K\times 2K} \\ 1 & \end{bmatrix}$$
$$= \begin{bmatrix} \sum_{k=1}^K [\mathbf{\Lambda}_A]_{k,k} & \mathbf{0}_{1\times 2K} \\ \mathbf{0}_{2K\times 1} & \mathbf{0}_{2K\times 2K} \end{bmatrix},$$

$$\mathbf{L}^T\tilde{\mathbf{\Lambda}}_C\mathbf{L} = \begin{bmatrix} 0 & \cdots & 0 \\ 1 & & \\ & \ddots & \\ & & 1 \end{bmatrix} \tilde{\mathbf{\Lambda}}_C \begin{bmatrix} 0 & 1 & \\ \vdots & & \ddots \\ 0 & & 1 \end{bmatrix} = \begin{bmatrix} 0 & \mathbf{0}_{1\times 2K} \\ \mathbf{0}_{2K\times 1} & \tilde{\mathbf{\Lambda}}_C \end{bmatrix},$$

$$(\mathbf{K}^T\tilde{\mathbf{\Lambda}}_A\mathbf{K} + \mathbf{L}^T\tilde{\mathbf{\Lambda}}_C\mathbf{L})^{-1} = \begin{bmatrix} \frac{1}{\sum_{k=1}^K [\mathbf{\Lambda}_A]_{k,k}} & \mathbf{0}_{1\times 2K} \\ \mathbf{0}_{2K\times 1} & \tilde{\mathbf{\Lambda}}_C^{-1} \end{bmatrix}.$$

Evaluating the subtractive term of (3.35) shows that $\tilde{\mathbf{\Lambda}}_C$ vanishes,

$$(\mathbf{H}^T\tilde{\mathbf{\Lambda}}_A\mathbf{K})(\mathbf{K}^T\tilde{\mathbf{\Lambda}}_A\mathbf{K} + \mathbf{L}^T\tilde{\mathbf{\Lambda}}_C\mathbf{L})^{-1}(\mathbf{K}^T\tilde{\mathbf{\Lambda}}_A\mathbf{H}) =$$
$$= \begin{bmatrix} \sum_{k=1}^K [\mathbf{\Lambda}_A]_{k,k}\frac{1}{c}\cos(\phi_k) & 0 & \cdots & 0 \\ \sum_{k=1}^K [\mathbf{\Lambda}_A]_{k,k}\frac{1}{c}\sin(\phi_k) & 0 & \cdots & 0 \end{bmatrix} \begin{bmatrix} \frac{1}{\sum_{k=1}^K [\mathbf{\Lambda}_A]_{k,k}} & \mathbf{0} \\ \mathbf{0} & \tilde{\mathbf{\Lambda}}_C^{-1} \end{bmatrix}$$
$$\begin{bmatrix} \sum_{k=1}^K [\mathbf{\Lambda}_A]_{k,k}\frac{1}{c}\cos(\phi_k) & \sum_{k=1}^K [\mathbf{\Lambda}_A]_{k,k}\frac{1}{c}\sin(\phi_k) \\ 0 & 0 \\ \vdots & \vdots \\ 0 & 0 \end{bmatrix}$$
$$= \frac{1}{\sum_{k=1}^K [\mathbf{\Lambda}_A]_{k,k}}\frac{1}{c^2}\cdot$$
$$\begin{bmatrix} \sum_{k=1}^K [\mathbf{\Lambda}_A]_{k,k}\cos(\phi_k) \\ \sum_{k=1}^K [\mathbf{\Lambda}_A]_{k,k}\sin(\phi_k) \end{bmatrix} \begin{bmatrix} \sum_{k=1}^K [\mathbf{\Lambda}_A]_{k,k}\cos(\phi_k) & \sum_{k=1}^K [\mathbf{\Lambda}_A]_{k,k}\sin(\phi_k) \end{bmatrix}. \quad \text{(A.2)}$$

Finally (3.39) is obtained by subtracting (A.2) from (A.1), and using (3.33).

B
Appendix to Chapter 4

B.1 Approximation of the Likelihood Function

We first rewrite the covariance matrix,

$$\begin{aligned}\mathbf{C} &= N_0 f_s \mathbf{I} + T_s \ \mathbf{\Phi}\ \mathbf{S}_\nu\ \mathbf{\Phi}^T \\ &= \mathbf{\Phi}\ \left[N_0 f_s \mathbf{\Phi}^{-1} \mathbf{\Phi}^{T^{-1}} + T_s\ \mathbf{S}_\nu\right]\ \mathbf{\Phi}^T. \end{aligned} \tag{B.1}$$

As already mentioned, $\mathbf{\Phi}$ is an orthogonal matrix when assuming perfect autocorrelation properties of the transmit pulse $s(t)$ and Nyquist sampling. We obtain an orthonormal matrix $\mathbf{\Phi'}$ by normalizing the columns of $\mathbf{\Phi}$, which is achieved by utilizing a diagonal matrix $\mathbf{L_s} = \mathrm{diag}\left(||\mathbf{s}_0||,\ ||\mathbf{s}_1||,\ \ldots,\ ||\mathbf{s}_{N-1}||\right)$, i.e. $\mathbf{\Phi'} = \mathbf{\Phi} \cdot \mathbf{L_s}^{-1}$. With $\mathbf{\Phi} = \mathbf{\Phi'} \cdot \mathbf{L_s}$ we can rewrite (B.1) as

$$\mathbf{C} = \mathbf{\Phi'}\mathbf{L_s}\ \left[N_0 f_s \mathbf{L_s}^{-1} \mathbf{\Phi'}^{-1} \mathbf{\Phi'}^{T^{-1}} \mathbf{L_s}^{T^{-1}} + T_s\ \mathbf{S}_\nu\right]\ \mathbf{L_s}\mathbf{\Phi'}^T.$$

We can now make use of the orthogonality of $\mathbf{\Phi'}$, i.e. $\mathbf{\Phi'}^{-1} = \mathbf{\Phi'}^T$ and with $\mathbf{L_s} = \mathbf{L_s}^T$ we finally arrive at

$$\mathbf{C} = \mathbf{\Phi'}\ \left[N_0 f_s \mathbf{I} + T_s\ \mathbf{E_s}\mathbf{S}_\nu\right]\ \mathbf{\Phi'}^T, \tag{B.2}$$

where $\mathbf{E_s}$ is a diagonal matrix with the energies of the shifted pulses $\varepsilon_{\mathbf{s}_i} = ||\mathbf{s}_i||^2$ on its diagonal,

$$\mathbf{E_s} = \mathbf{L_s}\mathbf{L_s} = \mathrm{diag}\left(\varepsilon_{\mathbf{s}_0},\ \varepsilon_{\mathbf{s}_1},\ \ldots,\ \varepsilon_{\mathbf{s}_{N-1}}\right).$$

The advantage from the formulation (B.2) is obvious, since inverting $\mathbf{C}$ can now be done by simply inverting a diagonal matrix,

$$\mathbf{Q} := \mathbf{C}^{-1} = \mathbf{\Phi'}\ \left[N_0 f_s \mathbf{I} + T_s\ \mathbf{E_s}\mathbf{S}_\nu\right]^{-1}\ \mathbf{\Phi'}^T\ .$$

Expansion of the log-LHF leads to

$$\begin{aligned}\ln\ f(\mathbf{r};\boldsymbol{\theta}) &= \ln\left(\det(\mathbf{Q})\right) - \ln\left(\pi^N\right) - (\mathbf{r}-\mathbf{S}_\tau\boldsymbol{\alpha})^H\mathbf{Q}(\mathbf{r}-\mathbf{S}_\tau\boldsymbol{\alpha}) \\ &\propto 2\mathrm{Re}\big\{\mathbf{r}^H\mathbf{Q}\mathbf{S}_\tau\boldsymbol{\alpha}\big\} - \boldsymbol{\alpha}^H\mathbf{S}_\tau^T\mathbf{Q}\mathbf{S}_\tau\boldsymbol{\alpha}.\end{aligned}$$

We can further simplify the following term $\mathbf{g} := \mathbf{Q}\mathbf{S}_\tau\boldsymbol{\alpha}$. We therefore assume equal energies for the shifted pulses, $\varepsilon_{\mathbf{s}_0} = \varepsilon_{\mathbf{s}_1} = \cdots = \varepsilon_{\mathbf{s}_{N-1}} = \varepsilon_{\mathbf{s}}$ and express the elements of $\mathbf{Q}$ as

$$[\mathbf{Q}]_{n,u} = \sum_{i=1}^{N} \frac{1/\varepsilon_{\mathbf{s}}\, s_{lp}((n-i)T_s)s_{lp}((u-i)T_s)}{f_sN_0 + T_s\varepsilon_{\mathbf{s}}S_\nu(iT_s-\xi)}.$$

With this we can write the elements of $\mathbf{g}$ as

$$\begin{aligned}[\mathbf{g}]_n &= \sum_{u=0}^{N-1}[\mathbf{Q}]_{n,u}\cdot\sum_{k=1}^{K}\alpha_k s_{lp}(uT_s-\tau_k) \\ &= \sum_{u=0}^{N-1}\sum_{i=1}^{N}\frac{1/\varepsilon_{\mathbf{s}}\, s_{lp}((n-i)T_s)s_{lp}((u-i)T_s)}{f_sN_0 + T_s\varepsilon_{\mathbf{s}}S_\nu(iT_s-\xi)}\cdot\sum_{k=1}^{K}\alpha_k s_{lp}(uT_s-\tau_k) \\ &= \sum_{i=1}^{N}\sum_{k=1}^{K}\frac{1/\varepsilon_{\mathbf{s}}\, s_{lp}((n-i)T_s)\alpha_k\sum_{u=0}^{N-1}s_{lp}((u-i)T_s)s_{lp}(uT_s-\tau_k)}{f_sN_0 + T_s\varepsilon_{\mathbf{s}}S_\nu(iT_s-\xi)}.\end{aligned}$$

Note that the inner sum $\sum_{u=0}^{N-1}(\cdot)$ equals zero if $\tau_k \neq iT_s$, which leads to

$$\begin{aligned}[\mathbf{g}]_n &= \sum_{k=1}^{K}\frac{1/\varepsilon_{\mathbf{s}}\, s_{lp}(nT_s-\tau_k)\alpha_k\sum_{u=0}^{N-1}s_{lp}^2(uT_s-\tau_k)}{f_sN_0 + T_s\varepsilon_{\mathbf{s}}S_\nu(\tau_k-\xi)} \\ &= \sum_{k=1}^{K}\frac{1/\varepsilon_{\mathbf{s}}\, s_{lp}(nT_s-\tau_k)\alpha_k\varepsilon_{\mathbf{s}}}{f_sN_0 + T_s\varepsilon_{\mathbf{s}}S_\nu(\tau_k-\xi)} \\ &= \sum_{k=1}^{K}\frac{s_{lp}(nT_s-\tau_k)\alpha_k}{f_sN_0 + T_s\varepsilon_{\mathbf{s}}S_\nu(\tau_k-\xi)}.\end{aligned}$$

With the definition of the weights $w_k^2 = \frac{N_0}{N_0+T_sS_\nu(\tau_k-\xi)}$ (3.12) and $\varepsilon_{\mathbf{s}} \approx 1/T_s$ follows

$$[\mathbf{g}]_n = \frac{1}{f_sN_0}\sum_{k=1}^{K}\alpha_k w_k^2 s_{lp}(nT_s-\tau_k),$$

or in matrix notation with $\mathbf{W} = \mathrm{diag}\left(w_1^2, w_2^2, \ldots, w_K^2\right)$,

$$\mathbf{g} = \frac{1}{f_sN_0}\mathbf{S}_\tau\mathbf{W}\boldsymbol{\alpha}.$$

With this approximation the log-LHF reduces to (4.11)

$$\ln\ f(\mathbf{r};\boldsymbol{\theta}) \propto 2\mathrm{Re}\big\{\mathbf{r}^H\mathbf{S}_\tau\mathbf{W}\boldsymbol{\alpha}\big\} - \boldsymbol{\alpha}^H\mathbf{S}_\tau^T\mathbf{S}_\tau\mathbf{W}\boldsymbol{\alpha}.$$

Bibliography

[1] D. Dardari, A. Conti, U. Ferner, A. Giorgetti, and M. Z. Win, "Ranging with ultrawide bandwidth signals in multipath environments," *Proceedings of the IEEE*, vol. 97, no. 2, pp. 404–426, Feb. 2009. [Online]. Available: http://ieeexplore.ieee.org/lpdocs/epic03/wrapper.htm?arnumber=4802191

[2] Y. Shen and M. Z. Win, "Fundamental limits of wideband localization part i: A general framework," *IEEE Transactions on Information Theory*, vol. 56, no. 10, pp. 4956–4980, Oct. 2010. [Online]. Available: http://ieeexplore.ieee.org/lpdocs/epic03/wrapper.htm?arnumber=5571900

[3] R. Mautz, "Overview of current indoor positioning systems," *Geodezija ir Kartografija*, vol. 35, no. 1, pp. 18–22, 2009. [Online]. Available: http://www.tandfonline.com/doi/abs/10.3846/1392-1541.2009.35.18-22

[4] ——, "The challenges of indoor environments and specification on some alternative positioning systems," in *6th Workshop on Positioning, Navigation and Communication, 2009. WPNC 2009*, Mar. 2009, pp. 29–36.

[5] S. Marano, W. Gifford, H. Wymeersch, and M. Win, "NLOS identification and mitigation for localization based on UWB experimental data," *IEEE Journal on Selected Areas in Communications*, vol. 28, no. 7, pp. 1026–1035, Sep. 2010.

[6] K. Witrisal and P. Meissner, "Performance bounds for multipath-assisted indoor navigation and tracking (MINT)," in *Communications (ICC), 2012 IEEE International Conference on*, 2012, p. 4321–4325. [Online]. Available: http://ieeexplore.ieee.org/xpls/abs_all.jsp?arnumber=6363827

[7] M. Z. Win and R. A. Scholtz, "Impulse radio: How it works," *Communications Letters, IEEE*, vol. 2, no. 2, p. 36–38, 1998. [Online]. Available: http://ieeexplore.ieee.org/xpls/abs_all.jsp?arnumber=660796

[8] P. Meissner, E. Leitinger, M. Lafer, and K. Witrisal, "Real-Time Demonstration System for Multipath-Assisted Indoor Navigation and Tracking (MINT)," in *IEEE ICC 2014 Workshop on Advances in Network Localization and Navigation (ANLN)*, Sydney, Australia, 2014.

[9] E. Leitinger, M. Fröhle, P. Meissner, and K. Witrisal, "Multipath-assisted maximum-likelihood indoor positioning using UWB signals," in *IEEE ICC 2014 Workshop on Advances in Network Localization and Navigation (ANLN)*, Sydney, Australia, 2014.

[10] N. Freris, S. Graham, and P. Kumar, "Fundamental limits on synchronizing clocks over networks," *IEEE Transactions on Automatic Control*, vol. 56, no. 6, pp. 1352–1364, Jun. 2011.

[11] N. Freris, H. Kowshik, and P. Kumar, "Fundamentals of large sensor networks: Connectivity, capacity, clocks, and computation," *Proceedings of the IEEE*, vol. 98, no. 11, pp. 1828–1846, Nov. 2010.

[12] P. Carbone, A. Cazzorla, P. Ferrari, A. Flammini, A. Moschitta, S. Rinaldi, T. Sauter, and E. Sisinni, "Low complexity UWB radios for precise wireless sensor network synchronization," *IEEE Transactions on Instrumentation and Measurement*, vol. 62, no. 9, pp. 2538–2548, Sep. 2013.

[13] J. Xu, M. Ma, and C. Law, "Position estimation using UWB TDOA measurements," in *The 2006 IEEE 2006 International Conference on Ultra-Wideband*, 2006, pp. 605–610.

[14] J. Xu, M. Ma, and C. L. Law, "Theoretical lower bound for UWB TDOA positioning," in *Global Telecommunications Conference, 2007. GLOBECOM'07. IEEE*, 2007, p. 4101–4105. [Online]. Available: http://ieeexplore.ieee.org/xpls/abs_all.jsp?arnumber=4411690

[15] J. Xu, M. Ma, and C. Law, "Performance of time-difference-of-arrival ultra wideband indoor localisation," *IET Science, Measurement & Technology*, vol. 5, no. 2, p. 46, 2011. [Online]. Available: http://digital-library.theiet.org/content/journals/10.1049/iet-smt.2010.0051

[16] R. Kaune, "Accuracy studies for TDOA and TOA localization," in *2012 15th International Conference on Information Fusion (FUSION)*, 2012, pp. 408–415.

[17] Y. Qi, H. Kobayashi, and H. Suda, "Analysis of wireless geolocation in a non-line-of-sight environment," *Wireless Communications, IEEE Transactions on*, vol. 5, no. 3, p. 672–681, 2006. [Online]. Available: http://ieeexplore.ieee.org/xpls/abs_all.jsp?arnumber=1611097

[18] A. Urruela and J. Riba, "Novel closed-form ML position estimator for hyperbolic location," in *IEEE International Conference on Acoustics, Speech, and Signal Processing, 2004. Proceedings. (ICASSP '04)*, vol. 2, 2004, pp. ii–149–52 vol.2.

[19] E. Leitinger, P. Meissner, C. Ruedisser, G. Dumphart, and K. Witrisal, "Evaluation of position-related information in multipath components for indoor positioning," *IEEE Journal on Selected Areas in Communications - 2014 Special Issue on Location-Awareness for Radios and Networks.*, 2014, submitted.

[20] P. Meissner, C. Steiner, and K. Witrisal, "UWB positioning with virtual anchors and floor plan information," in *Positioning Navigation and Communication (WPNC), 2010 7th Workshop on*, 2010, p. 150–156. [Online]. Available: http://ieeexplore.ieee.org/xpls/abs_all.jsp?arnumber=5650374

[21] G. Dumphart, "Performance bounds for anchorless cooperative indoor localization exploiting multipath," Master's thesis, Graz University of Technology, 2014.

[22] *Fundamentals of Quartz Oscillators, Application Note 200-2*, Hewlett-Packard Company, 1997.

[23] P. Meissner, D. Arnitz, T. Gigl, and K. Witrisal, "Analysis of an indoor UWB channel for multipath-aided localization," in *Ultra-Wideband (ICUWB), 2011 IEEE International Conference on*, 2011, p. 565–569. [Online]. Available: http://ieeexplore.ieee.org/xpls/abs_all.jsp?arnumber=6058910

[24] J. Karedal, S. Wyne, P. Almers, F. Tufvesson, and A. Molisch, "A measurement-based statistical model for industrial ultra-wideband channels," *IEEE Transactions on Wireless Communications*, vol. 6, no. 8, pp. 3028–3037, Aug. 2007. [Online]. Available: http://ieeexplore.ieee.org/lpdocs/epic03/wrapper.htm?arnumber=4290044

[25] H. L. V. Trees, *Detection, Estimation, and Modulation Theory.* John Wiley & Sons, Apr. 2004.

[26] S. M. Kay, *Fundamentals of Statistical Signal Processing: Estimation Theory.* Prentice-Hall PTR, 1998.

[27] P. Meissner, E. Leitinger, M. Lafer, and K. Witrisal, *MeasureMINT UWB database*, Graz University of Technology, 2013. [Online]. Available: www.spsc.tugraz.at/tools/UWBmeasurements

[28] P. Meissner and K. Witrisal, "Analysis of position-related information in measured UWB indoor channels," in *Antennas and Propagation (EUCAP), 2012 6th European Conference on*, 2012, p. 6–10. [Online]. Available: http://ieeexplore.ieee.org/xpls/abs_all.jsp?arnumber=6206547

[29] P. Meissner, E. Leitinger, M. Fröhle, and K. Witrisal, "Accurate and robust indoor localization systems using ultra-wideband signals," *arXiv:1304.7928 [cs, math]*, Apr. 2013, arXiv: 1304.7928. [Online]. Available: http://arxiv.org/abs/1304.7928